

---

**Search for Supersymmetry in events  
with an isolated lepton, at least 2-9 jets  
and missing transverse momentum with  
the ATLAS detector**

Nikolai Hartmann

---



München 2018



---

**Search for Supersymmetry in events  
with an isolated lepton, at least 2-9 jets  
and missing transverse momentum with  
the ATLAS detector**

**Nikolai Hartmann**

---

Dissertation  
an der Fakultät für Physik  
der Ludwig-Maximilians-Universität  
München

vorgelegt von  
Nikolai Hartmann  
aus Starnberg

München, den 8.1.2018

Erstgutachter: Prof. Dr. Dorothee Schaile

Zweitgutachter: Prof. Dr. Wolfgang Dünneweber

Tag der mündlichen Prüfung: 8.3.2018

# Zusammenfassung

Diese Arbeit stellt eine Suche nach den supersymmetrischen Partnern der Quarks (Squarks) und Gluonen (Gluinos) in Proton-Proton Kollisionsereignissen mit exakt einem Elektron oder Muon, mehreren Jets und fehlendem Transversalimpuls im Endzustand vor. Die Lepton Signatur unterdrückt den reinen QCD Untergrund und die Restriktion auf ein Lepton reduziert die Hauptuntergründe auf Prozesse mit  $W$ -Boson Zerfällen, die weiter durch ein Kriterium auf die transverse Masse unterdrückt werden können. Die verwendeten Daten wurden 2015 und 2016 mit einer integrierten Luminosität von  $36,1 \text{ fb}^{-1}$  am ATLAS Experiment aufgezeichnet. Die Suche betrachtet verschiedene Signalregionen mit 2-6 Jets, die in einer vollen statistischen Kombination interpretiert werden. Eine zusätzliche 9-Jet Signalregion zielt auf längere Zerfallsketten ab. Der Untergrund in der 9-Jet Region wird mit einer datengestützten Technik, die auf der Invarianz der Verteilung der transversen Masse in Ereignissen mit unterschiedlicher Jet Multiplizität basiert, abgeschätzt.

Die Suche zeigte keinen signifikanten Überschuss an Ereignissen über der Standardmodellervorhersage. Die 2-6-Jet Signalregionen werden in vereinfachten Modellen mit einstufigen Squark und Gluino Zerfällen mit einem  $W$ -Boson interpretiert und schließen Gluino Massen bis zu  $2,1 \text{ TeV}$  und Squark Massen bis zu  $1,25 \text{ TeV}$  bei 95% Konfidenzniveau aus. Die 9-Jet Signalregion wird in zweistufigen Gluino Zerfällen mit einem  $W$ - und einem  $Z$ -Boson und in einer Teilauswahl des phänomenologischen minimalen supersymmetrischen Standardmodell (pMSSM) interpretiert. In den Modellen mit zweistufigem Zerfall werden Gluino Massen mit bis zu  $1,75 \text{ TeV}$  und in den pMSSM Modellen mit bis zu  $1,7 \text{ TeV}$  bei 95% Konfidenzniveau ausgeschlossen.



# Abstract

This thesis presents a search for the supersymmetric partners of quarks (squarks) and gluons (gluinos) in proton-proton collision events with exactly one electron or muon, multiple jets and missing transverse momentum in the final state. The lepton signature suppresses the pure QCD background and the restriction to one lepton reduces the main backgrounds to processes with  $W$  boson decays which can be further suppressed via a requirement on the transverse mass. The data used amount to an integrated Luminosity of  $36.1 \text{ fb}^{-1}$  taken in 2015 and 2016 with the ATLAS experiment at the LHC with a centre of mass energy of 13 TeV. The search is performed in different signal regions, requiring at least 2-6 jets that are interpreted in a full statistical combination. An additional 9-jet signal region targets longer decay chains. The background in the 9-jet region is estimated by a data driven technique, based on the invariance of the transverse mass distribution in events with different jet multiplicities.

No significant excess of events above the standard model expectation was found. The 2-6-jet signal regions are interpreted in simplified models with squark and gluino one-step decays with a  $W$  boson and exclude gluino masses up to 2.1 TeV and squark masses up to 1.25 TeV at 95% confidence level. The 9-jet signal region is interpreted in simplified models with gluino two-step decays with a  $W$  and a  $Z$  boson and in a subset of the phenomenological minimal supersymmetric standard model (pMSSM). In the two-step models gluino masses are excluded up to 1.75 TeV and in the pMSSM models up to 1.7 TeV at 95% confidence level.



# Contents

<b>Introduction</b>	<b>1</b>
<b>1 Theory</b>	<b>3</b>
1.1 The standard model of particle physics . . . . .	3
1.2 Quantum field theory and symmetries . . . . .	5
1.2.1 The Lagrangian . . . . .	5
1.2.2 Feynman diagrams . . . . .	5
1.2.3 Divergencies and Renormalisation . . . . .	6
1.2.4 The standard model as a gauge theory . . . . .	6
1.3 Supersymmetry . . . . .	10
1.3.1 Addressing open questions . . . . .	10
1.3.2 The MSSM . . . . .	14
1.3.3 Production of gluinos and squarks at the LHC . . . . .	18
1.3.4 Decay models of gluinos and squarks in this analysis . . . . .	19
1.3.5 Current constraints from direct searches . . . . .	23
1.4 Monte-Carlo event generation . . . . .	25
<b>2 The LHC and ATLAS</b>	<b>29</b>
2.1 The LHC . . . . .	29
2.2 The ATLAS Experiment . . . . .	31
2.2.1 Coordinate System . . . . .	31
2.2.2 Subdetectors . . . . .	32
2.2.3 Forward detectors . . . . .	34
2.2.4 Trigger system . . . . .	34
2.2.5 Data taking in 2015 and 2016 . . . . .	34
<b>3 Analysis Overview</b>	<b>37</b>
3.1 Inclusive search in 1-lepton final states . . . . .	37
3.2 Signal grids . . . . .	37
3.3 Backgrounds . . . . .	38
3.4 Simulated samples . . . . .	39

3.5	Object definitions and event preselection . . . . .	41
3.5.1	Tracks, vertices and pile-up . . . . .	41
3.5.2	Jets . . . . .	42
3.5.3	B-tagging . . . . .	42
3.5.4	Electrons . . . . .	43
3.5.5	Muons . . . . .	43
3.5.6	Lepton isolation . . . . .	44
3.5.7	Missing transverse momentum . . . . .	44
3.5.8	Overlap removal . . . . .	44
3.5.9	Event preselection . . . . .	45
3.6	Observables . . . . .	46
3.7	Trigger . . . . .	47
<b>4</b>	<b>Statistical data analysis</b>	<b>51</b>
4.1	Test statistic and p-values . . . . .	51
4.2	Building the Likelihood . . . . .	53
4.3	Estimating sensitivity . . . . .	54
<b>5</b>	<b>Signal region optimisation</b>	<b>57</b>
5.1	Methods . . . . .	57
5.1.1	$N$ -dimensional scan . . . . .	57
5.1.2	$N-1$ plots . . . . .	58
5.2	Optimisation for the analysis with $3.2 \text{ fb}^{-1}$ . . . . .	60
5.3	Concept for the analysis with $36.1 \text{ fb}^{-1}$ . . . . .	64
5.4	Optimisation for the multijet channel . . . . .	66
<b>6</b>	<b>Background estimation</b>	<b>71</b>
6.1	The transfer factor approach . . . . .	71
6.2	Blind analysis . . . . .	72
6.3	Convention for data/MC comparison plots . . . . .	73
6.4	Background estimation for the 2-6-jet channels . . . . .	74
6.5	$t\bar{t}/Wt$ decay modes . . . . .	79
6.6	Background estimation for the 9-jet signal region . . . . .	80
6.6.1	Motivation . . . . .	82
6.6.2	Region definitions . . . . .	84
6.6.3	Invariance of the transverse mass distribution . . . . .	87
6.6.4	Statistical model . . . . .	87
<b>7</b>	<b>Uncertainties</b>	<b>91</b>
7.1	Experimental uncertainties . . . . .	91
7.1.1	Scale factors . . . . .	91

7.1.2	Pileup reweighting and luminosity . . . . .	92
7.1.3	Jets . . . . .	92
7.1.4	Electron and Muon calibration . . . . .	93
7.1.5	Missing transverse energy . . . . .	94
7.1.6	Impact on signal regions . . . . .	94
7.2	Theory uncertainties . . . . .	95
7.2.1	Truth selection . . . . .	96
7.2.2	Backgrounds . . . . .	96
7.2.3	Signal . . . . .	97
7.2.4	Cross section uncertainties . . . . .	101
7.2.5	Impact on signal regions . . . . .	101
<b>8</b>	<b>Results</b>	<b>103</b>
8.1	Convention for uncertainties in tables and plots . . . . .	103
8.2	Background fit . . . . .	103
8.3	Validation regions . . . . .	108
8.4	Signal regions . . . . .	108
8.5	Interpretation . . . . .	108
8.6	Discussion . . . . .	112
<b>9</b>	<b>Summary and Outlook</b>	<b>117</b>
	<b>Bibliography</b>	<b>119</b>
	<b>Acronyms</b>	<b>131</b>
	<b>Appendix A Optimisation plots</b>	<b>135</b>
	<b>Appendix B Signal contamination plots</b>	<b>137</b>
	<b>Appendix C Studies on the invariant <math>m_T</math> shape</b>	<b>144</b>



# Introduction

A long series of interplay between theoretical models and experimental observations in the 20th century led to the standard model of particle physics. The discovery of the Higgs boson in 2012 completed a crucial part of this picture. The standard model is the most fundamental description of our world and many of its predictions have been verified to high precision, even for extremely rare phenomena. On the other hand it fails to describe long known phenomena that dominate the large scale physics and the evolution of the universe. Most prominently, no consistent description of gravity is included and there are strong indications that large scale physics cannot be described without a form of dark matter, around five times more abundant than the matter described by the standard model. This clash of high precision on the one side and the clear limitations on the other side is the biggest puzzle in current fundamental research. One promising extension of the standard model is the concept of Supersymmetry. It would lead to the addition of a superpartner for each standard model particle. The theory exists since the 70s and the superpartners have been searched for since then. No clear indications have been found so far. The superpartners might be just too heavy to be produced at particle physics experiments so far. In 2015 the Large Hadron Collider (LHC) increased its centre of mass energy from 8 TeV to 13 TeV, raising the hope for a new discovery. If new particles are strongly interacting, they could be produced numerously at the LHC and discovered with already a small amount of data. The superpartners of quarks and gluons would lead to such a scenario and were therefore one focus of searches since the beginning of 2015.

This thesis describes a search for squarks and gluinos in events with exactly one lepton (electron or muon), multiple jets and missing transverse momentum with data taken in 2015 and 2016 by the ATLAS experiment. First, an introduction to the standard model of particle physics and to Supersymmetry is given, followed by an overview of the LHC and the ATLAS detector. Next, the ingredients and techniques of the one lepton analysis are described. The further chapters describe the optimisation of search regions, the background estimation and the uncertainties considered. Finally, the results are shown and discussed.



# Chapter 1

## Theory

### 1.1 The standard model of particle physics

The most fundamental description of nature is given by the Standard model (SM) of Particle Physics. It describes matter in form of spin  $\frac{1}{2}$  fermions and all known interactions, except for gravitation, by the exchange of spin 1 bosons.

These interactions are the electromagnetic interaction, the weak interaction and the strong interaction. The interactions a particle can participate are associated to charge-like quantum numbers. In a relativistic quantum theory like the SM, for each particle there exists an anti-particle with all charge-like quantum numbers inverted. The charge associated to the electromagnetic interaction is the electric charge  $Q$ . The electromagnetic interaction is mediated by photons ( $\gamma$ ) and described by a quantum field theory, the quantum electrodynamics (QED). The strong interaction describes interactions of particles carrying colour charge. Three types of coloured particles exist, carrying *red*, *green* and *blue* colour charge. The interaction is mediated by gluons ( $g$ ) which carry one unit of colour and one unit of anticolour. The theory of strong interactions is described by quantum chromodynamics (QCD).

Fermions can be classified into leptons and quarks. Leptons are paired in doublets of an electrically charged lepton and a corresponding neutral neutrino. Quarks carry both electric charge and colour charge and are paired in doublets of *up-type* quarks (u, c, t) with electric charge  $+\frac{2}{3}$  and *down-type* quarks (d, s, b) with electric charge  $-\frac{1}{3}$ . Physical states are always “colour-neutral”, consisting either of states containing quarks of all three colours (baryons) or colour and anticolour (mesons).

The association of the weak interaction to a charge is done in a unified description of the weak and electromagnetic interaction - the electroweak interaction, theoretically proposed by Glashow, Weinberg and Salam (GWS) [1–3]. In this unified description, for each particle two numbers are assigned: the third component of the isospin  $I_3$  and the weak hypercharge

Name	Spin	Mass
$W^\pm$	1	80.4 GeV
$Z$	1	91.2 GeV
Photon ( $\gamma$ )	1	0
Gluon ( $g$ )	1	0
Higgs boson ( $H$ )	0	125 GeV

Table 1.1: Bosons in the SM. The masses are rounded to 3 significant digits. For precise values and errors see [10]

$Y$ , where the electric charge quantum number  $Q$  can be identified as (notation from [4]):

$$Q = I_3 + Y \quad (1.1)$$

Parity violation (violation of point reflection symmetry) in weak interactions necessitates the separate treatment of left- and right-handed fermions. In the limit of vanishing masses these states correspond to particles where the projection of the spin onto the momentum is positive (helicity +1) for the right-handed fermions, and negative (helicity -1) for the left-handed fermions. The weak interaction is mediated by the electrically charged  $W^\pm$  bosons and the neutral  $Z$  boson. Interactions mediated by  $W^\pm$  bosons are maximally parity violating—only left-handed fermions participate in these interactions. For left-handed fermions  $I_3 = \frac{1}{2}$  for neutrinos and up-type quarks and  $I_3 = -\frac{1}{2}$  for charged leptons and down-type quarks.

The consistent description of electroweak interactions with massive particles in the SM is achieved by the Higgs mechanism, as proposed by Brout and Englert, Higgs, Guralnik and Hagen in 1964 [5–7]. A consequence of this description is the existence of an additional Spin 0 boson, the Higgs (H) boson. A particle consistent with the SM H boson has been recently observed by the ATLAS and CMS Collaborations [8, 9]. Table 1.1 gives a list of all bosons in the SM and their masses.

Leptons and quarks come in 3 “generations”. The masses increase from generation to generation. Weak interactions mediated by  $W^\pm$  bosons couple up-type quarks to down-type quarks and leptons to neutrinos. While the coupling within one generation is the strongest, there exist non zero couplings between the generations. The full form of all mixings is described by the unitary 3x3 Cabibbo–Kobayashi–Maskawa (CKM) matrix, which was introduced by Makoto Kobayashi and Toshihide Maskawa in 1973 [11] to introduce a mechanism for CP violation (violation of symmetry under joint parity + charge conjugation) in the SM. Table 1.2 shows a list of all fermions of the 3 generations and their masses.

In the most simple version of the SM neutrinos are exactly massless. However, neutrino oscillations have been observed in many experiments, the first hints came from the disappearance of solar neutrinos at the Homestake experiment [12]. The oscillations can be described by non-zero masses and a mixing matrix in the lepton sector (the Pontecorvo–Maki–Nakagawa–Sakata (PMNS) [13] matrix).

Generation	Leptons		Quarks	
	Name	Mass	Name	Mass
1	Electron ( $e$ )	511 keV	up ( $u$ )	$\approx 2$ MeV
	- neutrino ( $\nu_e$ )	$\approx 0$	down ( $d$ )	$\approx 5$ MeV
2	Muon ( $\mu$ )	106 MeV	charm ( $c$ )	1.28 GeV
	- neutrino ( $\nu_\mu$ )	$\approx 0$	strange ( $s$ )	$\approx 95$ MeV
3	Tau ( $\tau$ )	1.78 GeV	top ( $t$ )	173 GeV
	- neutrino ( $\nu_\tau$ )	$\approx 0$	bottom ( $b$ )	4.18 GeV

Table 1.2: Particles of all fermion families and observed masses. The masses are rounded to 3 significant digits (if known to that precision). For precise values and errors and different mass definition schemes see [10].

## 1.2 Quantum field theory and symmetries

This section will briefly describe the formalism of quantum field theory and how the SM is described by fundamental symmetries. The description and notation is following [4].

### 1.2.1 The Lagrangian

In field theory the term *Lagrangian* refers to the Lagrangian density  $\mathcal{L}$ , whose space-time integral is the action

$$S = \int \mathcal{L}(\phi, \partial_\mu \phi) d^4x. \quad (1.2)$$

The Lagrangian is a function of one or more fields  $\phi(x)$  and their derivatives  $\partial_\mu \phi$ . Using the principle of least action, the equation of motion of each field is given by the Euler-Lagrange equation,

$$\partial_\mu \left( \frac{\partial \mathcal{L}}{\partial(\partial_\mu \phi)} \right) - \frac{\partial \mathcal{L}}{\partial \phi} = 0. \quad (1.3)$$

### 1.2.2 Feynman diagrams

The transition from field theory to quantum field theory is done by either imposing canonical commutation relations between the fields and their momentum density conjugates, analogous to the commutation relation between position and momentum operator in non-relativistic quantum mechanics, or by using the path integral formalism.

The equations of motion can only be analytically solved for free field theories, containing no interactions between the fields. Predicting scattering cross sections and decay rates from

theories with interaction terms is done using perturbation theory. Each transition matrix element can be expanded in a power series in the coupling constant, where the summands can be represented as Feynman diagrams. The diagrams are created by using a set of Feynman rules, containing possible vertices, representing the interaction of different fields, and propagators, representing the propagation of fields. All combinations of propagators and vertices that can be placed between the incoming and outgoing particles represent the full perturbation series. The lowest possible order in the series is called leading order (LO) and the further orders next-to-leading order (NLO), NNLO and so forth.

### 1.2.3 Divergencies and Renormalisation

For diagrams that contain loops, an integration over all possible momenta in the loop has to be performed, since the momenta are not determined by energy-momentum conservation. This leads to divergent amplitudes when taking the momentum to infinity—the *ultraviolet divergencies*. The divergencies can be eliminated by regularising the integrals, e.g. imposing a cut-off momentum or performing the integral in  $N > 4$  spacetime dimensions and following a *renormalisation* procedure that replaces the bare values of parameters like masses or coupling constants by their physical (measured) values. Theories that can be described by a finite number of measured parameters that do not depend on the divergent integrals are called *renormalisable*. The Yang-Mills theories the standard model is based on have been shown to be renormalisable by Gerard 't Hooft and Martinus Veltman [14, 15]. An important prediction of renormalisation is the dependence of the measured value of coupling constants on the energy scale—the *running coupling*. This makes predictions for QCD possible. At high energy or low distance scales, QCD becomes asymptotically free, while at low scales the coupling is greater than one, rendering the perturbative expansion impossible. The strong coupling  $\alpha_s$  runs with the momentum transfer  $Q$  proportional to  $\frac{1}{\log(Q/\Lambda)}$ . The pole at  $Q = \Lambda$  corresponds to the scale where the coupling becomes strong and hadronisation takes place. Experimentally,  $\Lambda$  is around 200 MeV and  $\alpha_s(M_Z)$  around 0.12 [10]. *Infrared divergencies* occur when the *real* emission of *collinear* or *soft* (vanishing momenta) particles is considered. The divergencies also occur in *virtual* emission contributions where the particles are reabsorbed. For the SM, the Kinoshita-Lee-Nauenberg (KLN) [16, 17] theorem states that the infinite corrections from real and virtual emissions cancel.

### 1.2.4 The standard model as a gauge theory

The fields of the standard model leave physical predictions invariant under certain transformations. According to Noether's theorem [18] such symmetries lead to conservation laws. In quantum field theory, the conservation of charge-like quantum numbers is related to a symmetry under global (spacetime independent) transformations. The existence of gauge fields is related to a symmetry under a local (spacetime dependent) gauge transformation.

QED can be taken as an example for this procedure. The free field Lagrangian for a single non-interacting fermion field (leading to the Dirac equation) is given by

$$\mathcal{L}_{\text{Dirac}} = \bar{\psi}(i\gamma^\mu\partial_\mu)\psi - m\bar{\psi}\psi \quad (1.4)$$

To be a U(1) gauge theory the Lagrangian has to be invariant under a transformation

$$\psi(x) \rightarrow e^{i\alpha(x)}\psi(x). \quad (1.5)$$

Therefore, a vector field  $A_\mu$  (the photon) has to be introduced that transforms as

$$A_\mu(x) \rightarrow A_\mu(x) - \frac{1}{e}\partial_\mu\alpha(x). \quad (1.6)$$

The derivative  $\partial_\mu$  is replaced by the gauge covariant derivative

$$D_\mu = \partial_\mu + ieA_\mu, \quad (1.7)$$

leading to interaction terms between the fermion and photon field. The kinetic term for the free photon field (leading to the Maxwell equations) is given by

$$\mathcal{L}_{\text{Maxwell}} = -\frac{1}{4}F_{\mu\nu}F^{\mu\nu}, \quad (1.8)$$

with the field strength tensor  $F_{\mu\nu}$  defined as

$$F_{\mu\nu} = \partial_\mu A_\nu - \partial_\nu A_\mu. \quad (1.9)$$

In addition to U(1), the SM is also based on SU(N) (Yang-Mills) theory. The procedure here is similar. There have to be N fermion fields (in group theory terms they are in the *N-representation*) that transform under an SU(N) rotation. The gauge covariant derivative is

$$D_\mu = \partial_\mu - igA_\mu^a t^a \quad a = 1, \dots, (N^2 - 1) \quad (1.10)$$

where  $t^a$  are the  $N^2 - 1$  generators of SU(N), each of them corresponding to one gauge boson. The kinetic term for the gauge fields is given by

$$\mathcal{L}_{\text{Gauge}} = -\frac{1}{4}F_{\mu\nu}^a F^{\mu\nu,a}, \quad (1.11)$$

where the field strength tensor contains an additional third term, leading to cubic and quartic couplings between the gauge bosons,

$$F_{\mu\nu}^a = \partial_\mu A_\nu^a - \partial_\nu A_\mu^a + gf^{abc}A_\mu^b A_\nu^c. \quad (1.12)$$

The structure constants  $f^{abc}$  are defined by the commutation relations

$$[t^a, t^b] = if^{abc}t^c \quad (1.13)$$

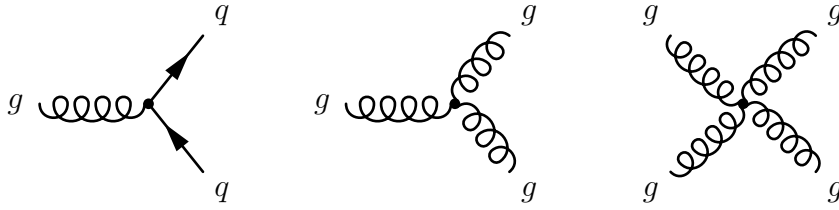


Figure 1.1: Vertices of QCD

QCD is based on  $SU(3)$ . Thus, there are 8 gluon fields. Since only quarks participate in the strong interaction (carry colour charge), they are in the 3-representation of  $SU(3)$  while the other fermions are singlets. The interaction vertices between gluons and quarks and the gluon self interaction are shown in Figure 1.1.

The GWS theory is based on the symmetry groups  $SU(2)$  and  $U(1)$ , where only the left-handed fermions are doublets w.r.t.  $SU(2)$ ,

$$E_L = \begin{pmatrix} e \\ \nu_e \end{pmatrix}_L, \quad Q_L = \begin{pmatrix} u \\ d \end{pmatrix}_L \quad (1.14)$$

and analogous for the other generations. All fermions couple to the  $U(1)$  gauge field, according to their weak hypercharge  $Y$ .

The local gauge symmetries forbid mass terms for the gauge bosons. Fermion mass terms couple left- and right-handed fields and are therefore also not allowed. Since both the weak bosons and fermions observed in nature are massive, the electroweak symmetry has to be broken. This is described by spontaneous symmetry breaking via a complex scalar field—the Higgs field. The field has an additional term in the Lagrangian, the Higgs potential,

$$V(\phi) = -\mu^2 \phi^* \phi + \frac{\lambda}{2} (\phi^* \phi)^2 \quad (1.15)$$

that will lead to a vacuum expectation value (VEV) at the minimum

$$\phi^* \phi = \frac{\mu^2}{\lambda} \equiv v^2, \quad (1.16)$$

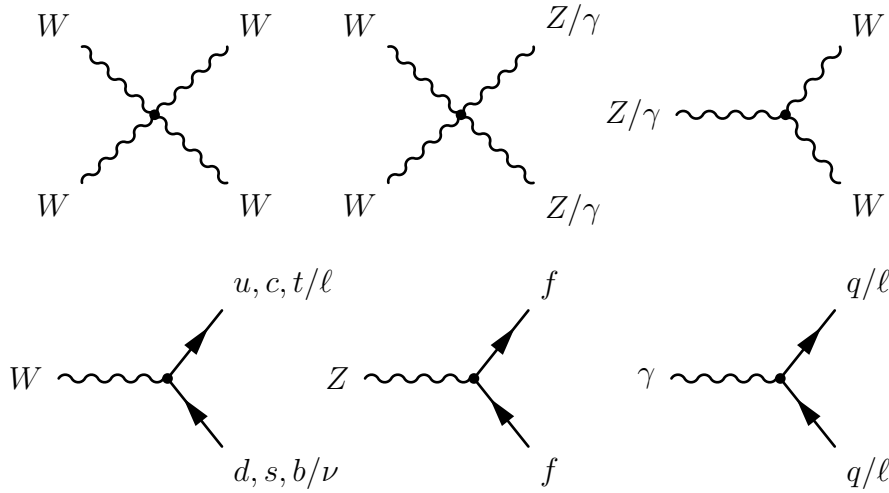
that spontaneously breaks the electroweak symmetry. If the ground state of the field is written in the form

$$\phi(x) = \frac{1}{\sqrt{2}} \begin{pmatrix} 0 \\ v \end{pmatrix}, \quad (1.17)$$

the massive weak bosons  $W^\pm$  and  $Z$  can be written in terms of the gauge bosons of  $SU(2)$  ( $A_\mu^{1,2,3}$ ) and  $U(1)$  ( $B_\mu$ ):

$$W_\mu^\pm = \frac{1}{\sqrt{2}} (A_\mu^1 \mp i A_\mu^2) \quad \text{with} \quad m_W = g \frac{v}{2} \quad (1.18)$$

$$Z_\mu^0 = \frac{1}{\sqrt{g^2 + g'^2}} (g A_\mu^3 - g' B_\mu) \quad \text{with} \quad m_Z = \sqrt{g^2 + g'^2} \frac{v}{2} \quad (1.19)$$


 Figure 1.2: Interactions of the  $Z$ ,  $W$  and  $\gamma$  bosons

with the coupling constants  $g$  and  $g'$  of  $SU(2)$  and  $U(1)$ . The weak mixing angle  $\theta_w$  is defined as,

$$\cos \theta_w = \frac{g}{\sqrt{g^2 + g'^2}} \quad \sin \theta_w = \frac{g'}{\sqrt{g^2 + g'^2}} \quad (1.20)$$

to describe the change of basis from  $(A^3, B)$  to  $(Z^0, A)$ ,

$$\begin{pmatrix} Z^0 \\ A \end{pmatrix} = \begin{pmatrix} \cos \theta_w & -\sin \theta_w \\ \sin \theta_w & \cos \theta_w \end{pmatrix} \begin{pmatrix} A^3 \\ B \end{pmatrix} \quad (1.21)$$

The QED Lagrangian is restored by the photon field,

$$A_\mu = \frac{1}{\sqrt{g^2 + g'^2}}(g' A_\mu^3 + g B_\mu), \quad (1.22)$$

with the electron charge

$$e = g \sin \theta_w = g' \cos \theta_w \quad (1.23)$$

and the electric charge quantum number as defined in Equation 1.1. The interaction vertices between the  $W$ ,  $Z$  and photon fields ( $\gamma$ ) and their couplings to fermions are shown in Figure 1.2.

Fluctuations around the VEV of the Higgs field lead to the occurrence of a massive scalar boson—the Higgs boson. This also creates couplings between the Higgs boson and the electroweak gauge bosons<sup>1</sup> and triple and quartic couplings of the Higgs boson to itself. Fermions acquire their mass terms by Yukawa (fermion-scalar-fermion) coupling terms to the Higgs field—the resulting mass term after symmetry breaking is proportional

<sup>1</sup>For simplicity, the term *gauge boson* will from now on also be used for the electroweak gauge bosons after symmetry breaking (the massive weak bosons and the photon)

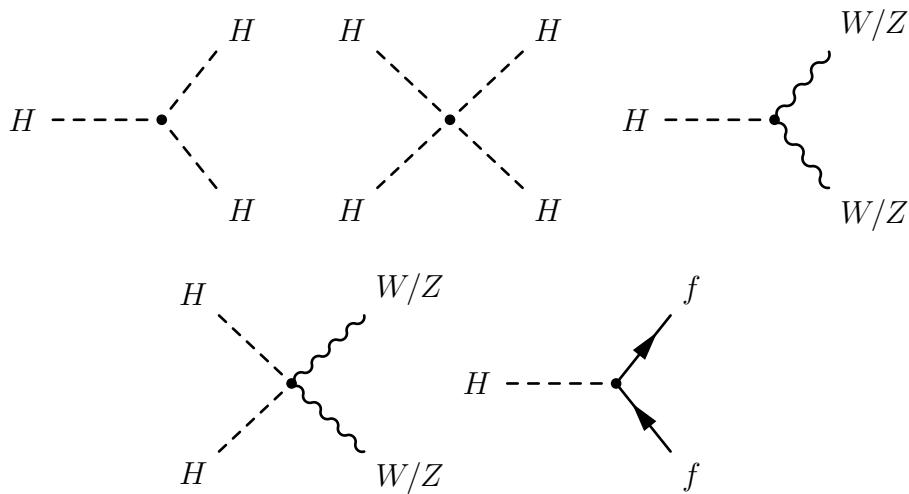


Figure 1.3: Couplings involving the SM Higgs boson

to a Yukawa coupling constant  $Y_f$ . Therefore, the Higgs boson has couplings to fermions, proportional to their mass. Figure 1.3 shows the interaction vertices of the Higgs boson to the gauge bosons and fermions.

## 1.3 Supersymmetry

Supersymmetry (SUSY) is a symmetry relating bosons and fermions. In a supersymmetric theory the action is thus invariant under a transformation  $Q$  that transforms a bosonic state into a fermionic state and vice versa:

$$Q |\text{Boson}\rangle = |\text{Fermion}\rangle, \quad Q |\text{Fermion}\rangle = |\text{Boson}\rangle \quad (1.24)$$

SUSY requires the bosons and fermions that transform into each other to be of equal mass. Since no such *superpartners* have been observed, they must be at a different mass scale—in any realistic model SUSY has to be broken. This chapter is following Ref. [19] if no other references are given.

### 1.3.1 Addressing open questions

Despite its huge success in describing all measurements so far up to great precision, the SM has many open questions. Some phenomena observed in the universe are not described by the SM and the theoretical structure hints to a more fundamental description—of which the SM is the low energy limit. Some of these aspects may be addressed by SUSY.

## Dark matter

Many observations hint to an additional source of gravitational attraction, not covered by the visible matter described by the SM, where visible means emitting light. The observed rotation curves of objects in galaxies are not consistent with the gravitational attraction of the visible matter [20]. Discrepancies are also seen by calculating the (gravitational) potential energy from the observed kinetic energy of galaxies moving in clusters via the virial theorem [21] or from gravitational lensing. One of the most significant observations is the bullet cluster, a galaxy cluster that passed through another galaxy cluster. Most of the visible matter (hot gas) got significantly distorted, while the matter making up most of the mass passed through each other with very little interaction [22]. Finally, the anisotropies in the cosmic microwave background (CMB) are described extremely well by the  $\Lambda$ CDM model, which includes a density of cold dark matter. The most recent measurement from the Planck Collaboration in 2015 [23],

$$\Omega_c h^2 = 0.1188 \pm 0.0010,$$

corresponds to a fraction of dark matter of the critical density  $\Omega_c \approx 0.26$  in contrast to the fraction for baryonic matter  $\Omega_b \approx 0.049$ . Thus, the dark matter density is more than 5 times larger than the baryonic matter density<sup>2</sup>.

The most popular explanation for these observations is the existence of dark matter in form of weakly interacting massive particles (WIMPs). If the lightest supersymmetric particle (LSP) is stable, it may be a candidate for dark matter.

## Unification of forces

Some connections between parameters of the standard model hint to a more fundamental description to explain these connections. A prominent example is the exact cancellation of electron charge and proton charge ( $2 \times$  up-quark charge +  $1 \times$  down-quark charge). The SM does not require any connection between quarks and leptons a priori. However, there is a bizarre cancellation of quark and lepton quantum numbers in anomalous triangle diagrams that would spoil the gauge invariance. Due to these anomalies, the SM is only consistent if all generations contain the same number of quarks and leptons with the charge assignments as they are [4]. Grand unified theories (GUTs) try to address this coincidence by embedding the SM into a larger symmetry group. The higher symmetry would be described by a single gauge group with a single coupling constant. The running couplings of the SM gauge groups would combine into this single parameter at a unification scale. In the SM the couplings run towards each other, but do not exactly meet at the same energy, while in the minimal supersymmetric standard model (MSSM) they meet with sufficient

---

<sup>2</sup>the remaining  $\approx 69\%$  needed to reach the observed zero spacetime curvature are assigned to a cosmological constant or *dark energy*. Its nature is another open question, which is not discussed further here.

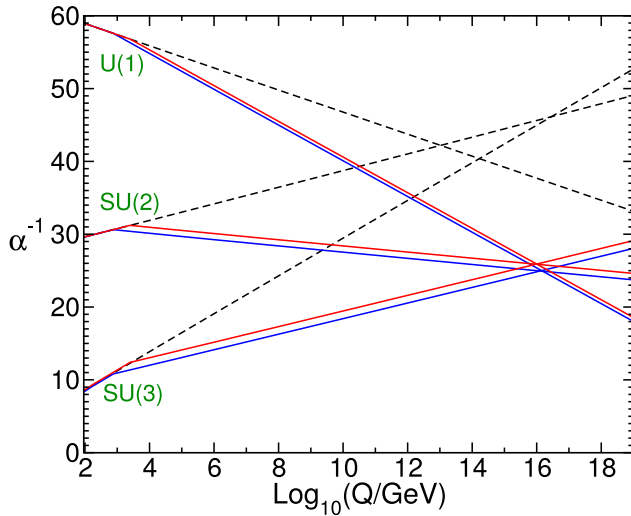


Figure 1.4: Running of gauge couplings in the SM (dashed lines) and the MSSM (solid lines). Figure from Ref. [19].

precision. The unification scale depends on the mass scale of superpartners, since the running of couplings starts to change at this scale. Exact unification at around  $10^{16}$  GeV is possible and combining this with constraints on the absence of proton decay hints to superpartners at the TeV scale [24]. Figure 1.4 shows the running of gauge couplings in the SM and the MSSM with possible unification. If this is not a coincidence, SUSY could lead the way to a GUT.

## Gravity

In the SM there is no description of the gravitational force. It can be described by introducing a Spin 2 field (*graviton*), but such a theory is not renormalisable and can be only used as a low energy approximation. Gravity is much weaker than the other known forces. The scale at which quantum effects in gravity become important is given by the Planck mass,

$$M_{\text{P}} = \sqrt{\frac{\hbar c}{G_{\text{N}}}} = 1.221 \times 10^{19} \text{ GeV}/c^2. \quad (1.25)$$

Supersymmetry is connected to gravity since it is an extension of the Poincaré spacetime symmetry (the symmetry of special relativity). Schematically, the generator of SUSY transformations  $Q$  and its hermitian conjugate  $Q^\dagger$  satisfy an algebra of anticommutation and commutation relations <sup>3</sup>,

<sup>3</sup>See Ref.[19] for the exact form, with correct spinor indices.

$$\{Q, Q^\dagger\} = P^\mu, \quad (1.26)$$

$$\{Q, Q\} = \{Q^\dagger, Q^\dagger\} = 0, \quad (1.27)$$

$$[P^\mu, Q] = [P^\mu, Q^\dagger] = 0, \quad (1.28)$$

with the four-momentum generator of spacetime translations  $P^\mu$ . One incarnation of the connection between gravity and SUSY is that the graviton is a necessary consequence of making SUSY a local symmetry. This is analogous to introducing gauge bosons for local gauge invariance. A supersymmetric theory including gravity in this way is called *supergravity*. Although such a theory is still non-renormalisable, it is hoped to be a low-energy approximation of a more complete description. Modern string theories are based on supergravity.

### The Hierarchy Problem

Due to the observed phenomena that the SM does not describe, it is likely that some new physics exists at higher energy scale. At least at the Planck scale with  $M_P \approx 10^{18}$  GeV something new is expected since quantum gravity effects become relevant. If the scalar Higgs field in the SM couples directly or indirectly to higher scale physics, the Higgs boson squared-mass will receive loop corrections that depend quadratically on the scale of new physics. Consequently, the corrections can become much larger than the measured value of the Higgs boson mass itself. This means the bare mass parameter of the Higgs boson (without corrections) has to be tuned to extreme precision depending on all different contributions from high scale physics, so that with the large corrections, the observed value at the low energy scale comes out correctly. This sensitivity to arbitrary high scale physics is considered unnatural and a hint that there should be a mechanism that avoids these issues.

SUSY protects the Higgs boson mass from these unnatural corrections, since the contributions coming from fermions and bosons (see Figure 1.5) enter with different sign. SUSY theories require the same number of fermionic and bosonic degrees of freedom. In unbroken SUSY the cancellation of the corrections to the Higgs boson mass is exact, to all orders of perturbation theory. Another way of looking at the hierarchy problem is to compare the ultraviolet behaviour of the SM scalar Higgs field to the fermion fields and gauge fields. For fermions, the corrections vanish with vanishing masses, as a consequence of the chiral symmetry. In the limit of zero masses, left-handed particles stay left-handed and right-handed particles stay right-handed. For the gauge bosons, the corrections vanish due to gauge invariance. However, there is no symmetry protecting the scalar Higgs field. SUSY is a candidate for such a symmetry. [25]

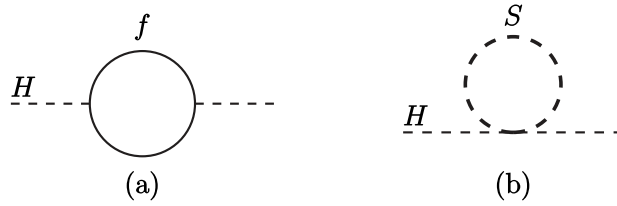


Figure 1.5: One-loop contributions to the Higgs boson mass due to a fermion (a) and a scalar (b). These diagrams are examples for quadratically divergent contributions to the Higgs boson mass (Figure from Ref. [19]).

### 1.3.2 The MSSM

The MSSM is a framework that parametrises any supersymmetric extension of the SM with minimal additional particle content in a general form.

#### Particle content

In a supersymmetric theory each particle must be part of a *supermultiplet* with equal number of bosonic and fermionic degrees of freedom. The fermions in the SM are spin  $\frac{1}{2}$  fermions with 2 degrees of freedom (left- and right-handed). Their superpartners are described by complex scalar fields, such that there is one scalar superpartner for each the left- and right-handed fermions—called *sfermions*. Individual particle names are formed by prepending the letter “s-” to the SM name. The supermultiplets of SM fermions and their scalar superpartners are called *chiral supermultiplets*. For the SM gauge bosons there are spin  $\frac{1}{2}$  superpartners—called *gauginos*. Individual particle names are formed by appending “-ino” to the SM name. The supermultiplets of SM gauge bosons and spin  $\frac{1}{2}$  superpartners are called *gauge supermultiplets*. Unspecified superpartners are referred to as *sparticles*.

As a spin 0 boson, the SM Higgs field resides in a chiral supermultiplet. The mathematical structure of SUSY does not allow Yukawa coupling terms that give mass to both up-type and down-type quarks with only a single Higgs doublet. As a minimal extension, 2 Higgs doublets are needed. Also, the anomaly cancellation conditions mentioned in section 1.3.1 would not hold any more in the MSSM with only one Higgs doublet. The 2 complex Higgs doublets (8 degrees of freedom) lead to 5 Higgs bosons (3 degrees of freedom are absorbed in masses of the gauge bosons in electroweak symmetry breaking). One of them is identified as the SM Higgs boson, the others are yet to be discovered. The 2 Higgs doublets are denoted by  $H_u$  and  $H_d$ .

All fields that are superpartners of the SM fields are denoted by a tilde ( $\tilde{\phantom{x}}$ ). Tables 1.3 and 1.4 list all fields of the chiral and gauge supermultiplets in the MSSM.

Names		spin 0	spin 1/2	$SU(3)_C, SU(2)_L, U(1)_Y$
squarks, quarks ( $\times 3$ families)	$Q$	$(\tilde{u}_L \tilde{d}_L)$	$(u_L d_L)$	$(\mathbf{3}, \mathbf{2}, \frac{1}{6})$
	$\bar{u}$	$\tilde{u}_R^*$	$u_R^\dagger$	$(\bar{\mathbf{3}}, \mathbf{1}, -\frac{2}{3})$
	$\bar{d}$	$\tilde{d}_R^*$	$d_R^\dagger$	$(\bar{\mathbf{3}}, \mathbf{1}, \frac{1}{3})$
sleptons, leptons ( $\times 3$ families)	$L$	$(\tilde{\nu} \tilde{e}_L)$	$(\nu e_L)$	$(\mathbf{1}, \mathbf{2}, -\frac{1}{2})$
	$\bar{e}$	$\tilde{e}_R^*$	$e_R^\dagger$	$(\mathbf{1}, \mathbf{1}, 1)$
Higgs, higgsinos	$H_u$	$(H_u^+ H_u^0)$	$(\tilde{H}_u^+ \tilde{H}_u^0)$	$(\mathbf{1}, \mathbf{2}, +\frac{1}{2})$
	$H_d$	$(H_d^0 H_d^-)$	$(\tilde{H}_d^0 \tilde{H}_d^-)$	$(\mathbf{1}, \mathbf{2}, -\frac{1}{2})$

Table 1.3: SM Fermions and their superpartners in the MSSM (Table from Ref. [19]).

Names	spin 1/2	spin 1	$SU(3)_C, SU(2)_L, U(1)_Y$
gluino, gluon	$\tilde{g}$	$g$	$(\mathbf{8}, \mathbf{1}, 0)$
winos, W bosons	$\tilde{W}^\pm \tilde{W}^0$	$W^\pm W^0$	$(\mathbf{1}, \mathbf{3}, 0)$
bino, B boson	$\tilde{B}^0$	$B^0$	$(\mathbf{1}, \mathbf{1}, 0)$

Table 1.4: SM Gauge bosons and their superpartners in the MSSM (Table from Ref. [19]).

### R-parity conservation

The most general form of a supersymmetric Lagrangian that also respects the SM symmetry groups allows for baryon ( $B$ ) and lepton number ( $L$ ) violating terms. The difference  $B-L$  is conserved in the SM, but could be violated by the  $B$  and  $L$  violating terms that are therefore constrained by experiments. A strong constraint is coming from the absence of proton decay, for example the lifetime for the decay  $p \rightarrow e^+ \pi^0$  is set a lower limit of  $1.6 \times 10^{34}$  years at 90% confidence level as found by the Super-Kamiokande Experiment [26].

Therefore, the  $B$  and  $L$  violating terms are not included in the MSSM. The absence of the terms is guaranteed by a new postulated symmetry. The conserved quantum number of this symmetry, R-parity, is defined for each particle as

$$P_R = (-1)^{3(B-L)+2s}. \quad (1.29)$$

With the Baryon number  $B = \pm \frac{1}{3}$  for the quarks/antiquarks and superpartners,  $B = 0$  for the others, the Lepton number  $L = \pm 1$  for the leptons/antileptons and superpartners,  $L = 0$  for the others and the spin  $s$ . Following this definition, SM particles and Higgs

bosons have  $P_R = 1$  and superpartners have  $P_R = -1$ . The experimental consequences of R-parity conservation are that the LSP has to be stable, therefore being an attractive candidate for dark matter. Furthermore, sparticles can only be produced in even numbers (usually in pairs) and each vertex can only have an even number of sparticles. All sparticle decays end with the LSP (or an odd number of LSPs).

### Soft breaking

To keep the cancellation of quadratic divergencies in the corrections for the Higgs boson mass term in a theory of broken SUSY, the possible terms in the Lagrangian that lead to the breaking are restricted. In particular, the dimensionless couplings of the SM particles and their superpartners have to be kept related (as they are in exact SUSY), for example for the fermions and scalars  $\lambda_S = |\lambda_f|^2$ . This means, the only SUSY violating terms that are allowed are those with couplings of positive mass dimension (not dimensionless). In a theory where supersymmetry is broken that way—called *softly* broken—the corrections to the SM Higgs boson squared-mass depend quadratically on the mass scale  $m_{\text{soft}}$  associated to the SUSY breaking terms (*soft terms*). Therefore, the hierarchy problem reappears if the masses of the superpartners are too large. This is taken as the main motivation to postulate the existence of superpartners not far above the TeV scale.

The soft breaking in the MSSM is described by the following parameters:

- Gaugino mass parameters  $M_1, M_2, M_3$ , corresponding to the U(1), SU(2), SU(3) gauge groups
- Triple scalar couplings—the 3x3 matrices in family space  $\mathbf{a}_u, \mathbf{a}_d, \mathbf{a}_e$  correspond to couplings of sfermions to the Higgs fields. Since they are of the same form as the Yukawa couplings, they preserve gauge invariance, but break SUSY since they are only assigned to sfermions (and not fermions).
- Sfermion 3x3 mass matrices  $\mathbf{m}_Q^2, \mathbf{m}_L^2, \mathbf{m}_{\bar{u}}^2, \mathbf{m}_{\bar{d}}^2$
- SUSY breaking Higgs mass parameters  $m_{H_u}^2, m_{H_d}^2$  and  $b$

With these, the MSSM adds in total 105 parameters to the parameters in the SM. Since almost all of them are related to the soft terms, the phenomenology depends strongly on the exact breaking mechanism, which—ideally—will make predictions for some of the parameters or relations between them.

The matrices  $\mathbf{a}_{u,d,e}$  and  $\mathbf{m}_{Q,L,\bar{u},\bar{d}}^2$  may give rise to additional sources of CP violation and flavour mixings. These effects are heavily constrained by experimental bounds. For example upper limits for the branching fraction of the decay  $\mu \rightarrow e\gamma$  suggest negligible mixing in the lepton sector. Bounds on neutral meson oscillations and other rare decays suggest negligible additional sources of CP violation and negligible new contributions to mixing

in the quark sector. Thus, a simple assumption for the parameters are *flavour blind* soft terms, meaning the  $\mathbf{m}^2$  and  $\mathbf{a}$  matrices are approximately diagonal. This would also lead to degenerate masses for squarks and sleptons with the same electroweak quantum numbers. The assumption might only hold at some high energy scale, for example the unification scale, and the soft parameters are evolved to the low energy scale by renormalisation, preserving the flavour- and CP-conserving properties, but splitting up the masses again.

### Breaking mechanisms

Since almost all parameters of the MSSM are related to the SUSY breaking soft terms, phenomenology is driven by the mechanism that leads to the breaking terms. In the most popular models, the breaking terms are generated by a VEV of the so called *F-term*. This term is originally introduced as an *auxiliary* complex scalar field without a kinetic term to make the SUSY algebra close for off-shell particles in the chiral supermultiplets. A similar term, the *D-term*, corresponding to an auxiliary bosonic field, is introduced for the gauge supermultiplets, but breaking via the D-term can typically only account for a small contribution to the soft breaking terms.

SUSY breaking is usually introduced to occur in a *hidden sector* that is only weakly or indirectly coupled to the visible sector. Phenomenology only depends on the way the breaking is communicated to the visible sector and not on the details of the hidden sector itself. Gravity is a good candidate for a mediation mechanism, since it couples universally to energy and is therefore an unavoidable breaking mechanism in any case. In such gravity mediated SUSY breaking models the mediators are assumed to be at the Planck scale. The other popular option is gauge mediated SUSY breaking (GMSB), where new messenger fields that share gauge interactions with the MSSM fields are introduced. Those messengers can be relatively light. Both breaking models assume supergravity and hence the existence of gravitinos. One of the main phenomenological differences is that the gravitinos in GMSB models will be the LSPs, while they are heavy in gravity mediated models, leading to the lightest neutralino (described below) being the LSP [19, 25]. The models considered for analysis in this thesis target this scenario.

### Mass spectrum

Due to SUSY breaking, the masses of the undiscovered particles in the MSSM depend on many parameters. Predictions about possible mass ranges and hierarchies are made by assuming specific breaking mechanisms or unification schemes and also by experimental constraints—like the flavour blindness of SUSY breaking discussed above.

In the MSSM, electroweak symmetry breaking is generalised to the case of two Higgs doublets. The VEV  $v$  of the SM Higgs field (see Equation 1.16) can be connected with the VEVs of the two MSSM Higgs doublets  $H_u$  ( $v_u$ ) and  $H_d$  ( $v_d$ ),

$$v_u^2 + v_d^2 = v^2. \quad (1.30)$$

The ratio of the VEVs is written as

$$\tan \beta = v_u/v_d \quad (1.31)$$

The massive Higgs bosons that are left after electroweak symmetry breaking are two CP even states  $h^0$  and  $H^0$ , one CP odd state  $A^0$  and two charged Higgs bosons  $H^\pm$ . Usually, the state  $h_0$  is identified with the SM Higgs boson. Before its discovery a prediction from the MSSM was an upper bound on its mass of  $\approx 135$  GeV, at that time a more strict requirement than what was known from the SM—in good agreement with the now observed 125 GeV.

After electroweak symmetry breaking the higgsinos and electroweak gauginos mix to form mass eigenstates. The charged higgsinos and the charged winos will form two mass eigenstates called *charginos* ( $\chi_i^\pm, i = 1, 2$ ), the neutral higgsinos and neutral wino/bino will form four mass eigenstates called *neutralinos* ( $\chi_i^0, i = 1, 2, 3, 4$ ). The label  $i$  is assigned in order of ascending masses.

Squarks and sleptons can in principle also mix, but according to the flavor blindness hypothesis, mixing due to the soft terms is assumed to be negligible. Therefore mixing mainly occurs between superpartners of the left- and right-handed fields due to the Yukawa couplings, which are only significant for the third generation squarks and sleptons. The mixed mass eigenstates for the third generation sfermions are called  $(\tilde{t}_1, \tilde{t}_2)$ ,  $(\tilde{b}_1, \tilde{b}_2)$  and  $(\tilde{\tau}_1, \tilde{\tau}_2)$ . The index 1 stands for the lighter of the two sparticles. The significant Yukawa couplings lead to lower masses when they are evolved from a unification scale down to the electroweak scale, so the sfermions of the third generation are assumed to have lower masses than the first and second generation. Therefore, in many phenomenological models, the  $\tilde{t}_1$  is the lightest squark and the first and second generation squarks have degenerate masses. Light third generation squarks are also favourable from naturalness arguments. The correction terms to the Higgs boson mass from sfermions in broken SUSY are proportional to the Yukawa couplings, so the largest contribution comes from the third generation. The argumentation for the sleptons is similar. The gluino mass is determined by the gluino mass parameter  $M_3$  and (potentially large) corrections due to the strong interaction with the squark-quark supermultiplets. Depending on the model it can be lighter or heavier than the squarks. Usually the gluino mass parameter  $M_3$  is assumed to be larger than the bino and wino mass parameters  $M_1$  and  $M_2$ . For example in GMSB and minimal supergravity (MSUGRA) models the prediction is roughly

$$M_3 : M_2 : M_1 \approx 6 : 2 : 1, \quad (1.32)$$

so the gluino mass is expected to be larger than the masses of the charginos and neutralinos.

### 1.3.3 Production of gluinos and squarks at the LHC

If gluinos and squarks are within the reach of the LHC, they can be produced in proton-proton collisions via the strong interaction. Therefore, gluino and squark production would

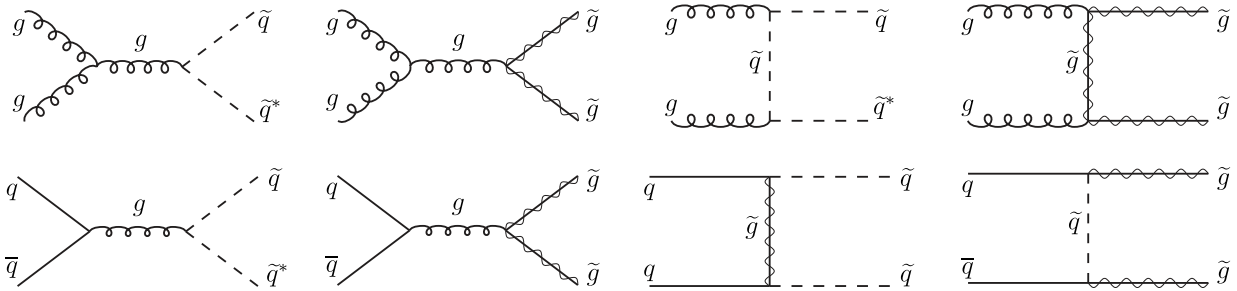


Figure 1.6: Example diagrams for leading order production processes of gluino and squark pairs in proton-proton collisions [19].

be the dominant production channel of SUSY particles. This analysis focuses on scenarios where either the gluinos or the squarks are accessible from direct pair production. Figure 1.6 shows example diagrams for the production processes.

The cross sections are calculated up to NLO QCD corrections with resummation of soft gluon emission at next-to-leading-logarithmic (NLL) accuracy, [27–31] using the prescriptions from the LHC SUSY cross section working group [32]. For gluino pair production the squarks are assumed to be effectively decoupled. For squark pair production, the gluinos are assumed to be effectively decoupled. Furthermore, only the superpartners of the left-handed first and second generation quarks are assumed to be produced and to be degenerate in mass. Figure 1.7 shows the resulting cross sections for gluino and squark pair production depending on the masses.

### 1.3.4 Decay models of gluinos and squarks in this analysis

Both the design of the search strategy and the interpretation of results are based on specific scenarios for the decay of gluinos and squarks.

#### Simplified models

Simplified models are widely used in searches for new physics at the LHC [33, 34]. They can capture a large range of possible phenomena by a small set of parameters that have a large effect on the observables. In contrast, very constrained phenomenological models might still have an unmanageable large number of parameters which potentially have only small effects on observables.

In this work, three simplified models for gluino and squark decays are used. The first two models describe decays via an intermediate chargino  $\tilde{\chi}_1^\pm$  to the LSP which is assumed to be the lightest neutralino  $\tilde{\chi}_1^0$ . These models are called *one-step* models. The branching fractions are assumed to be 100%. A squark decays into a  $\tilde{\chi}_1^\pm$  via the emission of one quark. In the gluino decays, two quarks are emitted. The decay is mediated by a heavy (decoupled) squark. The  $\tilde{\chi}_1^\pm$  decays to a LSP via the emission of a  $W$  boson. Three

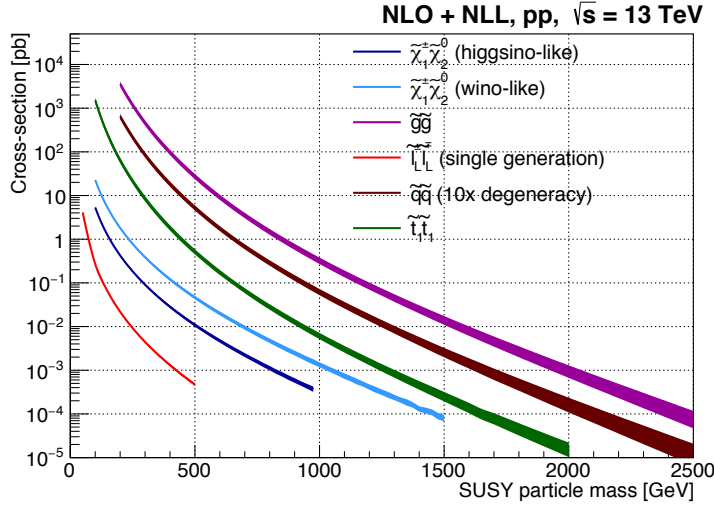


Figure 1.7: Cross sections for pair production of different SUSY particles in 13 TeV proton-proton collisions [32]. This analysis uses the shown  $\tilde{g}\tilde{g}$  and the  $\tilde{q}\tilde{q}$  cross sections, where the  $\tilde{q}\tilde{q}$  cross sections are scaled by  $\frac{2}{5}$  to account for the  $4\times$  instead of  $10\times$  degeneracy.

parameters define the models: the gluino/squark mass  $m_{\tilde{g}/\tilde{q}}$ , the LSP mass  $m_{\tilde{\chi}_1^0}$  and the ratio of mass differences between the chargino and the LSP and the gluino/squark and the LSP,  $x = \frac{m(\tilde{\chi}_1^\pm) - m(\tilde{\chi}_1^0)}{m(\tilde{g}/\tilde{q}) - m(\tilde{\chi}_1^0)}$ . In the third model, the gluino *two-step* model, the chargino is assumed to decay via another step through the second lightest neutralino  $\tilde{\chi}_2^0$  into an LSP. In the  $\tilde{\chi}_2^0$  decay a  $Z$  boson is emitted. The two-step models used in this analysis are defined by two parameters, the gluino mass and the LSP mass. To fix the intermediate particle masses the chargino mass is required to be the average of the gluino and the LSP mass and the second neutralino mass the average of the chargino and LSP mass—so in each intermediate step, half of the remaining visible decay energy is carried away by SM particles. Figure 1.8 shows the Feynman diagrams for the simplified models.

## pMSSM

Not all values in the set of the 105 parameters of the MSSM mentioned in Section 1.3.2 are phenomenologically viable. The necessity of flavour blind breaking terms constrains additional phases and mixings, also leading to degenerate masses of the first and second generation sfermions. In the Higgs sector there are many constellations that do not lead to electroweak symmetry breaking, so the parameters can also be reduced by imposing the required relations between them. This leads to the 19 parameters of the pMSSM [35]:

- $\tan\beta$ : the ratio of the VEVs of the two Higgs doublet fields
- $M_A$ : the mass of the CP odd Higgs boson

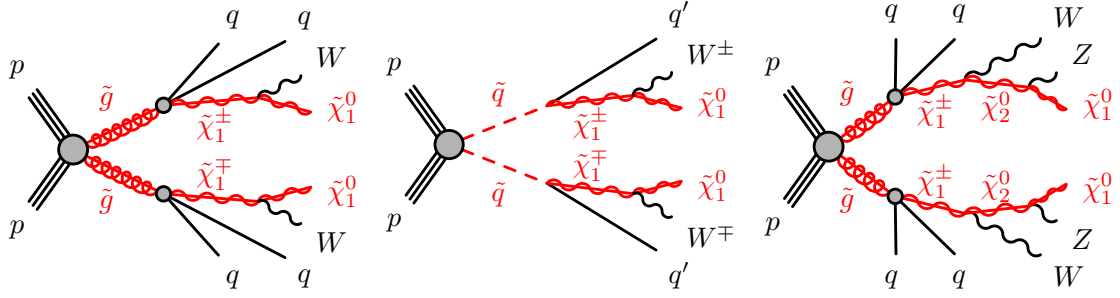


Figure 1.8: Simplified models for gluino one-step (left), squark one-step (middle) and gluino two-step (right) decays.

- $\mu$ : the Higgs-higgsino mass parameter
- $M_1, M_2, M_3$ : the gaugino mass parameters
- $m_{\tilde{q}}, m_{\tilde{u}_R}, m_{\tilde{d}_R}, m_{\tilde{l}}, m_{\tilde{e}_R}$ : determining the masses of first and second generation sfermions
- $m_{\tilde{Q}}, m_{\tilde{t}_R}, m_{\tilde{b}_R}, m_{\tilde{L}}, m_{\tilde{\tau}_R}$ : determining the masses of the third generation sfermions
- $A_t, A_b, A_\tau$ : triple scalar couplings for the third generation sfermions

The set of models from the 19-dimensional parameter space used in this work was designed by an ATLAS search for all hadronic events with large jet multiplicities [36], motivated by models that were not excluded by the ATLAS pMSSM summary analysis with LHC 7 and 8 TeV data [37]. The models are selected to have a bino-dominated neutralino  $\tilde{\chi}_1^0$  LSP, fixed at low mass via  $M_1 = 60$  GeV and a Higgsino dominated multiplet (leading to degenerate masses), consisting of two neutralinos  $\tilde{\chi}_2^0$  and  $\tilde{\chi}_3^0$  and a chargino  $\tilde{\chi}_1^\pm$ , defined by the parameter  $\mu$ . The other parameter in the models is the gluino mass parameter  $M_3$ . The remaining parameters are fixed to values that make the other particles kinematically inaccessible. The squark and slepton mass parameters and  $A_t, A_b$  are set to 5 TeV,  $m_A = M_2 = 3$  TeV,  $A_\tau = 0$  and  $\tan\beta = 10$ . Mass spectra were calculated by the SOFTSUSY [38] and the decay branching ratios by the SDECAY/HDECAY programs [39]. Figure 1.9 shows an example for a mass spectrum and a Feynman diagram for a likely decay. These models are referred to as *pMSSM models* in this thesis.

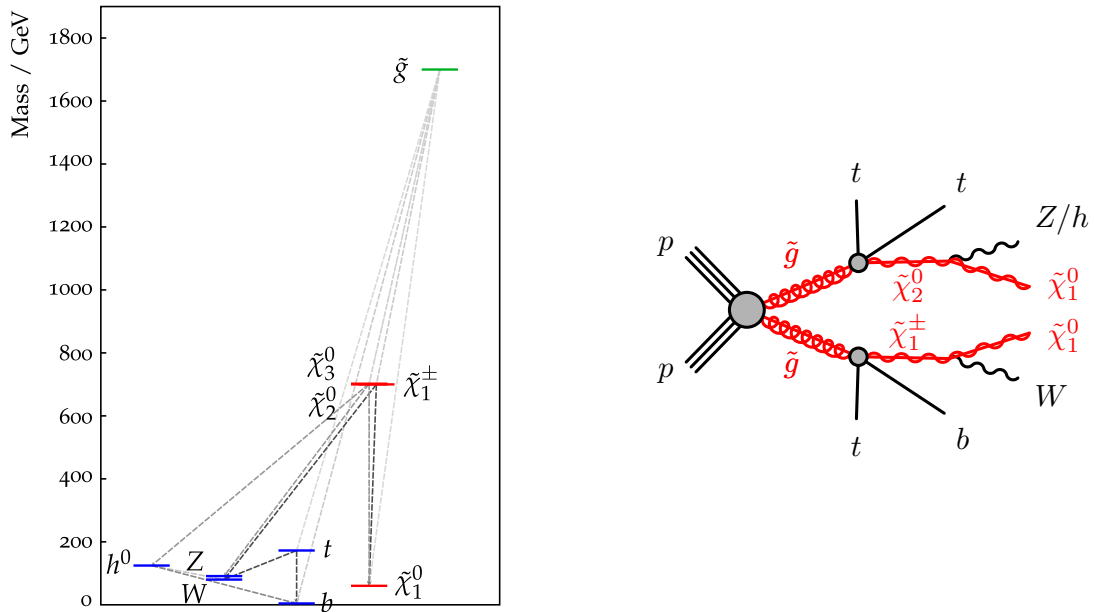


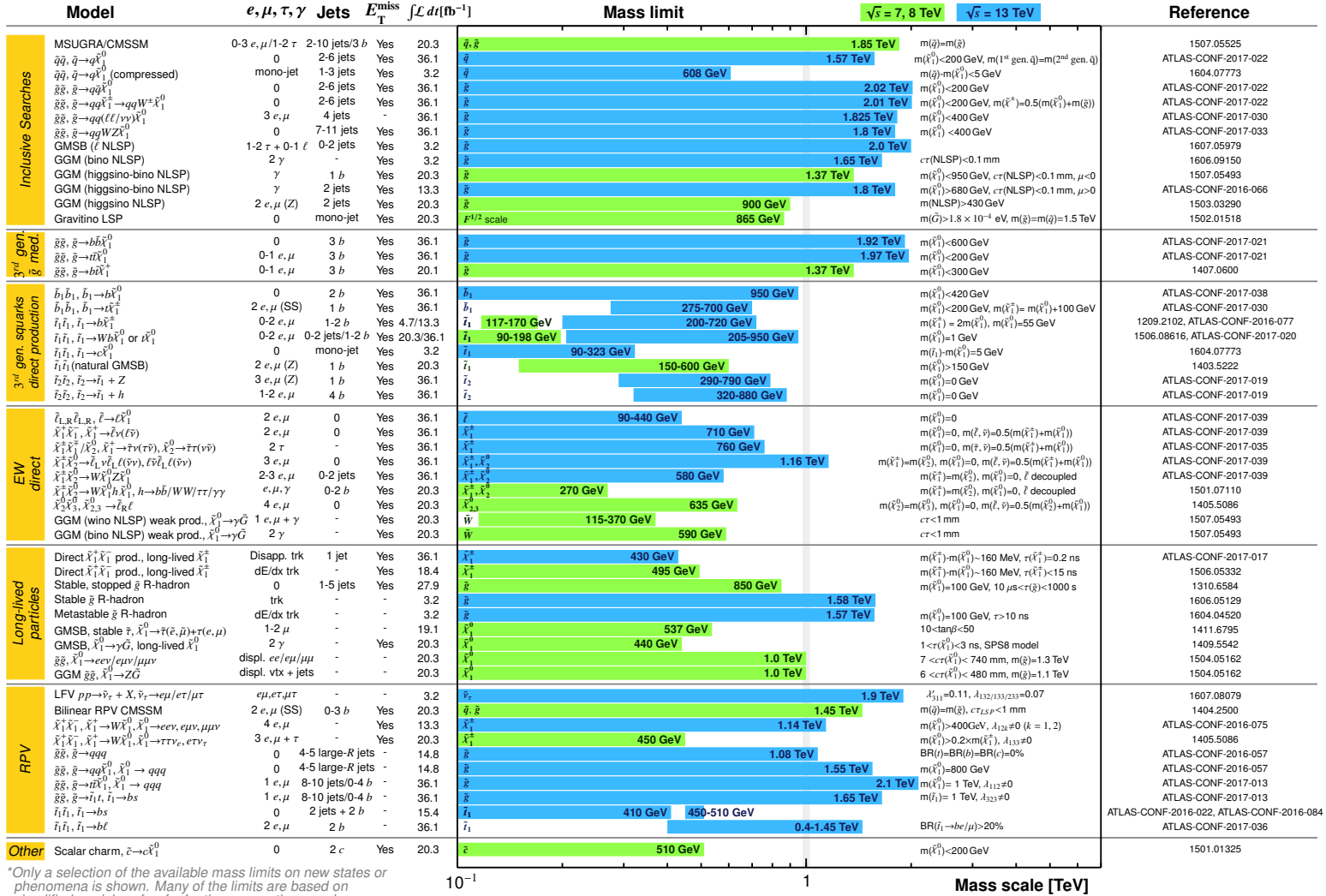
Figure 1.9: Example mass spectrum (left) and likely decay (right) for a pMSSM model with a gluino mass of 1700 GeV and a higgsino/chargino mass of 700 GeV. The plot on the left side includes the relevant SM particles for illustration. The dashed lines indicate possible decays. The plot was generated by the PYSLHA program [40].

### 1.3.5 Current constraints from direct searches

In addition to the constraints from flavour physics and absence of proton decay already mentioned above and other indirect searches not mentioned here, there is a large number of lower bounds on sparticle masses from direct searches. Some limits from the Large Electron-Positron Collider (LEP) experiments are still significant, due to their general (model independent) nature. They are mainly set by the high energy LEP2 data up to 208 GeV. Due to the precise knowledge of the collision energy, missing momentum could also be reconstructed along the beam axis direction. This leads to limits in a broad range of scenarios for the lightest charginos of 103.5 GeV and 92.9 GeV for small mass difference between chargino and LSP [41]. Limits on the invisible width of the  $Z$  boson lead to a rather general limit for neutralinos of 45.5 GeV, except for scenarios with vanishing coupling [10]. Most of the results from the Tevatron experiments are now superseded by the LHC results. Many analyses using the 13 TeV data from the 2015 and 2016 LHC runs have already been published by the ATLAS and CMS collaborations. Limits on the strongly produced sparticles have reached the TeV scale, in case of light squarks the 1 TeV boundary is exceeded in many scenarios, in case of gluinos the lower bound reached 2 TeV for most simplified models with non-compressed spectra. Figure 1.10 shows a summary for the limits from ATLAS search results as of May 2017. The results of the CMS experiment yield similar limits [42]. A more complete overview, including the results from LHC data up to summer 2015 can be found in Ref. [10].

ATLAS SUSY Searches\* - 95% CL Lower Limits  
May 2017

ATLAS Preliminary  
 $\sqrt{s} = 7, 8, 13$  TeV



\*Only a selection of the available mass limits on new states or phenomena is shown. Many of the limits are based on simplified models, c.f. refs. for the assumptions made.

Figure 1.10: Summary of sparticle mass limits from the ATLAS experiment, based on different simplified and phenomenological models [43].

## 1.4 Monte-Carlo event generation

To extract theory predictions on general observable quantities in p-p collisions, events are typically simulated. A review on currently available generator programs and techniques can be found in Ref. [44].

The simulation involves QCD interactions in both the hard regime where the asymptotical freedom allows perturbative calculation and the soft regime where this is not possible. The proton is a composite object. To describe scattering of protons, the cross section calculation has to be factorised in a hard scattering cross section of partons (quarks and/or gluons) that can be calculated perturbatively and the parton distribution functions (PDFs) of the incoming partons. The PDFs describe the probability of finding a certain parton with momentum fraction  $x$  of the proton in a collision. This holds in the infinite momentum frame where the parton momenta are collinear with proton momentum. At high  $x$ , the PDFs are dominated by the 3 valence quarks of the proton. At lower  $x$ , gluons and sea-quarks (from  $g \rightarrow q\bar{q}$  splitting) dominate. So far it is not possible to calculate the PDFs from first principles. Therefore, they are fit to data. The ones used for LHC simulations [45–47] are mainly based on electron-proton data from the HERA experiments, but also include proton-proton data from Tevatron and LHC. The PDFs depend on the momentum transfer  $Q^2$ , but once known for a certain momentum transfer, they can be evolved by QCD predictions to different scales. At higher momentum transfers, sea-quarks and gluons dominate more and more. Figure 1.11 shows an example for proton PDFs at different scales.

The next step in the simulation chain is the parton shower. Quarks in the final state can radiate gluons, and gluons can also radiate gluons or split into a quark and an antiquark. This is called final state radiation (FSR) and leads to a cascade of softer and softer partons that will eventually arrive at the scale where they hadronise. Similar to the evolution of PDFs, QCD can predict the splitting probabilities for partons, so this cascade can be simulated step by step for each parton. Initial state partons can also radiate, which is called initial state radiation (ISR). The description is similar, but here the evolution is done backwards and the radiation probability has to take into account that with additional radiation the initial parton has a higher momentum fraction  $x$  with a different probability in the PDF, so in situations where a higher  $x$  has lower probability, less ISR is present.

Modern event generators also have the ability to merge the parton shower process with NLO calculations that already have the first additional emission included in the matrix element. This is expected to give a more accurate description, especially for regimes with very hard radiation. Furthermore, tree level diagrams can be calculated separately for different number of hard emissions and merged with each other and the parton shower procedure. There also exist methods to combine this with the NLO merging procedure.

The hadronisation of partons is in the non perturbative regime of QCD that cannot be calculated from first principles. Therefore, hadronisation models with tunable parameters that can be fitted to data are used. Finally, the decay of these hadrons has to be simulated.

## MSTW 2008 NLO PDFs (68% C.L.)

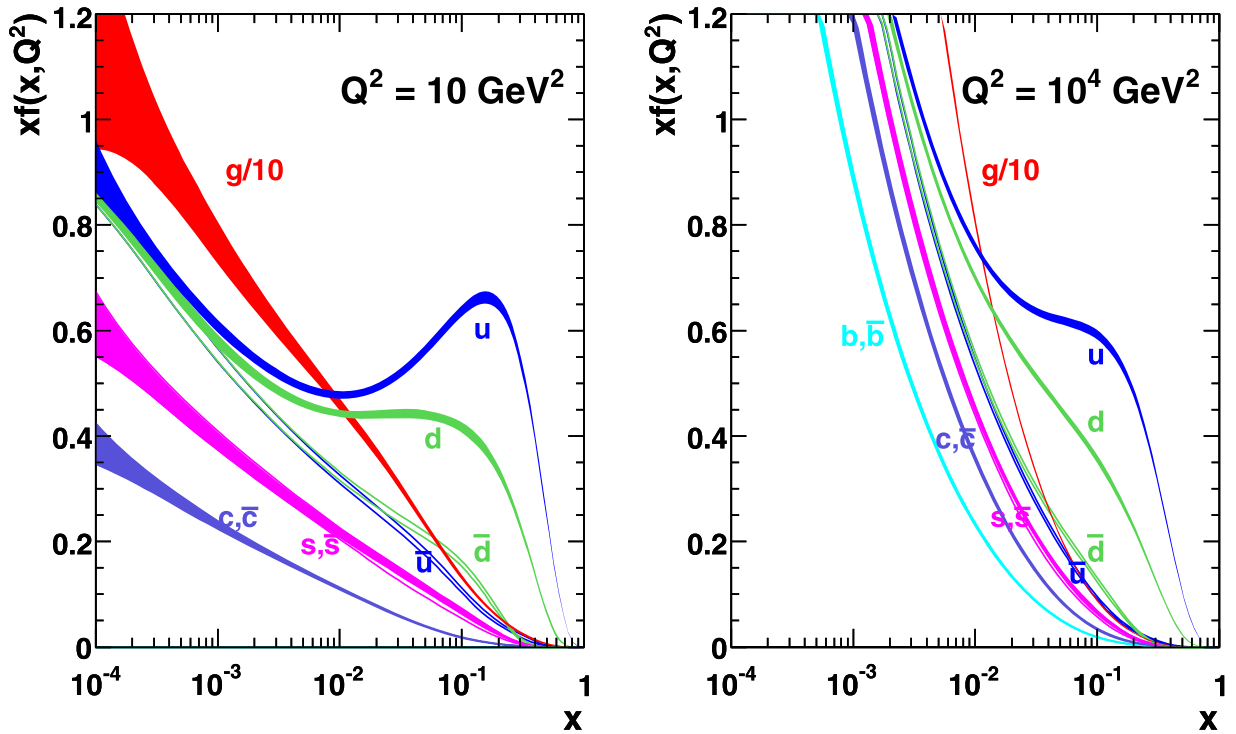


Figure 1.11: Example for parton distribution functions at 2 different scales [46]

All steps of the event generation are visualised in Figure 1.12.

Overlaid to the hard scattering event there can be an *underlying event*, originated from secondary, typically softer interactions of partons in the same protons that participate in the hard collision. Furthermore, at the high luminosity of the LHC, multiple p-p collisions (*pileup*) happen at the same time. Both the underlying event and additional collisions have to be simulated by models for soft QCD scattering of protons, referred to as *minimum bias* events.

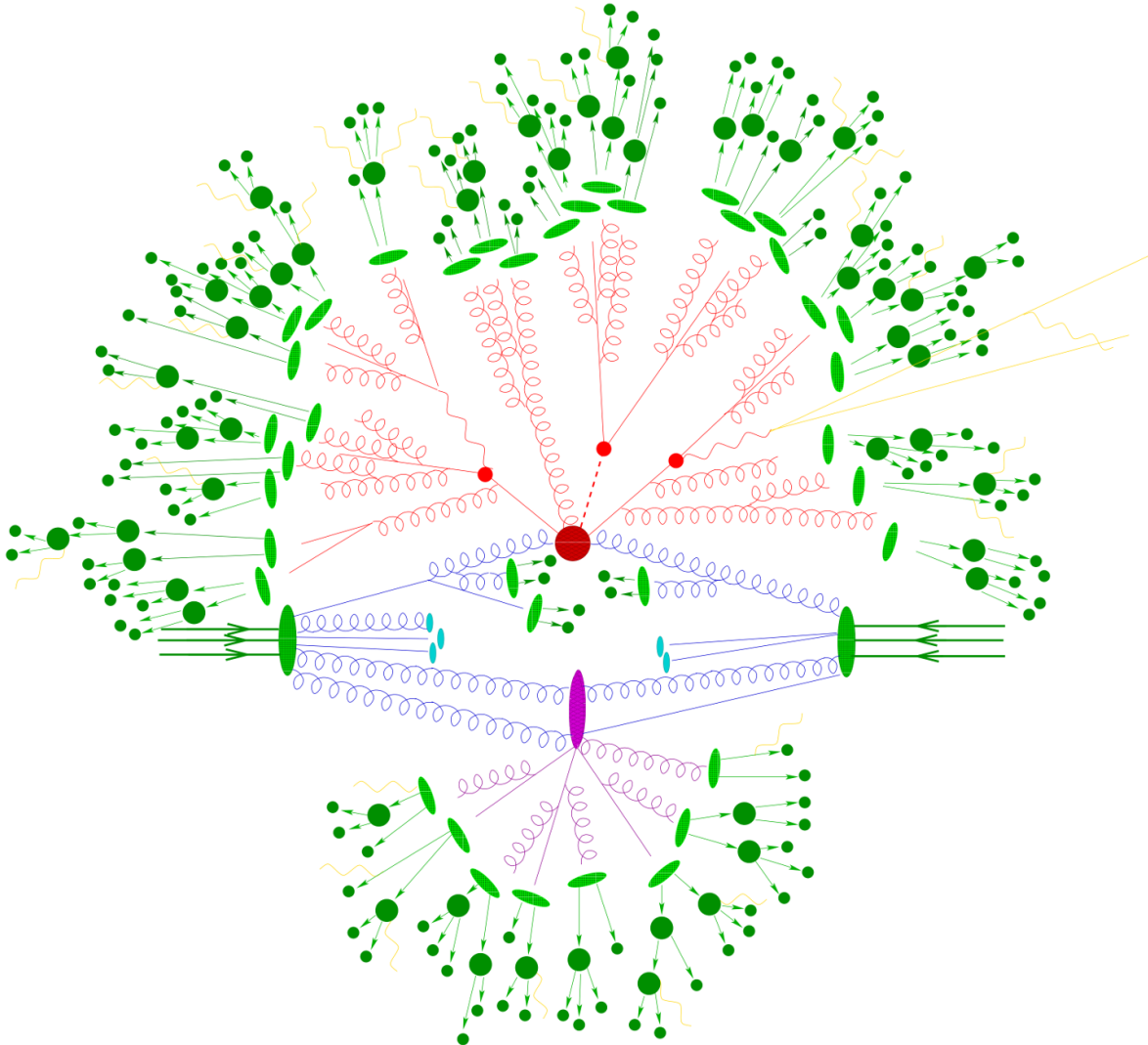


Figure 1.12: Pictorial representation of a simulated  $t\bar{t}h$  event in p-p collisions. The big red blob corresponds to the hard interaction. The small red blobs show the decay vertices of the Higgs boson and the top quarks. Additional QCD radiation and the parton shower is also drawn as red lines. Hadronisation of partons is symbolised by the light green ellipses and the decay of hadrons by the dark green blobs. The yellow lines show photon radiation. A second parton collision is shown with a purple blob. (Figure from Ref. [48]).



# Chapter 2

## The LHC and ATLAS

### 2.1 The LHC

The Large Hadron Collider (LHC) [49] is a particle accelerator and collider at the European Organization for Nuclear Research (CERN, french: *Conseil Européen pour la Recherche Nucléaire*), located near Geneva in the 26.7 km long ring tunnel that was previously housing the LEP machine. It is capable of colliding protons (p) and heavy ions. Following the LEP tunnel geometry, the LHC has eight arcs and eight straight sections. Detectors that record events from collisions are installed in four of the straight sections. The straight sections are numbered clockwise, starting from Point 1, close to the CERN Meyrin site, where the ATLAS (A Toroidal LHC ApparatuS) detector is located. Three more straight sections are equipped with beam crossing points. The Compact Muon Solenoid (CMS) experiment is located at point 5, opposite of the ring and A Large Ion Collider Experiment (ALICE) and Large Hadron Collider beauty (LHCb) experiment are located at point 2 and 8 in the octants next to ATLAS. While ATLAS and CMS are multi-purpose detectors, ALICE is specialised in heavy ion physics and LHCb on b-physics.

The design centre-of-mass energy  $\sqrt{s}$  in p-p collisions is 14 TeV. The limiting factor for the achievable energy is the strength of the magnetic field in the dipole magnets that are used to keep the particles on the ring. For the nominal beam energy of 7 TeV, the magnetic field in the dipoles has to reach 8.33 T. Particles circulating in the LHC are organised in bunches, due to the acceleration with radio frequency cavities. The acceleration cavities of the LHC are located at point 4. The nominal number of bunches in the ring is 2808 with a bunch spacing of around 25 ns. Before reaching the LHC, the protons bunches pass through an injection chain consisting of CERNs acceleration structure that was already present before the LHC was build (see Fig. 2.1 for an overview). The protons pass the chain Linac2 – Booster – Proton Synchrotron (PS) – Super Proton Synchrotron (SPS) and finally reach the LHC with an injection energy of 450 GeV from which they are accelerated to nominal beam energy.

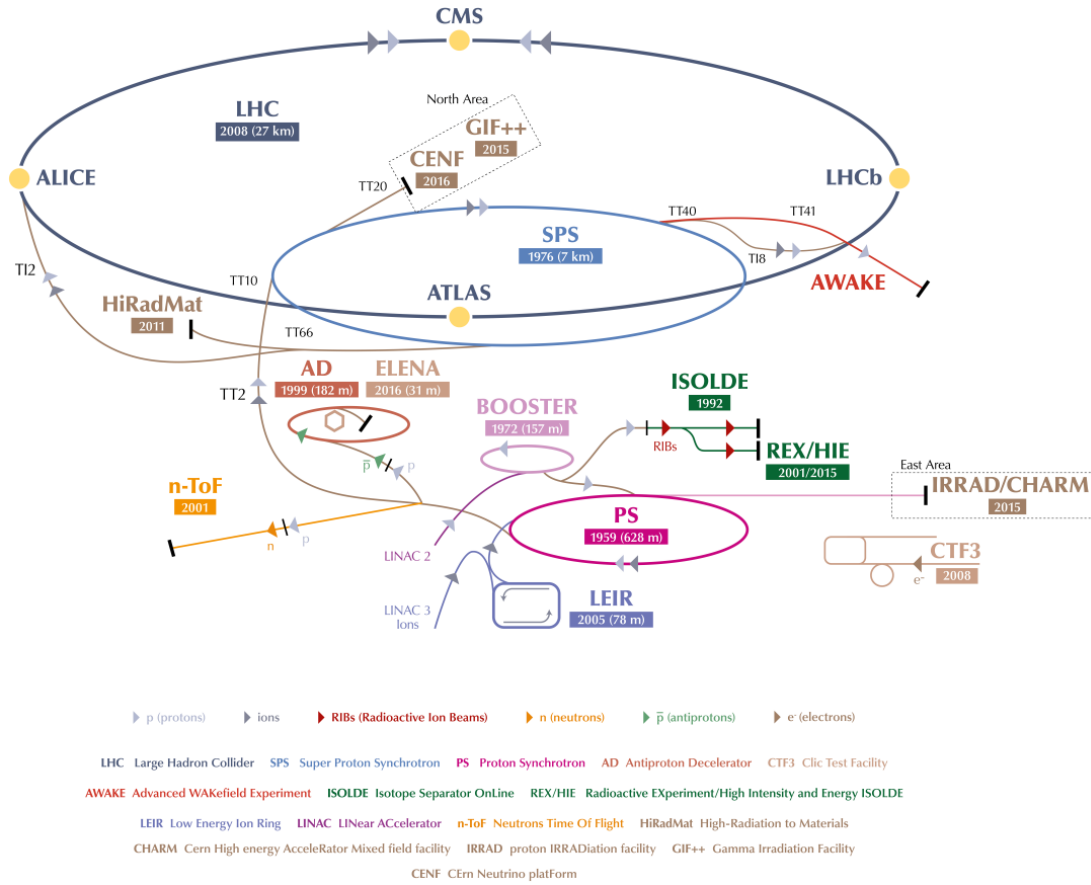


Figure 2.1: The CERN accelerator complex as of 2016 [50]

The design peak luminosity for the high luminosity experiments ATLAS and CMS is  $L = 10^{34} \text{ cm}^{-2}\text{s}^{-1}$ . The luminosity determines the expected event rate and the integrated luminosity  $\mathcal{L} = \int L dt$  determines the total number of expected events with a certain cross section  $\sigma$

$$N_{\text{event}} = \mathcal{L}\sigma_{\text{event}}$$

The achieved luminosity depends on the beam parameters and the number of particles in the beam. In the first p-p run (Run-1) of the LHC from 2010-2012 a beam energy of 3.5 TeV (2010-2011) and 4 TeV (2012) was reached. The second run (Run-2) started in 2015 with a beam energy of 6.5 TeV ( $\sqrt{s} = 13 \text{ TeV}$ ). The design luminosity at ATLAS and CMS was first reached in June 2016.

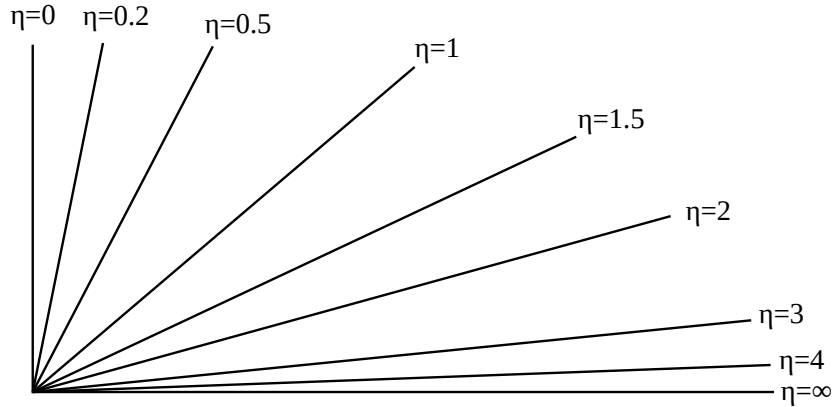


Figure 2.2: Angles corresponding to different values of pseudorapidity ( $\eta$ ) in the  $y$ - $z$  plane

## 2.2 The ATLAS Experiment

As one of two general purpose detectors, the ATLAS experiment is designed to cover a wide range of possible signatures at high luminosity. It is located at point 1 of the LHC, opposite to the main entrance of the CERN Meyrin site, in a cavern around 100 m underground. A detailed description of the experiment can be found in Ref [51].

### 2.2.1 Coordinate System

Events in the ATLAS detector are described by a right-handed coordinate system with the origin at the nominal interaction point in the centre of the detector. The  $z$ -axis points towards the beam direction, the positive  $x$ -axis towards the centre of the LHC ring and the positive  $y$ -axis upwards. The azimuthal angle  $\phi$  is measured around the beam axis, the polar angle  $\theta$  is measured from the beam axis. The rapidity  $y$  is defined by

$$y = \frac{1}{2} \ln \left( \frac{E + p_z}{E - p_z} \right) = \tanh^{-1} \left( \frac{p_z}{E} \right)$$

It is preferred over the polar angle  $\theta$ , since differences in  $y$  are invariant under Lorentz boosts in direction of the beam axis. The pseudorapidity  $\eta$  is defined as

$$\eta = -\ln \tan(\theta/2)$$

The pseudorapidity corresponds to the rapidity in the limit  $p \gg m$  [10]. Figure 2.2 shows the angles corresponding to different values of  $\eta$ . The separation of objects is often measured in terms of the distance in pseudorapidity-azimuthal angle space,  $\Delta R = \sqrt{\Delta\eta^2 + \Delta\phi^2}$ .

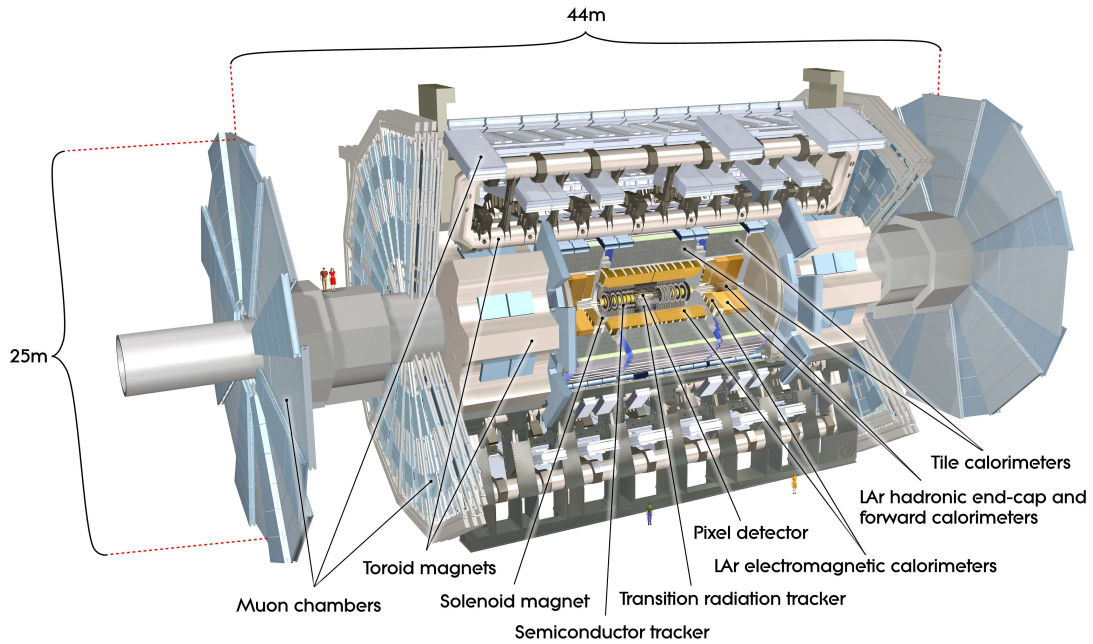


Figure 2.3: Overview of the subsystems of the ATLAS experiment [51]

## 2.2.2 Subdetectors

ATLAS consists of multiple subsystems. Most of them have both barrel-shaped layers to detect particles travelling towards the central (small  $|\eta|$ ) part of the detector and disc-shaped end-caps to cover the forward and backward (large  $|\eta|$ ) region (see Figure 2.3).

### Inner detector

The innermost layers record the tracks of charged particles. The whole inner detector (ID) is embedded in a 2 T solenoid magnet. This leads to a magnetic field in beam direction that bends charged particle tracks in the x-y (transverse) plane. The bending is used to determine the particles momentum and sign of the charge.

Three detector systems are used. The first two systems consist of Pixel detectors and the silicon microstrip trackers of the Semiconductor Tracker (SCT). They provide precision tracking in the range up to  $|\eta| < 2.5$ . High precision is needed especially for detecting secondary vertices from particles with significant lifetime (e.g.  $\tau$  leptons, B-hadrons). To improve the vertex and track resolution and to provide redundancy in higher radiation environments (increased luminosity) the barrel pixel system was upgraded before the start of the second LHC run in 2015 [52] by a new innermost layer around a smaller beam pipe, the Insertable B-Layer (IBL) [53]. The third system, the Transition Radiation Tracker (TRT) uses straw tubes for tracking. In addition to the tracked particle, the straw tubes can

detect transition radiation photons which can be used to improve electron identification. The TRT provides tracking in the range up to  $|\eta| < 2$ .

### Calorimeters

The calorimeters are designed to contain electro-magnetic (EM) and hadronic showers and to measure their energies. The information from the calorimeters is also used for triggering. Both the EM calorimeter and the hadronic calorimeter are sampling calorimeters, consisting of alternating layers of absorbing and active material. The EM calorimeter is based on liquid argon (LAr) detectors with accordion-shaped kapton electrodes and lead absorber plates. The barrel hadronic calorimeter is based on scintillating tiles (Tile calorimeter) and lead absorber plates. In the end-cap, the hadronic calorimeter is based on LAr detectors with copper as absorber material. In terms of radiation lengths ( $X_0$ ), the EM calorimeter has a thickness of  $> 22 X_0$  in the barrel and  $> 24 X_0$  in the end-cap. The hadronic calorimeter provides around 9.7 interaction lengths ( $\lambda$ ) in the barrel and  $10 \lambda$  in the end-cap.

The highest precision (highest granularity) in the calorimeters is achieved in the region  $|\eta| < 2.5$ , but coarser granularity calorimeters extend up to  $|\eta| < 3.2$ . An additional set of LAr forward calorimeters provide both electromagnetic and hadronic calorimetry in the region  $3.1 < |\eta| < 4.9$ .

### Muon system

Muons pass through the calorimeter system with little interaction and end up in the muon system. An additional system of air-core toroid coils provides a 0.5 T (barrel) to 1 T (end-cap) magnetic field around the beam axis that bends the muon tracks in the r-z ( $r^2 = x^2 + y^2$ ) plane. This allows an independent measurement of the muon momenta, in addition to the inner detector track.

Different detector systems are used for precision tracking and for triggering. Monitored Drift Tube (MDT) chambers contain gas filled drift tubes, aligned tangential to circles around the beam axis. Therefore, they provide precision measurement in bending direction of the magnetic field. Cathode Strip Chambers (CSCs) are multi-wire proportional chambers with cathode strips. They are used for precision tracking in the innermost layer in the end-cap region at large pseudorapidities ( $2 < \eta < 2.7$ ). The muon trigger relies on Resistive Plate Chambers (RPCs) and Thin Gap Chambers (TGCs). While the RPCs do not use wire anodes, the TGCs are multi-wire proportional chambers.

In addition to triggering, the fast response of RPCs and TGCs is used to identify the bunch crossing to which a muon track corresponds. Also, these detectors provide a measurement of the coordinate orthogonal to the precision tracking chambers.

### 2.2.3 Forward detectors

At larger distance from the interaction point three smaller detector systems are located in the very forward region. The first system, Luminosity measurement using Cerenkov Integrating Detector (LUCID) is located at a distance of  $\pm 17$  m from the interaction point. It is primarily dedicated to online luminosity monitoring from inelastic p-p scattering. The Zero-Degree Calorimeters (ZDC) are located at the point where the LHC beam pipe is divided into two pieces,  $\pm 140$  m from the collision centre. The ZDC detect forward neutrons, which is a key ingredient to determine the centrality of heavy ion collisions. The third system, Absolute Luminosity For ATLAS (ALFA), determines the luminosity via small angle elastic scattering and is located at  $\pm 240$  m from the interaction point.

### 2.2.4 Trigger system

The bunch crossing rate of 40 Mhz is too large to fully process and store all events. The ATLAS trigger system consists of two levels to reduce the rate to around 1 kHz [54] of event data that is stored to tape and reconstructed. The level one (L1) trigger, uses information from a subset of detector systems (reduced granularity information from calorimeters and muon trigger chambers). The L1 trigger system runs on custom hardware processors and the decision is taken within  $2.5 \mu\text{s}$ , including the travelling time of signal between detector and trigger system. To achieve this, the hardware involved in the L1 system is installed underground in or close to the ATLAS cavern [55]. The L1 procedure defines Regions-of-Interest (RoIs) where the selection process has identified interesting features. The output rate of the L1 trigger is around 100 kHz. The second level, the High-Level Trigger (HLT) is run entirely software based on a processor farm on the surface above the ATLAS detector. At the HLT both partial and full event data can be processed to have a selection that is very similar to the one used in the analyses. This allows good efficiency for triggering the signatures of interest.

### 2.2.5 Data taking in 2015 and 2016

The p-p data used in this analysis recorded in 2015 and 2016 at  $\sqrt{s} = 13$  TeV. In total, ATLAS recorded an integrated luminosity of  $3.9 \text{ fb}^{-1}$  in 2015 and  $35.6 \text{ fb}^{-1}$  in 2016.  $36.1 \text{ fb}^{-1}$  are usable for the physics analysis of this thesis. Figure 2.4 shows the total delivered integrated luminosity for for all p-p runs since 2011 and the instantaneous luminosity that was reached during the different runs of 2016. On average, there was a mean number of interactions per bunch crossing (pileup) of 13.7 in 2015 and 24.9 in 2016 [56].

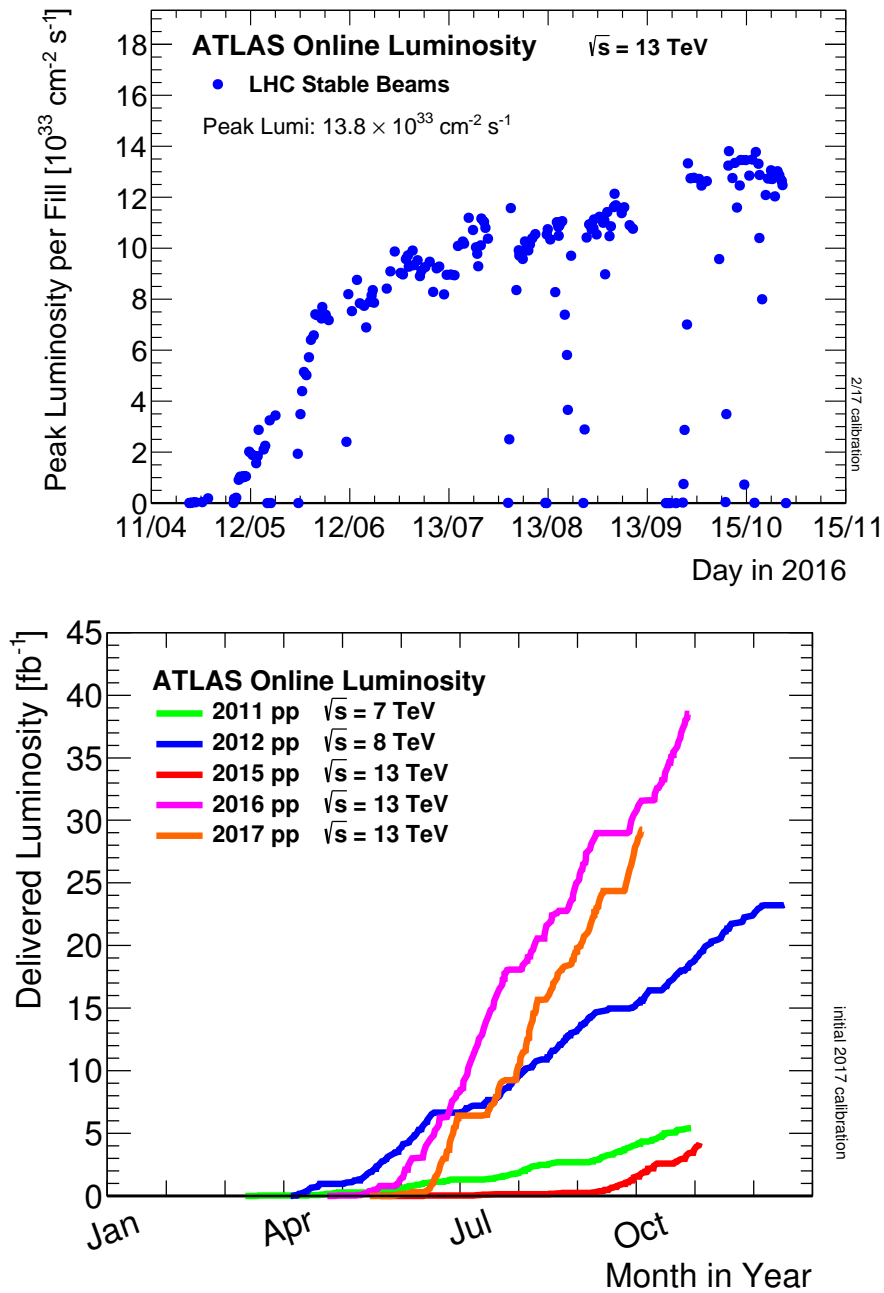


Figure 2.4: Peak luminosity for the 2016 runs (top) and integrated luminosity for all runs since 2011 (bottom) at ATLAS. [56]



# Chapter 3

## Analysis Overview

### 3.1 Inclusive search in 1-lepton final states

Many searches for supersymmetry focus on scenarios where top squarks are relatively light at the TeV scale. This is motivated by their significant Yukawa coupling to the Higgs Field that leads to their mass running lower for lower scales than the masses for the light squarks in models inspired by GMSB and MSUGRA [19]. Also, for solving the hierarchy problem, light top squarks are favourable since the remaining radiative correction to the Higgs boson mass in broken SUSY is also proportional to the Yukawa couplings. However, the focus on these scenarios leads to very restricted search regions, in particular due to the involvement of b-tagged jets in the final state. It is therefore important to search inclusively, also taking into account final states without b-jets. This “b-agnostic” strategy is sensitive to any kind of strongly produced sparticles, also those that decay without b quarks in the final state.

The analysis presented here is looking at final states with exactly one lepton<sup>1</sup> (electron or muon), multiple jets and missing transverse momentum ( $E_T^{\text{miss}}$ ). The requirement of one lepton suppresses the background originating from pure QCD (except  $t\bar{t}$  production) processes and the veto on additional leptons narrows down the irreducible SM backgrounds to processes producing exactly one leptonically decaying  $W$  boson.

### 3.2 Signal grids

The models described in section 1.3.4 were generated in 2-dimensional grids of the parameters. The one-step simplified models originally have three parameters. To capture the phenomenology in 2-dimensional grids, for each of the models one grid is generated where the ratio  $x = \frac{m(\tilde{\chi}_1^+) - m(\tilde{\chi}_1^0)}{m(\tilde{g}/\tilde{q}) - m(\tilde{\chi}_1^0)}$  is set to  $\frac{1}{2}$  and a second grid where the LSP ( $\tilde{\chi}_1^0$ ) mass is fixed

---

<sup>1</sup>If not specified otherwise the term *lepton* will be used equivalently as electron or muon (not including taus and neutrinos) throughout the next chapters

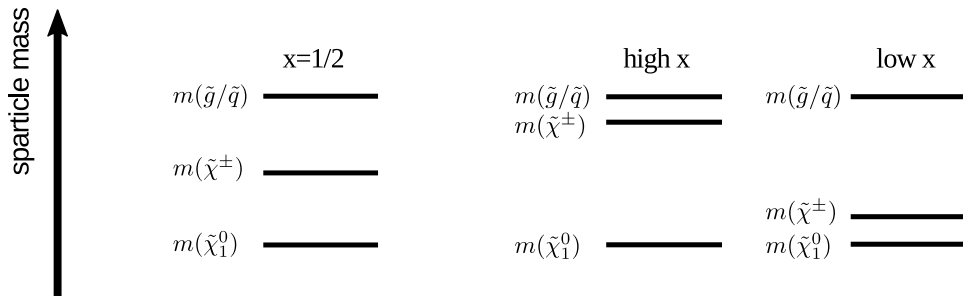


Figure 3.1: Different scenarios for the  $\tilde{g}\tilde{g}$  and  $\tilde{q}\tilde{q}$  one-step models. In the  $x = \frac{1}{2}$  grid, the mass spectrum is balanced. The decay energy in the first and second vertex is the same and depends only on the difference between the  $\tilde{g}$  and LSP ( $\tilde{\chi}_1^0$ ) mass. In the variable  $x$  grid, the LSP mass is fixed to 60 GeV, so high  $x$  and low  $x$  scenarios can be probed where the decay energies in the first and second vertex are different.

to 60 GeV and  $x$  is the second parameter. The second grid allows investigating “partially” compressed spectra where the mass difference for one of the decay vertices can be much smaller than for the other one (see Figure 3.1). For one scenario, the mass difference between the gluino/squark and the chargino is low (high  $x$ ), leading to soft jets from the first decay vertex, but a high  $p_T$  lepton from the second decay vertex in one of the decay branches. For low  $x$ , the mass difference between the chargino and the LSP is low, leading to hard jets from the first vertex, but a potentially softer lepton from the second vertex.

### 3.3 Backgrounds

The production of exactly one lepton, isolated from surrounding hadronic activity, in SM processes at proton-proton collisions typically involves a  $W$  boson that decays leptonically. Leptonic tau decays can also contribute. Neutrinos from these  $W$  boson decays will result in  $E_T^{\text{miss}}$ . QCD radiation can produce additional jets in the final state. Therefore, these backgrounds are partly irreducible. That means they share some indistinguishable phase space. The largest contribution comes from top quark pair production ( $t\bar{t}$ ) with one top quark decaying leptonically and the other one hadronically (“semi-leptonic”) and  $W$  boson production with additional jets ( $W$ +jets). Figure 3.2 shows example diagrams for these processes. Depending on the specific analysis selections, their contributions vary and different number of additional jets are relevant. Additional contributions are diboson and single top (dominantly  $Wt$ ) production. Top quark pair production with an additional vector boson ( $t\bar{t}+V$ ) is also considered. For  $Z$ +jets production, the only irreducible background is coming from the  $Z \rightarrow \tau\tau$  decay with one  $\tau$  decaying leptonically, since no  $\tau$  identification is performed and hadronically decaying taus are therefore identified as jets. Pure QCD multi-jet production, as well as all-hadronic  $t\bar{t}$  decays can only enter the selection via jets

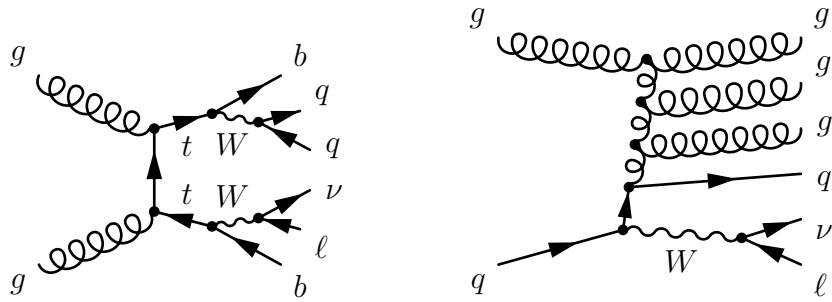


Figure 3.2: Example Feynman diagrams for  $t\bar{t}$  production and decay (left) and  $W$ +jets production. Both cases show a decay with exactly one lepton and multiple jets in the final state. The neutrino can lead to missing transverse energy.

that have been misidentified as a lepton and mis-measurement of  $E_T^{\text{miss}}$ . It has been shown that these backgrounds are negligible in all relevant selections of this analysis [57].

### 3.4 Simulated samples

The considered signal models and all relevant backgrounds have been simulated by using a variety of different Monte Carlo (MC) generators. Table 3.1 summarises all used samples and program versions. For further information, see the relevant ATLAS simulation notes [58–61].

The top quark pair processes, as well as the single top processes were generated by the POWHEG-BOX [62] generator. It implements the POWHEG [63] method for merging next-to-leading order (NLO) matrix elements with the parton shower process. For the parton shower, hadronisation and underlying event the POWHEG-BOX generator is interfaced with PYTHIA [64] with the PERUGIA2012 [65] tune and the CT10 PDF set [47].

$W/Z$ +jets and diboson processes are simulated using the SHERPA [66] program. It implements its own parton shower and is capable of merging leading order (LO) and NLO matrix elements with the parton shower, using the ME+PS@NLO prescription [67]. This has been used for the  $W/Z$ +jets samples to include up to two additional parton emissions at NLO and up to four at LO. The fully leptonic<sup>2</sup> diboson samples have been simulated with SHERPA v2.1 (no or one charged lepton) and v2.2 (at least two charged leptons). The semi leptonic diboson processes use v2.2. The v2.2 samples include up to one additional parton at NLO and the v2.1 samples no additional parton. In both cases, up to three additional partons are included at LO accuracy. For completeness, samples for electroweak diboson production with jets (e.g. vector boson scattering) and loop induced processes were also included. The v2.2 samples use the NNPDF3.0 PDF set [45] and the v2.1 samples CT10.

<sup>2</sup>here lepton stands for both charged lepton or neutrino

Physics process	Generator	Parton shower	Cross-section	PDF set	Tune
Signal	MADGRAPH5_AMC@NLO 2.2.2	PYTHIA 8.186	NLO+NLL [27–31]	NNPDF2.3 LO	ATLAS A14
$t\bar{t}$	POWHEG-BOX v2	PYTHIA 6.428	NNLO+NNLL [76]	CT10 NLO	PERUGIA2012
Single-top					
$t$ -channel	POWHEG-BOX v1	PYTHIA 6.428	NLO [77]	CT10f4 NLO	PERUGIA2012
$s$ -channel	POWHEG-BOX v2	PYTHIA 6.428	NLO [77]	CT10 NLO	PERUGIA2012
$Wt$ -channel	POWHEG-BOX v2	PYTHIA 6.428	NLO+NNLL [78]	CT10 NLO	PERUGIA2012
$W(\rightarrow \ell\nu) + \text{jets}$	SHERPA 2.2.1	SHERPA	NNLO [79]	NNPDF3.0 NNLO	SHERPA default
$Z/\gamma^*(\rightarrow \ell\ell) + \text{jets}$	SHERPA 2.2.1	SHERPA	NNLO [79]	NNPDF3.0 NNLO	SHERPA default
$WW, WZ$ and $ZZ$	SHERPA 2.1.1 / SHERPA 2.2.1	SHERPA	NLO	CT10 NLO / NNPDF3.0 NNLO	SHERPA default
$t\bar{t} + W/Z/WW$	MADGRAPH5_AMC@NLO 2.2.2	PYTHIA 8.186	NLO [80, 81]	NNPDF2.3 LO	ATLAS A14

Table 3.1: Summary of simulated signal and background event samples (Table adapted from [57]).

The  $t\bar{t}+W/Z$ , and also the signal samples were generated using MADGRAPH5\_AMC@NLO [68] at LO with up to two extra partons in the matrix element, merged with the parton shower using the CKKW-L [69] scheme. The  $t\bar{t}+WW$  process is simulated at LO accuracy without extra partons in the matrix element. For parton shower and hadronisation MADGRAPH5\_AMC@NLO is interfaced with PYTHIA8 [70], using the ATLAS A14 tune [71] and the NNPDF2.3 LO [72] PDF set.

The simulated events were mixed with simulated minimum bias samples, generated by PYTHIA8 with the A2 tune [73] with varying numbers of simultaneous soft QCD interactions to account for additional proton collisions in the same event (pileup). The detector simulation was performed with the full detector simulation based on GEANT4 [74] for the background samples and a fast detector simulation [75] based on parametrised detector responses for the signal samples.

The predicted number of events from an MC sample for a given integrated luminosity is given via the theoretical total cross section  $\sigma_{\text{tot}}$ . Table 3.1 lists accuracies to which the total the cross sections are calculated. For the main backgrounds, the  $t\bar{t}$ , single top and  $W$ +jets processes, the total cross sections are only needed for the development of the analysis strategy and the signal region optimisation. In the final statistical model, the total normalisation of these processes is taken from data.

Generated events can have weights. These can come from the generator itself, where especially NLO generators use weights in the combination of parton shower and matrix element. Another source of weighting events differently are filtered MC samples, that are generated by a priori selection criteria, to enhance the sample statistic in certain regions of phase space. The filter efficiency has to be taken into account when normalising the total event count. If multiple filters are combined, or filtered samples are combined with inclusive samples this leads to different event weights. Finally, some experimental corrections are applied by reweighting events, e.g to scale MC efficiencies to the ones measured in data. Therefore, instead of the total number of generated events, the sum of event weights  $w$  has

to be used,

$$N_{\text{pred}} = \frac{\int L dt \cdot \sigma_{\text{tot}}}{\sum_{i \in \text{generated}} w_i} \cdot \sum_{i \in \text{selected}} w_i$$

The MC statistical uncertainty on the predicted number of events resulting from the limited size of a set of selected MC events is given by the square root of the sum of squared weights,

$$\Delta N_{\text{pred}} = \sqrt{\sum_{i \in \text{selected}} w_i^2}.$$

## 3.5 Object definitions and event preselection

The event selection is based on several objects that are reconstructed from the detector data. Further *identification* criteria are applied to reduce backgrounds from misreconstructed objects. Electrons and muons are categorised into *baseline* and *signal* objects, distinguished by a loose and strict identification requirement. Prior to any further event selection, a common *preselection* is applied for all events considered.

### 3.5.1 Tracks, vertices and pile-up

The reconstruction of charged particle tracks starts with clusters created from raw data of the Pixel and SCT detectors. Each cluster corresponds to one space-point of a potential track. An iterative algorithm based on the Kalman filter technique [82] starts from seeds of three space-points to build track candidates. The tracks are assigned a score, based on which ambiguities are resolved [83]. Tracks in the loosest quality criterion are required to have a minimum  $p_T$  of 400 MeV [84]. Most objects that use tracks in their reconstruction require  $p_T > 500$  MeV.

The *impact parameters* are defined as the transverse ( $d_0$ ) and longitudinal ( $z_0$ ) distances of the closest approach of a reconstructed track to a reference point.

Vertices are reconstructed starting from the z-position at the beamline of reconstructed tracks as a seed. Nearby tracks are added by an iterative  $\chi^2$  fit. If a track is displaced by more than  $7\sigma$  from the vertex, it serves as a seed for a new vertex [85]. In the high luminosity environment at LHC, multiple inelastic collisions take place in one bunch crossing (in-time pile-up), reconstructed as several *primary vertices*. Objects that require an association to the primary vertex choose the one with the highest  $\sum p_T^2$ . The average of the mean number of interactions per bunch crossing  $\mu$  is denoted as  $\langle \mu \rangle$ . It is defined via the total inelastic proton cross section and the current luminosity [85]. The average number of reconstructed vertices  $N_{\text{Vtx}}$  is in general lower than  $\langle \mu \rangle$ , since not all interactions happen in the acceptance region of the detector and not all vertices are reconstructed. Furthermore, detector signals can be assigned to the wrong bunch crossing (out-of-time

pileup). This effect scales more with  $\langle\mu\rangle$  than with  $N_{\text{Vtx}}$ , since the inner detector has a short read-out window and a good timing resolution, so the vertex reconstruction is less affected by out-of-time pileup.

### 3.5.2 Jets

Jets are reconstructed from calorimeter cell clusters. A topological cell clustering algorithm [86] starts from seeds with significant energy deposits over noise level and successively merges neighbouring cells based on several thresholds. The energy entries are measured at the EM scale. This means they correspond to the deposits originating from electromagnetically interacting particles. No distinction between energy entries originating from hadronic or electromagnetic showers is made. The topological clusters are used as the input for the jet clustering with the anti- $k_t$  algorithm [87, 88] with a radius parameter  $R = 0.4$ . Tracks are assigned to the jets via the *ghost association* method, where they are set to infinitesimal momentum during the jet clustering [89]. The contribution of pile-up to the jet energy is subtracted per-event, per-jet, using jet areas [90]. The jet areas are also determined via ghost association with infinitesimal momentum particles added uniformly in solid angle to the event. Finally, the jets have to be calibrated to the jet energy scale (JES) by matching jets from MC simulation to reconstructed jets and correcting the EM scale energy to the particle level energy. For data, several *in-situ* corrections are applied, where differences between data and MC are evaluated in events where a jet is balanced by a well calibrated other object. A further calibration improves the jet resolution by taking the different energy response between quark and gluon initiated jets into account [89].

Jets with  $p_T < 50$  GeV and  $|\eta| < 2.4$  need to be associated to the primary vertex by the jet vertex tagger (JVT) [91], a multivariate discriminant based on quantities that describe the fraction of the total momentum of the jet that corresponds to tracks that are associated to the primary vertex. This suppresses jets originating from pile-up vertices. The imposed cut on this discriminant ( $> 0.4$ ) corresponds to an efficiency of 93% (96%) for jets originating from the hard interaction with  $20 \text{ GeV} < p_T < 30 \text{ GeV}$  ( $30 \text{ GeV} < p_T < 50 \text{ GeV}$ ). The jets used in this analysis require a minimum  $p_T$  of 20 GeV and  $|\eta| < 4.5$ . Further observables constructed from jets and all requirements on the jet multiplicity use central jets ( $|\eta| < 2.8$ ) with  $p_T > 30$  GeV.

### 3.5.3 B-tagging

Jets originating from b-quarks contain b-quark hadrons. Those have significant lifetimes and therefore their decays can be displaced from the primary vertex. For example, B mesons typically have lifetimes of  $c\tau \approx 450 \mu\text{m}$  [10]. For a particle with 50 GeV momentum (and a mass around 5 GeV), this corresponds to a mean flight path of  $\beta\gamma c\tau \approx 4.5$  mm.

The MV2 [92] algorithm combines the output of three different taggers into one classifier, based on Boosted Decision Trees (BDT). The first algorithm uses the impact parameters

of tracks in the jet. The second algorithm is a secondary vertex finder that tests track pairs inside a jet for a two-track vertex hypothesis. The third algorithm tries to reconstruct a full b-quark hadron decay chain with subsequent decays of the b-quark hadrons to c-quark hadrons.

B-tagged jets in this analysis are identified by the MV2c10 discriminant, with a cut on the score corresponding to 77% b-tagging efficiency.

### 3.5.4 Electrons

Electrons are reconstructed from tracks and calorimeter entries as described in [93]. Entries in the EM calorimeters are formed as clusters around seeds with a total cluster transverse energy above 2.5 GeV. The track reconstruction is complemented by an electron hypothesis (in contrast to the default pion hypothesis) for tracks with higher energy loss due to bremsstrahlung. The extrapolated tracks are matched to the calorimeter cluster barycentre using the distance in  $\eta$  and  $\phi$ . The cluster energy is calibrated to the electron energy scale from MC samples using multivariate techniques, also taking into account the amount of material in front of the cluster. The electron momentum direction is taken from the track information, while the energy corresponds to the final calibrated calorimeter cluster. Signal electron tracks are associated to the primary vertex of the hard collision by requiring  $d_0/\sigma_{d_0} < 5$  and  $\Delta z_0 \sin \theta < 0.5$  mm. The transverse impact parameter  $d_0$  and its estimated uncertainty  $\sigma_{d_0}$  is measured with respect to the beam line, while  $z_0$  is measured with respect to the chosen primary vertex. To discriminate against background electrons, several identification working points are defined [94]. Background electrons can for example originate from hadrons reconstructed as electrons and electrons from photon conversions (due to pair production in the tracker) or heavy flavour (b- or c-quark) hadron decays. The identification working points are based on a multivariate likelihood (LH) discriminant that is built from variables based on calorimeter shower shapes, proportions in the EM calorimeter and hadronic calorimeter, as well as track hits and measures for the transition radiation in the TRT. This analysis uses the *LH Loose* identification for baseline electrons and *LH tight* for signal electrons. Electrons are required a minimum  $p_T$  of 7 GeV and  $|\eta| < 2.47$ . The efficiencies for the electron identification depend on  $\eta$  and  $p_T$ . At 7 GeV the combined reconstruction and identification efficiency amounts to approximately 60%, increasing to over 85% at 60 GeV for the LH tight working point.

### 3.5.5 Muons

Muons are reconstructed both from their inner detector (ID) tracks and in the muon spectrometer (MS). This analysis uses combined muons, where after an independent track reconstruction in the MS and the ID, the global track is refit, using both the hits from the ID and MS. To extend the  $\eta$  range into the region  $2.5 < |\eta| < 2.7$ , extrapolated muons are added, where only the MS track is used. The track is extrapolated to the

inner detector to check the compatibility with originating from the interaction point. Both baseline and signal muons are required to fulfil the *medium* muon identification. The requirement is based on the number of hits in the MDT or CSC layers and a requirement on the compatibility between the ID and MS measurement, a cut on the significance of the difference in the charge to momentum ratio  $q/p$  measured in the MS and the ID. The combined efficiency of the reconstruction and medium identification is close to 99% in a large range of  $p_T$  and  $\eta$  [95]. Similar to the electrons, the muons are required to point back to the selected primary vertex by requiring  $d_0/\sigma_{d_0} < 3$  and  $\Delta z_0 \sin \theta < 0.5$  mm.

### 3.5.6 Lepton isolation

Both signal electrons and signal muons are required to be *isolated*. This means a region around the object is required to be clean of significant detector activity. The requirement is defined via a track based and calorimeter based variable. The track based isolation,  $p_T^{\text{varcone30}}$  is the sum of track momenta above 1 GeV in a cone around the lepton, excluding the lepton track. The cone size shrinks with increasing  $p_T$ ,  $\Delta R = \min(10 \text{ GeV}/p_T, 0.3)$ . The calorimeter based variable,  $E_T^{\text{topocone20}}$ , is defined by the sum of transverse energies in topological calorimeter clusters (see Section 3.5.2) in a cone of  $\Delta R = 0.2$  around the lepton, after subtracting the contribution from the lepton and correcting for pile-up effects. Cuts on the isolation variables are applied relative to the lepton momentum. Signal Leptons in this analysis require the *Gradient Loose* working point. It is defined by  $\eta$  and  $p_T$  dependent cuts on the isolation variables, such that the efficiency is 95% at 25 GeV and 99% at 60 GeV [94, 95].

### 3.5.7 Missing transverse momentum

Since the momentum of the colliding partons in a p-p collision is unknown, momentum conservation can only be assumed in the transverse plane. Therefore, the only indication for particles that do not interact with the detector is missing transverse momentum  $\mathbf{p}_T^{\text{miss}}$ . The magnitude is denoted as  $E_T^{\text{miss}}$ . It is constructed from the negative vector sum of the transverse components of all momentum vectors of reconstructed and calibrated objects and the track soft terms (TST). Those are all ID tracks associated to the chosen primary vertex fulfilling a basic quality selection, but not associated to any of the reconstructed and calibrated objects [96].

### 3.5.8 Overlap removal

After the baseline objects are reconstructed and identified an overlap removal procedure is carried out for close-by objects [97]. On the one hand this resolves ambiguities between objects that were reconstructed twice, for example electrons are typically as well clustered as jets. On the other hand the procedure serves as an additional isolation criterion, that

avoids two close by objects to bias each others energy and momentum resolution. Furthermore, backgrounds from leptons originating from meson or heavy flavour (b- or c-quark) hadron decays are suppressed by removing them under certain conditions when they overlap with a jet. The precise steps are as follows, where removed objects are no longer considered in the further steps

- If two electrons share an ID track, the one with the lower  $p_T$  is removed
- If an electron shares an ID track with a muon, remove the electron
- Reject (non-b-tagged) jets within  $\Delta R < 0.2$  of an electron.
- Reject electrons overlapping with a remaining jet. The cone size to define this overlap shrinks with increasing  $p_T$  of the electron,  $\Delta R = \min(0.4, 0.04 + 10 \text{ GeV}/p_T)$ . This avoids an increased rejection of leptons that are decay products of boosted particles, together with jets.
- Reject jets overlapping with muons within  $\Delta R < 0.2$  or where the muons were previously matched to the jet via ghost association. Only jets with less than 3 associated tracks with  $p_T > 500 \text{ MeV}$  or a low relative  $p_T$  of the jet and the sum of its tracks ( $p_T^\mu/p_T^{\text{jet}} > 0.5$  and  $p_T^\mu/\sum_{\text{jet tracks}} p_T^{\text{track}} > 0.7$ ) are removed. B-tagged jets are not considered for removal.
- Remove muons overlapping with a remaining jet. The same shrinking cone size as for the electron is used to define the overlap.

### 3.5.9 Event preselection

Prior to any further selection, events considered have to fulfil the following criteria:

- Reject data events where beam or detector conditions were not sufficient for physics analysis. This is also taken into account in the luminosity determination.
- Reject events where a jet was flagged as `BadLoose` [98]
- At least two jets with  $p_T > 30 \text{ GeV}$
- Exactly one signal lepton
- Veto events with further baseline leptons

### 3.6 Observables

To discriminate potential signals from the background, several observables are defined. Figure 3.3 shows a few distributions from MC simulation. All observables that use jets require a minimum  $p_T$  of 30 GeV.

- The *transverse mass* [99],

$$m_T = \sqrt{2p_T^\ell E_T^{\text{miss}} (1 - \cos[\Delta\phi(\mathbf{p}_T^\ell, \mathbf{p}_T^{\text{miss}})]),} \quad (3.1)$$

is one of the key pieces in the 1-lepton analysis. It is built from the missing transverse momentum ( $\mathbf{p}_T^{\text{miss}}$ ) and the lepton  $p_T$  ( $\mathbf{p}_T^\ell$ ) vectors. The calculation follows the definition of the invariant mass, but the transverse vectors are used. Since further leptons are vetoed in this analysis, real leptons from SM backgrounds originate from  $W$  boson decay. Therefore, in events where the neutrino from  $W$  boson decay is the only source of  $E_T^{\text{miss}}$  this variable has a kinematic endpoint at the  $W$  boson mass for the SM backgrounds. The signals considered in this analysis typically have a broadly distributed  $m_T$ . Backgrounds at  $m_T > 80$  GeV originate from the finite detector resolution and events with additional  $E_T^{\text{miss}}$ , e.g. with two leptonic  $W$  boson decays due to inefficiency of the second lepton veto or  $W \rightarrow \tau\nu$ . Other possibilities are off-shell  $W$  bosons and additional neutrinos from  $Z \rightarrow \nu\nu$  decays (e.g. in  $WZ$  events).

- The sum of the magnitudes of all transverse momenta of jets,  $H_T$ , is used in the definition of other observables
- The *effective mass*  $m_{\text{eff}}$ ,

$$m_{\text{eff}} = p_T^\ell + H_T + E_T^{\text{miss}}, \quad (3.2)$$

has a good correlation with the mass of the initially produced sparticles. More precisely, it scales with the mass difference of the squarks/gluinos and the LSP since it translates into the available momentum of the final state particles.

- The Aplanarity is defined as  $3/2 \times \lambda_3$ , the third eigenvalue of the sphericity tensor [100],

$$M_{xyz} = \sum_i \begin{pmatrix} p_{xi}^2 & p_{xi}p_{yi} & p_{xi}p_{zi} \\ p_{yi}p_{xi} & p_{yi}^2 & p_{yi}p_{zi} \\ p_{zi}p_{xi} & p_{zi}p_{yi} & p_{zi}^2 \end{pmatrix},$$

where the sum includes the lepton and jet momentum vectors. The eigenvalues are sorted and normalised to  $\lambda_1 + \lambda_2 + \lambda_3 = 1$ . The three eigenvectors (with the eigenvalues as magnitude) span an ellipsoid that characterises the main momentum directions in the event. A high value of the third eigenvalue corresponds to an event with spherically distributed momenta, while a low value indicates a planar decay. Many signal models are characterised by decays into multiple hard objects and have therefore a more spherical distribution of momenta than the background processes.

- The fraction  $E_T^{\text{miss}}/m_{\text{eff}}$  is useful for signals where  $m_{\text{eff}}$  is dominated by  $E_T^{\text{miss}}$ . This is the case for compressed models where  $E_T^{\text{miss}}$  is balanced by few ISR jets and the leptons are soft. The other scenario are high-x models where the decay energy is mainly distributed in  $E_T^{\text{miss}}$  and the lepton momentum and the jet momenta are soft.
- The  $E_T^{\text{miss}}$  significance  $E_T^{\text{miss}}/\sqrt{H_T}$  helps to suppress background with  $E_T^{\text{miss}}$  originating from finite detector resolution (“fake  $E_T^{\text{miss}}$ ”). This is useful in events with a large number of jets, where this effect is largest. The definition of this quantity is based on the assumption that the resolution of  $E_T^{\text{miss}}$  originates from the stochastic variation of the jet momentum measurement that scales approximately as  $1/\sqrt{p_T}$  [36].

### 3.7 Trigger

The data used in this analysis is recorded by using  $E_T^{\text{miss}}$  triggers. At the level one (L1) calorimeter trigger a threshold of  $E_T^{\text{miss}} > 50$  GeV is used. For different data taking periods in 2015 and 2016 different HLT thresholds were available, since the  $E_T^{\text{miss}}$  trigger rates depend on pile-up and therefore the thresholds had to be increased with higher instantaneous luminosity. The thresholds range from 70 GeV to 110 GeV. The HLT algorithm uses the jet-based algorithm (`mht`), which calculates  $E_T^{\text{miss}}$  by the vector sum of all jets reconstructed with the jet trigger algorithm. The jet trigger algorithm applies a correction for the energy contribution from pileup. Only calorimeter information is used, muons are not included in the trigger  $E_T^{\text{miss}}$  calculation [54]. To have the same trigger selection in MC as in data the MC events were assigned a random run number, distributed according to the luminosity in the different data runs. The corresponding triggers were then applied for the same run numbers as in data, corresponding to the data periods where the triggers were available. Figure 3.4 shows the efficiency of the combined trigger decision in data and MC. Above 200 GeV, the trigger selection is nearly fully efficient, both in data and MC. Therefore, no efficiency correction or uncertainty is needed for the trigger selection. All events considered in this analysis require  $E_T^{\text{miss}} > 200$  GeV.

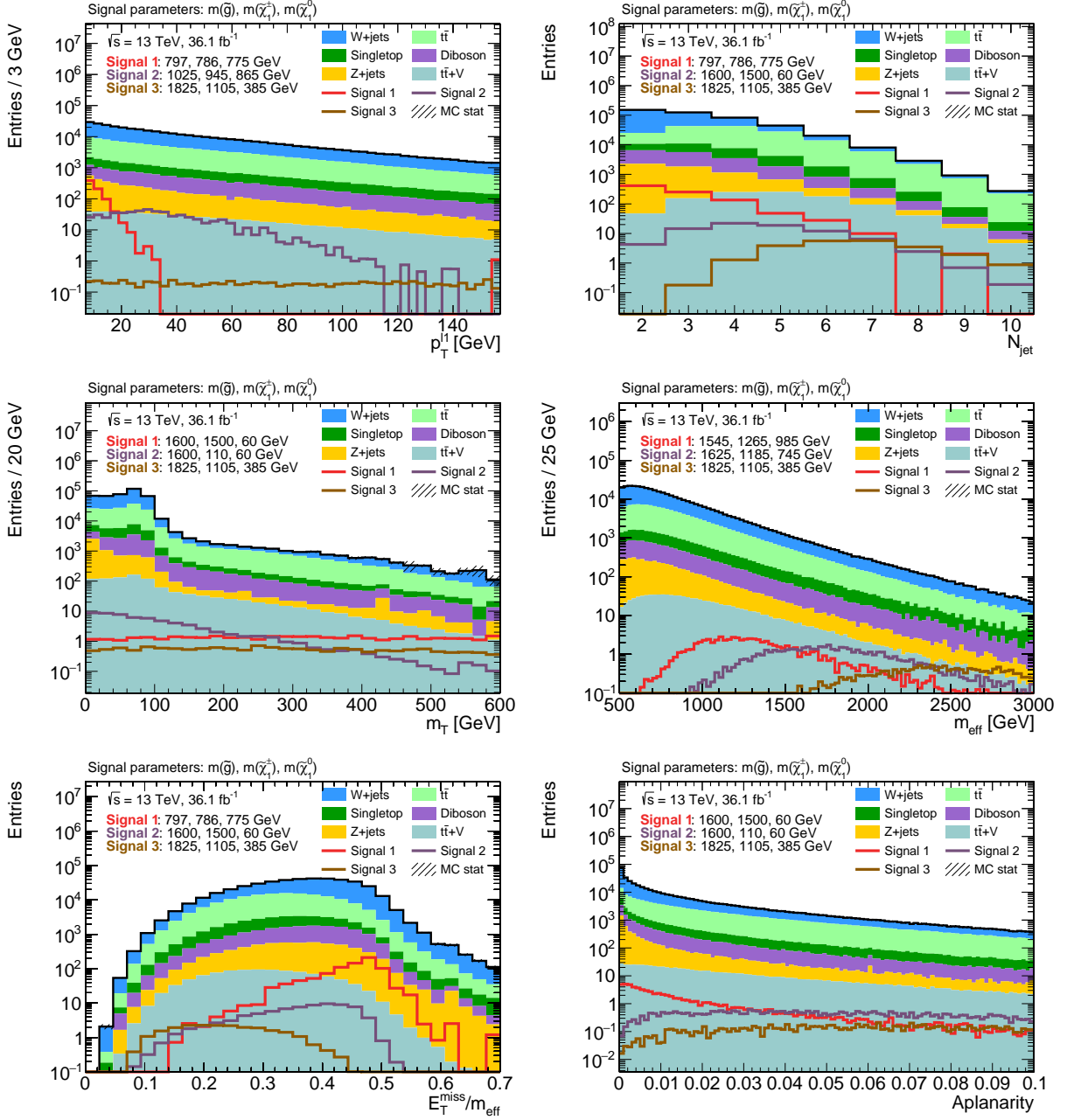


Figure 3.3: Distributions of several observables for simulated backgrounds and signal models overlaid. Different signal models are shown for the different observables to point out characteristic differences. The lepton  $p_T$  (top left) has lower values for more compressed mass spectra. Compressed spectra also yield a lower number of jets (top right), mostly from additional radiation, while high  $x$  models are characterised by a few high  $p_T$  jets and models with large mass differences between  $\tilde{g}/\tilde{q}$  and LSP ( $\tilde{\chi}_1^0$ ) have many jets in the event.  $m_T$  (middle left) has a broad distribution for many signals except for low  $x$  models, where a small mass difference in the second decay leads to softer leptons and less  $E_T^{miss}$ .  $m_{eff}$  (middle right) scales with the mass difference between  $\tilde{g}/\tilde{q}$  and the LSP. The ratio  $E_T^{miss}/m_{eff}$  (bottom left) can provide additional discrimination for high  $x$  and compressed models and the Aplanarity (bottom right) has a broad distribution for most signals, except for high  $x$  models that are characterised by few high  $p_T$  jets and a high  $p_T$  lepton.

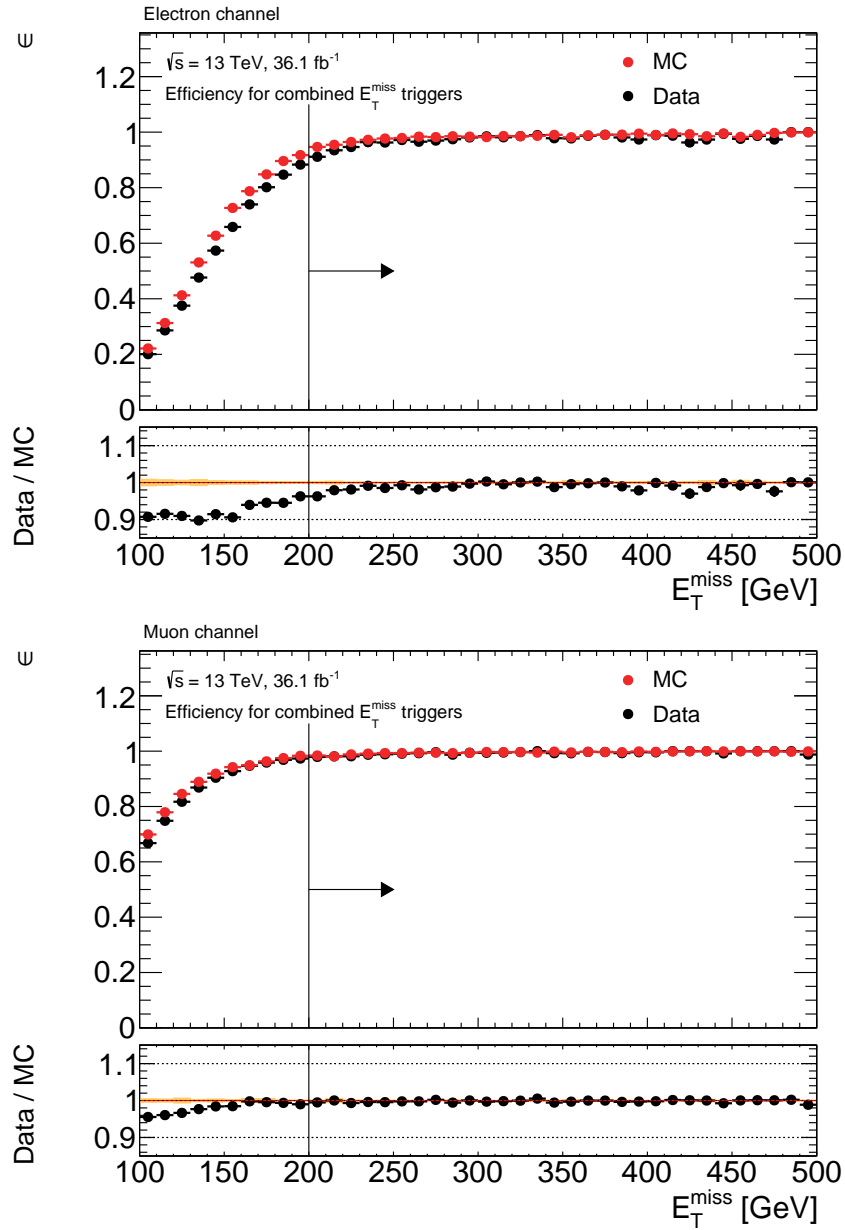


Figure 3.4: Efficiency for the combined  $E_T^{\text{miss}}$  triggers in Data and MC in events triggered by single lepton triggers in the electron (top) and muon (bottom) channel. A common selection of at least 4 jets and lepton  $p_T > 35$  GeV is applied. After the analysis preselection cut of  $E_T^{\text{miss}} > 200$  GeV the efficiencies for data and MC agree well and are close to 100%.



# Chapter 4

## Statistical data analysis

This chapter will briefly introduce the statistical concepts and methods that are used to optimise the analysis strategy, the treatment of uncertainties and the hypothesis tests that were used to derive the final results.

### 4.1 Test statistic and p-values

Searches at LHC are usually performed with the frequentist statistics philosophy [101, 102]. In frequentist statistics, probabilities describe the frequency of data, given a (known) model. This section follows Ref. [103] that contains the definitions and formulae that are used in this thesis.

In searches for new signals over a background, the compatibility of the data with a background model needs to be determined. To do so, one defines a *p-value*, the probability of measuring a certain outcome of an experiment, at least as extreme as the observed one, given a model where the signal is absent. On the other hand, when the experiments' outcome disfavours a signal, the absence of signal can also be tested by a p-value, based on a model where the signal is included.

The outcome of the experiment is quantified by a *test statistic*  $q$ , a function that combines the data observations into a single value. In the definitions used here, a more extreme outcome means higher values of the test statistic, so the p-value is defined by

$$p = \int_{q_{\text{obs}}}^{\infty} f(q|\text{model})dq, \quad (4.1)$$

where the distribution of the test statistic assuming a model,  $f(q|\text{model})$  has to be known or determined from pseudo experiments. For easier interpretation, the p-value is converted into a number of standard deviations from a Gaussian distribution, the *significance*,

$$Z = \Phi^{-1}(1 - p), \quad (4.2)$$

where  $\Phi^{-1}$  is the inverse of the cumulative distribution of a unit Gaussian. A discovery, based on rejecting a background hypothesis in particle physics is usually not claimed before observing a significance level of  $Z = 5$ ,  $Z = 3$  counts as *evidence*.

In the frequentist method, statistical models are assumed to be known, since they only make statements about the probability of data. Everything that is unspecified can only result from a data observation. The method used here describes unspecified models by unknown parameters that are determined from data by a likelihood fit. The *likelihood function* is constructed from probability density functions, given a model that depends on several parameters. The parameters that maximise the likelihood function  $L$  for given data are called maximum Likelihood (ML) estimators. The definitions of the statistic for tests based on such models at the LHC use the *profile likelihood ratio*,

$$\Lambda(\mu) = \frac{L(\mu, \hat{\boldsymbol{\theta}})}{L(\hat{\mu}, \hat{\boldsymbol{\theta}})}. \quad (4.3)$$

The parameter  $\mu$  is the value tested for the parameter of interest (POI). In a hypothesis test, that value corresponds to the hypothesis that shall be rejected, the *null hypothesis*. Usually there is an *expected* value of  $\mu$  in favour of which the null hypothesis shall be rejected, the *alternative hypothesis*. In this analysis the POI is the signal strength, a parameter scaling the total signal rate. The value  $\mu = 0$  corresponds to absent signal (background only),  $\mu = 1$  to the signal rate predicted by the model tested. For testing the discovery of a positive signal,  $\mu = 0$  corresponds to the null hypothesis,  $\mu = 1$  to the alternative hypothesis. The numerator of  $\Lambda(\mu)$  corresponds to the unconditionally maximised likelihood function, where  $\hat{\mu}$  is the ML estimator for the POI and  $\hat{\boldsymbol{\theta}}$  the ML estimators for the other parameters<sup>1</sup>, the *nuisance parameters*. The denominator is the conditionally maximised likelihood function with the POI fixed to  $\mu$ , where  $\hat{\boldsymbol{\theta}}$  are the nuisance parameters that maximise the likelihood function for this condition. Test statistics are build from the negative logarithm of  $\Lambda$ , which consequently has high values for observations in favour of the alternative hypothesis. For discovery of a (positive) signal, the test is only considered *one-sided*, so that fewer events than the expected number for the background only hypothesis are not counted as evidence against it. This leads to the definition of the test statistic  $q_0$ ,

$$q_0 = \begin{cases} -2 \ln \Lambda(0), & \hat{\mu} \geq 0 \\ 0, & \hat{\mu} < 0. \end{cases} \quad (4.4)$$

In the asymptotic (large sample size) limit, the distribution function  $f(q_0|\mu = 0)$  is a chi-squared distribution with one degree of freedom (scaled by  $\frac{1}{2}$ , since the rest of the values will correspond to a half delta distribution at 0, due to the requirement  $\hat{\mu} \geq 0$ ). From this, the discovery p-value,  $p_0$ , depends only on the value of the test statistic  $q_0$  and the significance is given by

$$Z_0 = \sqrt{q_0} \quad (4.5)$$

---

<sup>1</sup>the boldface symbols mean there can be an arbitrary number of parameters,  $\boldsymbol{\theta} = (\theta_1, \dots, \theta_N)$

If the background ( $\mu = 0$ ) hypothesis cannot be rejected and therefore no signal is discovered, the hypothesis can be swapped around to reject the signal+background ( $\mu = 1$ ) hypothesis. Also here, the test is done one-sided, meaning more events than the expected ones for the signal+background hypothesis are not considered as evidence against the signal. The test statistic for the *exclusion* of signals or deriving upper limits is therefore defined as

$$q_\mu = \begin{cases} -2 \ln \Lambda(\mu), & \hat{\mu} \leq \mu \\ 0, & \hat{\mu} > \mu. \end{cases} \quad (4.6)$$

Similar to  $q_0$ , the exclusion test statistic  $q_\mu$  is (for the null hypothesis  $\mu = 1$ ) asymptotically distributed like a half chi-squared distribution (and  $Z_\mu = \sqrt{q_\mu}$ ). A signal is considered excluded, when the p-value from  $q_{\mu,\text{obs}}$  is smaller than 0.05 ( $Z_\mu = 1.64$ ). For cases where  $\hat{\mu}$  would be negative, the denominator of the likelihood ratio is evaluated conditionally at  $\mu = 0$ . The test statistic has then a higher value than the one for the *Asimov data set*, the set of data that would correspond to the expectation values for the alternative hypothesis. For these values, the test statistic is distributed differently under the null hypothesis and the significance (for rejecting  $\mu = 1$ ) can be approximated by

$$Z_1 = \frac{q_1 + q_{1,A}}{2\sqrt{q_{1,A}}}, \quad (4.7)$$

where  $q_{1,A}$  is the value of the test statistic for the Asimov data set. To avoid excluding signals due to under-fluctuating events in cases when the exclusion power is low, the exclusion p-value  $p_{s+b}$  is divided by the p-value  $p_b$ , which is derived from the distribution of the test statistic under the background only hypothesis ( $\mu = 0$ , still using the exclusion test statistic  $q_\mu$ ) [104]. This results in the quantity

$$CL_s = \frac{p_{s+b}}{p_b}. \quad (4.8)$$

Exclusion limits in this work are always derived by requiring  $CL_s < 0.05$ . In addition to the observed p-values or  $CL_s$  values, the expected ones, corresponding to the median of the test statistic under the alternative hypothesis (or approximately the Asimov data set), are also quoted. From the quantiles of the test statistic distribution under the alternative hypothesis, a  $\pm 1\sigma$  band on the expected p-values can be derived. It shows in which range the determined p-value is expected to fluctuate for repeated observations distributed according to the alternative hypothesis. In the asymptotic limit, the band is simply given by varying the significance values with  $\pm 1$ .

## 4.2 Building the Likelihood

All statistical models in this thesis are based on binned Likelihood fits. Each bin is described by a Poisson distribution, where the distribution function for the number  $N$  of

observed events with the expected number  $\lambda$  is given by

$$P(N|\lambda) = \frac{\lambda^N e^{-\lambda}}{N!}. \quad (4.9)$$

Therefore, the total Likelihood is the product over the Poisson distributions for each bin. This requires statistically independent bins, ensured by appropriate selection criteria. The expected number of events,  $\lambda$ , in a bin is in general a function of the POI  $\mu_{\text{sig}}$  and the nuisance parameters. Nuisance parameters that are directly constrained by the Poisson terms for the data observations are called *normalisation factors*  $\boldsymbol{\mu}_{\text{bkg}}$ . The other nuisance parameters describe the systematic uncertainty parameters  $\boldsymbol{\alpha}$ . Each of them is constrained by an *auxiliary measurement*, described by a unit Gaussian distribution

$$G(x|\alpha) = \frac{1}{\sqrt{2\pi}} e^{-\frac{1}{2}(x-\alpha)^2}. \quad (4.10)$$

The auxiliary data  $x$  is set to 0. It does not correspond to real data, but is treated in the same way. The total likelihood function is schematically

$$L(\mu_{\text{sig}}, \boldsymbol{\mu}_{\text{bkg}}, \boldsymbol{\alpha}) = \prod_{i \in \text{bins}} P(N_i | \lambda_i(\mu_{\text{sig}}, \boldsymbol{\mu}_{\text{bkg}}, \boldsymbol{\alpha})) \prod_{j \in \text{sys}} G(0 | \alpha_j) \quad (4.11)$$

where the expected values  $\lambda_i$  (predicted event counts) are functions of the expected signal events  $\boldsymbol{s}$ , background events  $\boldsymbol{b}$ , nuisance parameters  $\boldsymbol{\mu}_{\text{bkg}}, \boldsymbol{\alpha}$  and the POI  $\mu_{\text{sig}}$ .

Although the systematic variations are a priori independent, correlations between the parameters (both systematics and normalisation factors) can arise since the predicted event count in a single bin can be affected by multiple parameters and a single parameter can affect the predicted event count in multiple bins.

The systematic uncertainty parameters are given as fixed variations (*up* and *down*) and need to be interpolated and extrapolated to map the value of each systematic parameter continuously onto its impact in each bin, for signal and all background processes. The up and down variations are interpolated by a polynomial and extrapolated by an exponential function. This combination ensures positive values for the predicted event counts for all values of the systematic parameters and avoids discontinuous derivatives (*kinks*) around  $\alpha_j = 0$ . The uncertainty on the limited MC sample size is summed up for each bin and described by one nuisance parameter per bin with a Poisson constraint term. The HistFactory package [105] is used for creating the statistical models and provides the interpolation functions. The input histograms and configuration for HistFactory are generated by HistFitter [106].

### 4.3 Estimating sensitivity

When designing the strategy for a search it is useful to have a measure to optimise for. The signal regions presented here have been optimised for maximum expected discovery

significance. Since the complete statistical model depends on many aspects that are usually developed after the search regions have been chosen, a set of assumptions has to be made when calculating the expected significance. For a setup, where only the total number of events after a certain selection is counted (*cut and count*), the sensitivity is dominated by three numbers: the total number of background events  $b$ , the total number of expected signal events  $s$  and the uncertainty on the predicted mean value of the background  $\Delta b$ . This can be modelled by a setup with two event counts (two *bins*) where one bin is the region enriched with the signal, the signal region (SR), and the other one, being signal free, a control region (CR) measurement of the background. If the ratio of the predicted yield/rate in the SR and CR is known, the *transfer factor*  $\frac{N_{\text{SR}}}{N_{\text{CR}}}$ , then the total predicted background in the SR can be a fit parameter. The limited statistics in the CR then effectively translates into an uncertainty on the total expected background in the SR. The likelihood is defined as

$$L(\mu_{\text{sig}}, b) = P(N_{\text{SR}}|\mu_{\text{sig}}s + b) \cdot P(N_{\text{CR}}|\tau b). \quad (4.12)$$

The known constant  $\tau$  is the inverse of the transfer factor. With the effective uncertainty on the measurement of  $b$ , coming from the Poisson uncertainty  $\sqrt{\tau b}$  in the CR, the factor  $\tau$  can be approximated in terms of the total uncertainty  $\Delta b$  on the background,

$$\tau = \frac{b}{\Delta b^2}. \quad (4.13)$$

To get a simple estimate of the expected significance, one approach is to rewrite the two Poisson distributions as a Poisson distribution of the total number of events in SR+CR and a binomial distribution, describing the probability of picking  $N_{\text{SR}}$  events out of  $N_{\text{tot}}$  with a fixed probability  $\rho$  that is known since the transfer factor is known,

$$L(\mu_{\text{sig}}, b) = \underbrace{\frac{e^{-\lambda_{\text{tot}}} \lambda_{\text{tot}}^{N_{\text{tot}}}}{N_{\text{tot}}!}}_{P(N_{\text{tot}}|\lambda_{\text{tot}})} \cdot \underbrace{\binom{N_{\text{tot}}}{N_{\text{SR}}} \rho^{N_{\text{SR}}} (1-\rho)^{N_{\text{tot}}-N_{\text{SR}}}}_{B(N_{\text{SR}}|\rho, N_{\text{tot}})}. \quad (4.14)$$

From this, the p-value for rejecting the background only hypothesis can be defined by the probability sum for picking at least  $N_{\text{SR}}$  events out of  $N_{\text{tot}}$  with probability  $\rho$ ,

$$p_{\text{B}} = \sum_{j=N_{\text{SR}}}^{N_{\text{tot}}} B(j|\rho, N_{\text{tot}}) \quad (4.15)$$

This can be calculated in a numerically fast way, also for large numbers and non-integer values of  $N_{\text{tot}}$  and  $N_{\text{SR}}$ , using the incomplete beta function<sup>2</sup> [107]. To get the expected p-value, one simply needs to insert  $N_{\text{tot}} = \tau b + s + b$ ,  $\rho = \frac{1}{1+\tau}$  and  $N_{\text{SR}} = s + b$ . The optimisation studies in the next chapter make use of this method, referred to as binomial Significance  $Z_{\text{B}}$ .

<sup>2</sup>This is implemented in the `RooStats::NumberCountingUtils` methods in ROOT



# Chapter 5

## Signal region optimisation

The discovery of rare signals requires distinctive selection procedures, since the cross sections of background processes are many orders of magnitude higher than the potential signals. The signal regions were optimised to discover (in the sense of seeing significant deviations) as many of the considered models as possible.

### 5.1 Methods

All optimisation methods share the common approach of maximising a measure of expected discovery significance by tuning certain analysis selection cuts. One method corresponds to an  $N$ -dimensional scan over all possible combinations of discrete cut values for  $N$  observables. The second method is based on one-dimensional scans, which can be performed iteratively, by scanning one observable while applying all selections except for the cut on the scanned observable ( $N-1$  plots).

#### 5.1.1 $N$ -dimensional scan

This approach is meant to find the best combination of cuts on a certain number of observables, which are potentially correlated. For each possible combination of selection criteria, the number of expected background events, their statistical error from the limited MC sample size and the number of signal events is determined from the MC samples. This requires the careful definition of a finite number of discrete steps  $k$  per observable, also taking into account that the number of combinations increases quickly when adding further steps or further observables ( $N_{\text{combinations}} = \prod_i k_i$ ). In practise, it has turned out to be feasible to scan several million combinations, although good results could often be achieved with much less.

Prior to evaluating the significance measure for each combination, for different fixed values of signal efficiency, candidates can be selected to maximise the background rejection.

This creates a Receiver Operation Characteristic (ROC) curve, which is per definition independent of the absolute normalisation, as it only depends on the efficiencies. These candidates are expected to also give maximum significance. For significance definitions that increase monotonically with the expected number of signal events and decrease monotonically with the expected number of background events this is generally true. This is not necessarily always the case since uncertainties can increase when the background decreases with tighter selection criteria, e.g due to the decreased statistics of the MC sample. In practise, the decrease of sensitivity due to this effect is usually smaller than the increase due to lower number of background events. Figure 5.1 shows an example where the assumption is validated for the binomial significance, taking into account the uncertainty from the MC sample size. With the assumption that the optimal candidates lie on the ROC curve it is also possible to use more computationally intense evaluations of the significance, e.g. checking the impact of systematic uncertainties for each selection candidate separately, since it is sufficient to scan a certain number of points on the ROC curve instead of all possible combinations.

Another approach is to directly solve the  $N$ -dimensional minimisation problem. Since this sort of problem typically has many local minima, standard minimiser programs do not lead to satisfactory results and empirical approaches like Simulated Annealing or Genetic Algorithms have to be used. Both are implemented in the Toolkit for Multivariate Data Analysis (TMVA), which is part of the ROOT data analysis framework [108, 109]. However, in the context of this analysis, similar performance to the “brute-force” approach of scanning all combinations in a predefined set of steps could only be achieved with much longer computing time (see Figure 5.2 for a comparison).

### 5.1.2 N-1 plots

A more supervised, less automated way is directly looking at one-dimensional scans, each observable at a time. It is useful to plot the distribution for different background components, as well as different potential signal models in addition to the expected significance that could be achieved by cutting on each value on the x-axis. This way one can get more direct feedback on which observables are the most relevant ones, if significance maxima only result from statistical fluctuations and how the ideal selections would differ for different signal models. The approach can also be combined with the  $N$ -dimensional scan. After having found an ideal cut combination, the one dimensional projections of the scan can validate and potentially improve the selection that was determined by the  $N$ -dimensional scan. Since the one-dimensional scans can be done iteratively, the method leads to similar results as the  $N$ -dimensional scans, even with correlated variables.

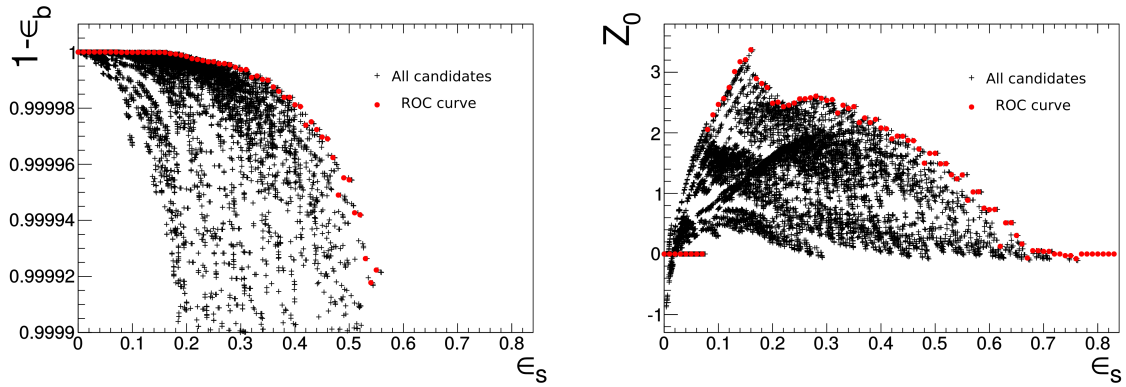


Figure 5.1: Signal efficiency versus background rejection (left) and signal efficiency versus expected Significance (right) for all selection candidates in an  $N$ -dimensional scan. The candidates marked in red are selected to maximise the background rejection for a given signal efficiency (ROC curve). For candidates where all simulated background events were rejected, no Significance can be defined, therefore the Significance is set to 0. The binomial significance definition is used, taking into account the statistical uncertainty on the MC sample size.

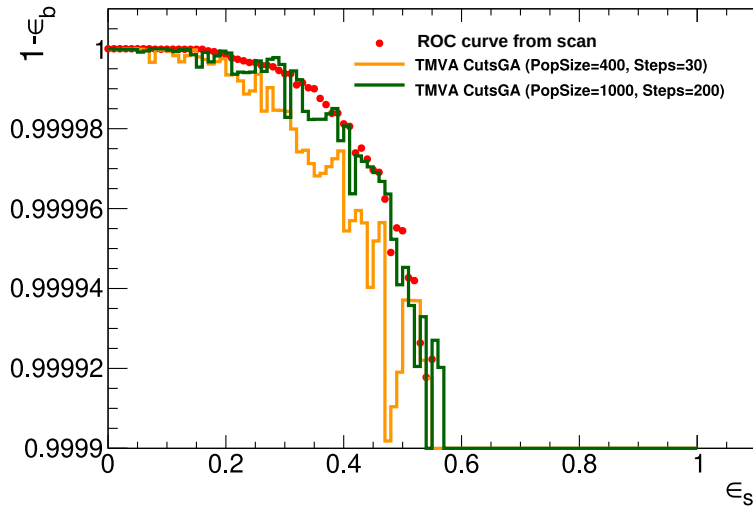


Figure 5.2: ROC curve for an example of an  $N$ -dimensional scan, in comparison to solving the same problem by the TMVA cut optimisation method, using the Genetic Algorithm for fitting. To reach similar performance as scanning 25000 cut combinations (the red points), the TMVA parameters had to be tuned (green line). The orange line corresponds to the default parameters. The computation time for the setup represented by the green curve was around 2.5 h, compared to around 15 s for the scanning of 25000 combinations.

## 5.2 Optimisation for the analysis with $3.2 \text{ fb}^{-1}$

At the beginning of 2015 the LHC started Run-2, the first time with a centre of mass energy of 13 TeV. Since this is around twice the energy from the first run (2010 and 2012 with 7 and 8 TeV) a boost in sensitivity for particles with higher, previously unreachable masses was expected, even with a small amount of data. To analyse the data of the first year of Run-2 as fast as possible, the search strategy for the 1-lepton analysis [110] was to work with several selections that are evaluated separately. For each selection, the hypothesis testing is done by using a single signal enriched bin (*cut and count*). Four reference gluino one-step models were selected, close to the parameter space that was excluded by the ATLAS Run-1 analysis [111].

These four reference models contain decays into high  $p_T$  (*hard*) leptons, so a cut on  $p_T^\ell > 35 \text{ GeV}$  was required as preselection. Table 5.1 shows the observables and scan steps that were used for the  $N$ -dimensional scan. The scan was performed separately for a requirement of at least 4, 5 and 6 jets. The significance was evaluated using the Binomial significance formula (see section 4.3) with the assumption of a constant relative uncertainty on the predicted background yield of 25%, in addition to the uncertainty from the limited MC sample size. The total yields were normalised to an expected integrated luminosity of  $3 \text{ fb}^{-1}$ . The sensitivity calculation was cross-checked by a full fit to Asimov data (see Section 4.1) in a setup similar to the one that was planned to be used to derive the final result, taking into account experimental uncertainties. The statistical model included a preliminary control region (the selection was based on a first look at the 13 TeV data [112]) with the following definition:

- At least 5 jets
- $p_T^{j1,2,3,4,5} > (150, 100, 40, 40, 40) \text{ GeV}$
- $E_T^{\text{miss}} > 200 \text{ GeV}$
- $40 \text{ GeV} < m_T < 120 \text{ GeV}$
- $800 \text{ GeV} < m_{\text{eff}} < 1200 \text{ GeV}$

The region was then split into two bins, one requiring at least one b-tagged jet and the other one requiring no b-tagged jet, to simultaneously normalise the contributions from top and  $W$ +jets backgrounds. Figure 5.3 shows an example for an optimisation scan. The position of the maximum is roughly equivalent for the simplified evaluation using the Binomial Significance formula and the full fit setup. The most extreme combinations of cuts correspond to regions where the MC statistics is not sufficient to give an accurate description of the predicted background yield. To avoid selecting these scenarios, a requirement of at least 10 simulated (unweighted) background events for each of the two main backgrounds,  $t\bar{t}$  production and  $W$ +jets was introduced for the candidates considered. Overall,

Observable	Cut values
$p_{\text{T}}^{j1}$	$> \in \{30, 75, 125, 175, 225, 275, 325, 375\} \text{ GeV}$
$p_{\text{T}}^{jN}$	$> \in \{30, 50, 70, 90, 110, 130, 150\} \text{ GeV}$
$E_{\text{T}}^{\text{miss}}$	$> \in \{150, 200, 250, 300, 350, 400, 450\} \text{ GeV}$
$m_{\text{T}}$	$> \in \{75, 125, 175, 225, 275, 325, 375, 425\} \text{ GeV}$
$m_{\text{eff}}$	$> \in \{0, 200, 400, \dots, 5800\} \text{ GeV}$
$E_{\text{T}}^{\text{miss}}/m_{\text{eff}}$	$> \in \{0, 0.1, 0.2, 0.3\}$
Aplanarity	$> \in \{0, 0.01, 0.02, \dots, 0.1\}$

Table 5.1: Observables and cut values for the N-dimensional optimisation scan performed to optimise the hard lepton signal regions for the  $3.2 \text{ fb}^{-1}$  analysis [110]. The scan was performed separately for a minimum number of  $N = 4, 5$  and 6 jets. The jets are sorted by  $p_{\text{T}}$ , so a  $p_{\text{T}}$  requirement on the N-th jet means all jets up to the N-th have to fulfil this requirement.

the sensitivity did not turn out to be limited by this requirement. The grey line in the plots corresponds to candidates without this requirement.

Finally, all resulting signal region candidate selections were adjusted with  $N-1$  plots, where in some cases the criteria were loosened to achieve a more reliable description of the background, while keeping the sensitivity at a comparable level. An example for  $N-1$  plots after the finally chosen selection is given in Figure 5.4.

Table 5.2 lists the reference signal points and the final signal region selections for the hard lepton scenarios. The different selection criteria can be understood from the different decay topologies (see Figure 3.1). The lower jet multiplicity for high  $x$  and low  $x$  signal regions originates from softer jets in one of the two decay vertices. For high  $x$ , the first decay gives less energy to the jets, for low  $x$ , the second one. Since the first decay vertex gives always jets, in the low  $x$  scenario, 4 jets with a rather high  $p_{\text{T}}$  are expected. This results on a strict requirement of the  $p_{\text{T}}$  on all 4 jets, while in the high  $x$  scenario only the first jet is required to have a very high  $p_{\text{T}}$ . Furthermore, the high  $x$  events are more planar, since the decay energy is spread into fewer objects. Therefore, the Aplanarity has low discrimination power and hence no requirement is applied for the scenario optimised for high  $x$ . Another difference between high and low  $x$  scenarios is the different requirement on  $m_{\text{T}}$ . In high  $x$  scenarios, both the lepton and the LSP receive high boosts, leading to a broadly distributed  $m_{\text{T}}$  shape up to very high values, while for low  $x$  most of the decay energy goes into the jets, leading to less  $m_{\text{T}}$ . The 5-jet and 6-jet signal region without regard of the slightly different jet multiplicity<sup>1</sup> are mainly distinguished by the different

<sup>1</sup>The 5-jet signal region is the result of an optimisation for a model where one would actually expect more hard jets than the one the 6-jet signal region was optimised for. However, this is balanced by the stricter requirement on the  $p_{\text{T}}$  of the subleading jets.

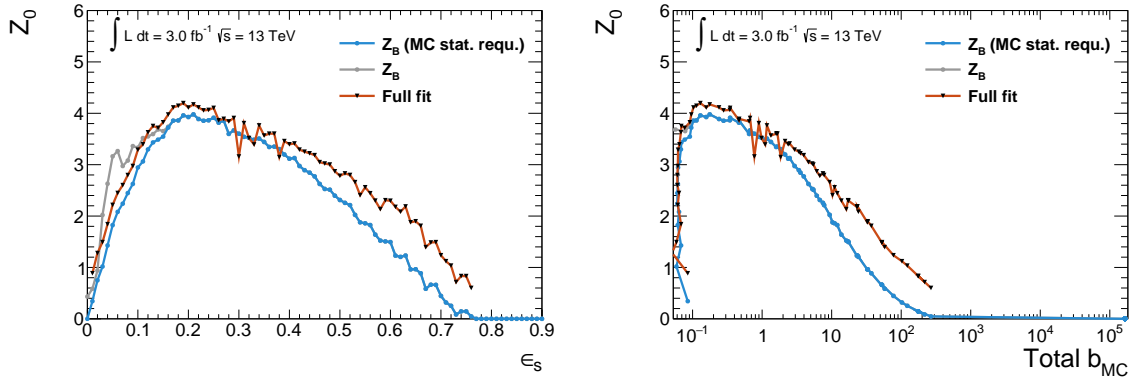


Figure 5.3: Significance scan for the selection candidates on the ROC curve for the gluino one-step model with  $m(\tilde{g}, \tilde{\chi}_1^\pm, \tilde{\chi}_1^0) = 1385, 705, 25$  GeV. All selection candidates require at least 5 jets. The left plot shows the expected significance plotted against the signal efficiency of the corresponding selection, the right plot against the total expected number of background events.

$m_{\text{eff}}$  cuts, as they were optimised for models with different mass differences between the gluino and the LSP in the  $x = 1/2$  grid. High  $x$  models can profit from a cut on the ratio of  $E_T^{\text{miss}}$  and  $m_{\text{eff}}$  since a large fraction of the decay energy goes into the boost of the LSP.

A dedicated set of selections target the more compressed spectra with  $p_T < 35$  GeV (*soft leptons*), where typically hard initial state radiation (ISR) jets have to be present, that recoil against the LSPs to produce significant  $E_T^{\text{miss}}$  [110].

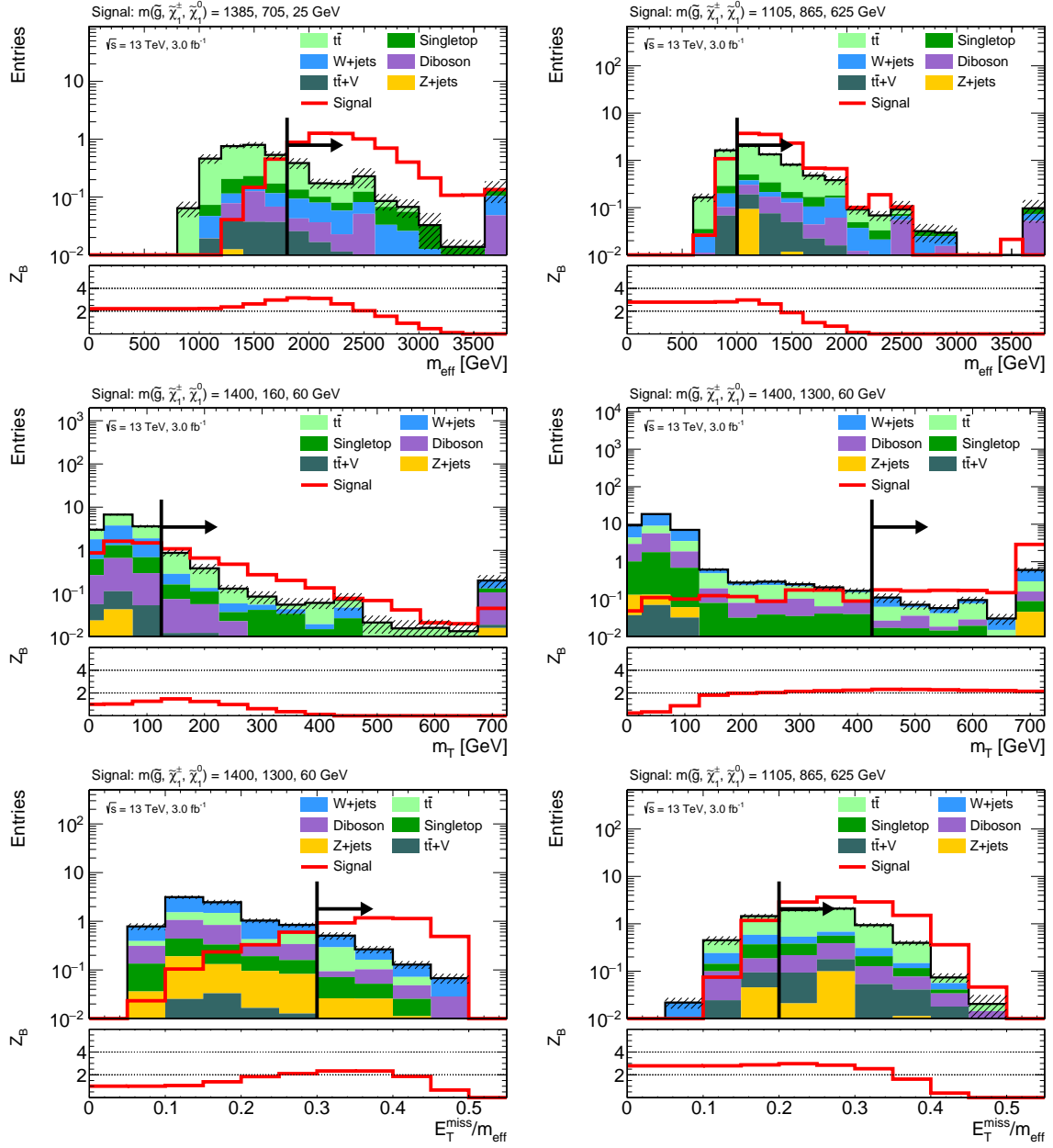


Figure 5.4: One-dimensional significance scans for  $m_{\text{eff}}$  for a high gluino mass (top left), a lower gluino mass point (top right),  $m_T$  for a low  $x$  point (middle left) and a high  $x$  point (middle right) and  $E_T^{\text{miss}}/m_{\text{eff}}$  for a high  $x$  point (bottom left) and a medium gluino mass point with  $x = 1/2$  (bottom right). All selections for the signal regions corresponding to the reference signal models (see Table 5.2) have been applied, except the one on the plotted quantity (cut value indicated by the black line). The bottom pad of each plot shows the significance that would be achieved when cutting on the corresponding value on the x-axis.

	4-jet high- $x$ SR	4-jet low- $x$ SR	5-jet SR	6-jet SR
Reference $m(\tilde{g}, \tilde{\chi}_1^\pm, \tilde{\chi}_1^0)$ (GeV)	1400, 1300, 60	1400, 160, 60	1385, 705, 25	1105, 865, 625
$N_{\text{jet}}$	$\geq 4$	$\geq 4$	$\geq 5$	$\geq 6$
$p_{\text{T}}^{\text{jet}}$ (GeV)	$> 325, 30, \dots, 30$	$> 325, 150, \dots, 150$	$> 225, 50, \dots, 50$	$> 125, 30, \dots, 30$
$E_{\text{T}}^{\text{miss}}$ (GeV)	$> 200$	$> 200$	$> 250$	$> 250$
$m_{\text{T}}$ (GeV)	$> 425$	$> 125$	$> 275$	$> 225$
$E_{\text{T}}^{\text{miss}}/m_{\text{eff}}$	$> 0.3$	-	$> 0.1$	$> 0.2$
$m_{\text{eff}}$ (GeV)	$> 1800$	$> 2000$	$> 1800$	$> 1000$
Aplanarity	-	$> 0.04$	$> 0.04$	$> 0.04$

Table 5.2: Resulting hard lepton signal regions from the optimisation procedure for the  $3.2 \text{ fb}^{-1}$  analysis and reference signal models that were used for optimisation. A cut on  $p_{\text{T}}^{\ell} > 35 \text{ GeV}$  is applied for all regions as well. The table was adapted from [110].

### 5.3 Concept for the analysis with $36.1 \text{ fb}^{-1}$

The concept of optimising based on several reference signal models and defining one cut and count signal region for each of them was repeated with 2015 and partial 2016 data of in total  $14.8 \text{ fb}^{-1}$  [113]. In addition to the gluino models, the squark models were also considered, leading to even more different signal region definitions. To generalise the setup, the analysis of the full 2015 and 2016 data with  $36.1 \text{ fb}^{-1}$  [57] was performed with a multi-bin fit. The idea is to keep the optimal sensitivity for the considered signal models, while staying general by using all available information simultaneously.

The key observable to perform the shape fit is the effective mass  $m_{\text{eff}}$ . A combined likelihood function (see Equation 4.11) is created from multiple bins according to several ranges of  $m_{\text{eff}}$ . Due to different shapes for different squark/gluino to LSP mass differences (see Figure 5.5), a shape fit can provide optimal sensitivity for the different scenarios. The optimisation for the shape fit scenario was based on the previous structure of having a signal region at higher jet multiplicities for the highest mass signals, two signal regions around 4 jets, targeting the low- $x$  and high- $x$  scenarios, and a soft lepton signal region starting at lower jet multiplicities (2 jets), targeting compressed scenarios, potentially with hard ISR jets. The shape fit setup allows to have a common set of selections targeting both the gluino and the squark scenarios.

All bins are orthogonal. The **2J** signal region has an upper cut on the lepton  $p_{\text{T}}$ , the **4J** signal regions are orthogonal by their  $m_{\text{T}}$  requirements, and they have an upper cut of at most 5 jets. Finally, the **6J** signal region requires at least 6 jets. In addition to the  $m_{\text{eff}}$  binning, each bin is further split into a category requiring at least one and no b-tagged jet. This provides the best sensitivity for the simplified models without b-quarks in the final state, while keeping the generality of the search, potentially discovering more

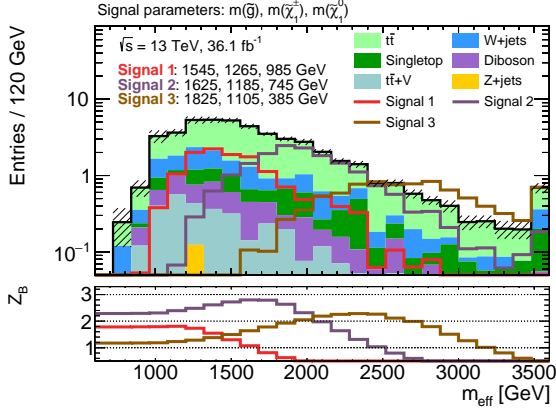


Figure 5.5: Significance scan in  $m_{\text{eff}}$  for different gluino one-step signal models with different mass differences between the gluino and the LSP. The selection for the **6J** signal region of the  $36.1 \text{ fb}^{-1}$  analysis has been applied for illustration. The signals would prefer different cuts on  $m_{\text{eff}}$ . Therefore, this observable is used to perform a binned shape fit.

realistic scenarios where b-quarks might be present (e.g. gluino decays to top quarks). The optimisation of the remaining cuts has been performed with a significance estimate that uses the squared sum of significances in all  $m_{\text{eff}}$  bins.

$$Z_B^{\text{total}} = \sqrt{\sum_{\text{bins}, i} (Z_B^i)^2}, \quad (5.1)$$

where the binomial significance estimate was used to evaluate the significance per bin. A constant 30% uncertainty on the background prediction was assumed. Furthermore, the resulting selections were validated in a simplified fit setup, also assuming 30% constant background uncertainty. A coarse scan over different cut combinations was then performed to maximise the expected exclusion contour across the different signal grids [114]. Table 5.3 lists the final selection criteria. The generic features of these selections are very similar to the ones found for the  $3.2 \text{ fb}^{-1}$  analysis.

A simpler cut and count setup was re-derived from the shape fit setup by choosing the  $m_{\text{eff}}$  bin for each signal region, that yields the largest area of sensitivity in the different signal model grids when the low edge of the bin is used as an  $m_{\text{eff}}$  cut. The purpose of this simpler setup is the possibility for a more model independent hypothesis testing. No assumption on the predicted signal rates has to be made to evaluate a potential excess in one of these regions and in the absence of an excess, upper limits on the number of additional events in these regions can be derived. Those upper limits can be interpreted in any signal model, when the efficiency of the signal region selection is known. The cut and count regions are labelled *discovery* signal regions (disc) in the table, while the shape fit setup is labelled *exclusion* (excl). Despite their names, both setups can be used for testing either the signal+background, as well as the background only hypothesis.

SR	2J	4J high-x	4J low-x	6J
$N_\ell$	= 1	= 1	= 1	= 1
$p_T^\ell$ [GeV]	> 7(6) for $e(\mu)$ and < $\min(5 \cdot N_{\text{jet}}, 35)$	> 35	> 35	> 35
$N_{\text{jet}}$	$\geq 2$	4-5	4-5	$\geq 6$
$E_T^{\text{miss}}$ [GeV]	> 430	> 300	> 250	> 350
$m_T$ [GeV]	> 100	> 450	150-450	> 175
Aplanarity	–	> 0.01	> 0.05	> 0.06
$E_T^{\text{miss}}/m_{\text{eff}}$	> 0.25	> 0.25	–	–
$N_{b\text{-jet}}$ (excl)		= 0 for $b$ -veto, $\geq 1$ for $b$ -tag		
$m_{\text{eff}}$ [GeV] (excl)	3 bins $\in$ [700,1900] + [ $> 1900$ ]	2 bins $\in$ [1000,2000] + [ $> 2000$ ]	2 bins $\in$ [1300,2000] + [ $> 2000$ ]	3 bins $\in$ [700,2300] + [ $> 2300$ ]
$m_{\text{eff}}$ [GeV] (disc)	> 1100	> 1500	> 1650(1300) for gluino (squark)	> 2300(1233) for gluino (squark)

Table 5.3: Overview of the selection criteria for the **2-6J** signal regions, used for gluino/squark one-step models in the  $36.1 \text{ fb}^{-1}$  analysis. The table is taken from [57].

## 5.4 Optimisation for the multijet channel

SUSY particles might decay via longer chains, or in general with a higher number of objects in the final state. The two-step and pMSSM models (see Section 1.3.4) provide a benchmark for such scenarios.

This opens the possibility for a different approach—to focus the signal region selection on the jet multiplicity. Analyses of this kind have been performed at ATLAS for the 0-lepton channel [36] and in the 1-lepton channel specifically for scenarios where no  $E_T^{\text{miss}}$  is present, e.g. certain R-parity violating processes with decays of the LSP into only visible particles [115]. As part of this thesis, a multijet search in 1-lepton events, still using  $E_T^{\text{miss}}$  and  $m_T$  has been performed to complement the already existing approaches. In the effort of finding a good signal region, as a first step an N-dimensional scan (see Section 5.1.1) was done for each signal point of the pMSSM and two-step grids separately, assuming an integrated luminosity of  $30 \text{ fb}^{-1}$ . As seen in Figure 5.6, a requirement of at least 9 jets was a common optimum for many signal models. Therefore, it was decided to use a 9-jet signal region for this search. When looking at the performance of a few signal regions, defined based on the scan in each point, similar performance could be reached with 3 signal regions, that differ only by their  $m_{\text{eff}}$  cut (see Figure 5.7). Therefore, this selection is used as the **9J** signal region, together with a binned shape fit in  $m_{\text{eff}}$ . It is defined as follows:

- Exactly one lepton with  $p_T > 35 \text{ GeV}$
- At least 9 jets
- $E_T^{\text{miss}} > 200 \text{ GeV}$

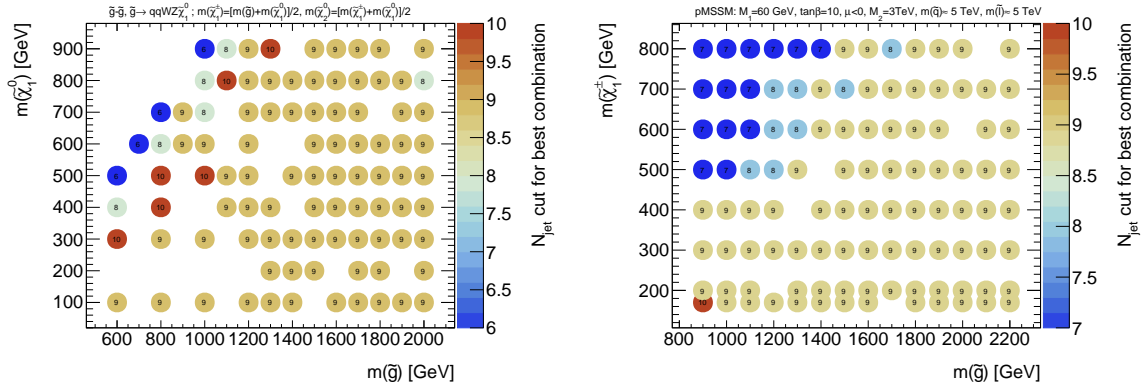


Figure 5.6: Cut values for the minimum jet requirement for the best cut combinations, determined in an N-dimensional optimisation scan for each signal model in the multijet benchmark grids. The left plot shows the results for the two-step grid, the right plot the pMSSM models. A requirement of at least 9 jets is the common optimum for many signal points. See Appendix A.1 for the cut values on the other observables.

- $E_T^{\text{miss}} / \sqrt{H_T} > 8 \text{ GeV}^{1/2}$
- $A_{\text{planarity}} > 0.07$
- $m_T > 175 \text{ GeV}$

The discovery setup for model independent hypothesis tests was chosen to apply a cut of  $m_{\text{eff}} > 1500 \text{ GeV}$ . Figure 5.8 shows the N-1 plots. The binning for the shape fit will be discussed later.

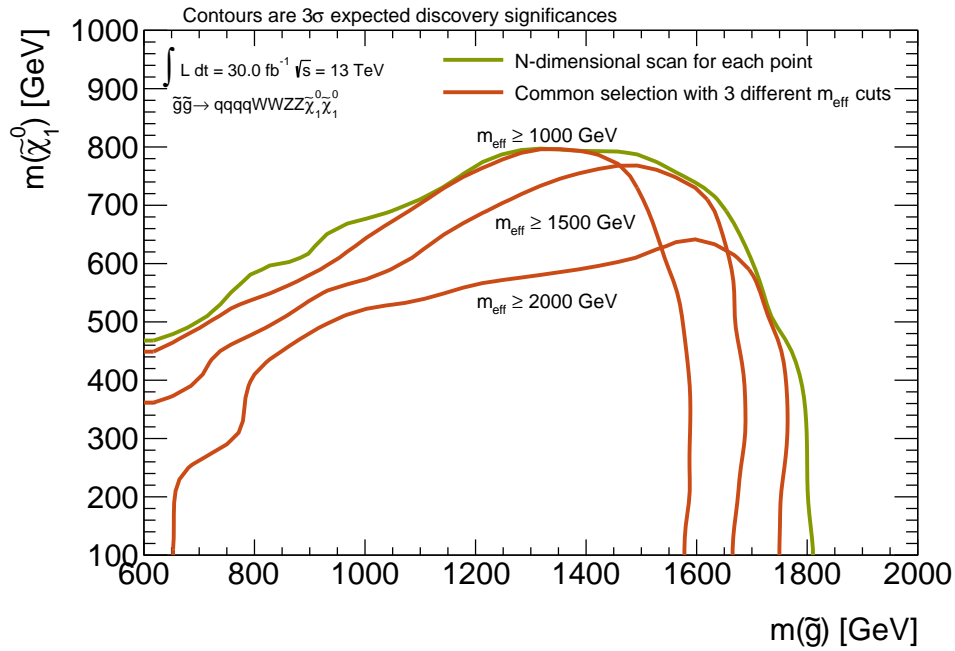


Figure 5.7: Sensitivity estimation for multijet signal region candidates in the two-step grid. The green contour shows the result from an N-dimensional scan over cut combinations for each signal point. The orange lines show an option for a signal region candidate with a common selection, but 3 different  $m_{\text{eff}}$  cuts, yielding similar sensitivity. This was the motivation for a single signal region, binned in  $m_{\text{eff}}$ . The contours correspond to the expected discovery significance at a  $3\sigma$  level.

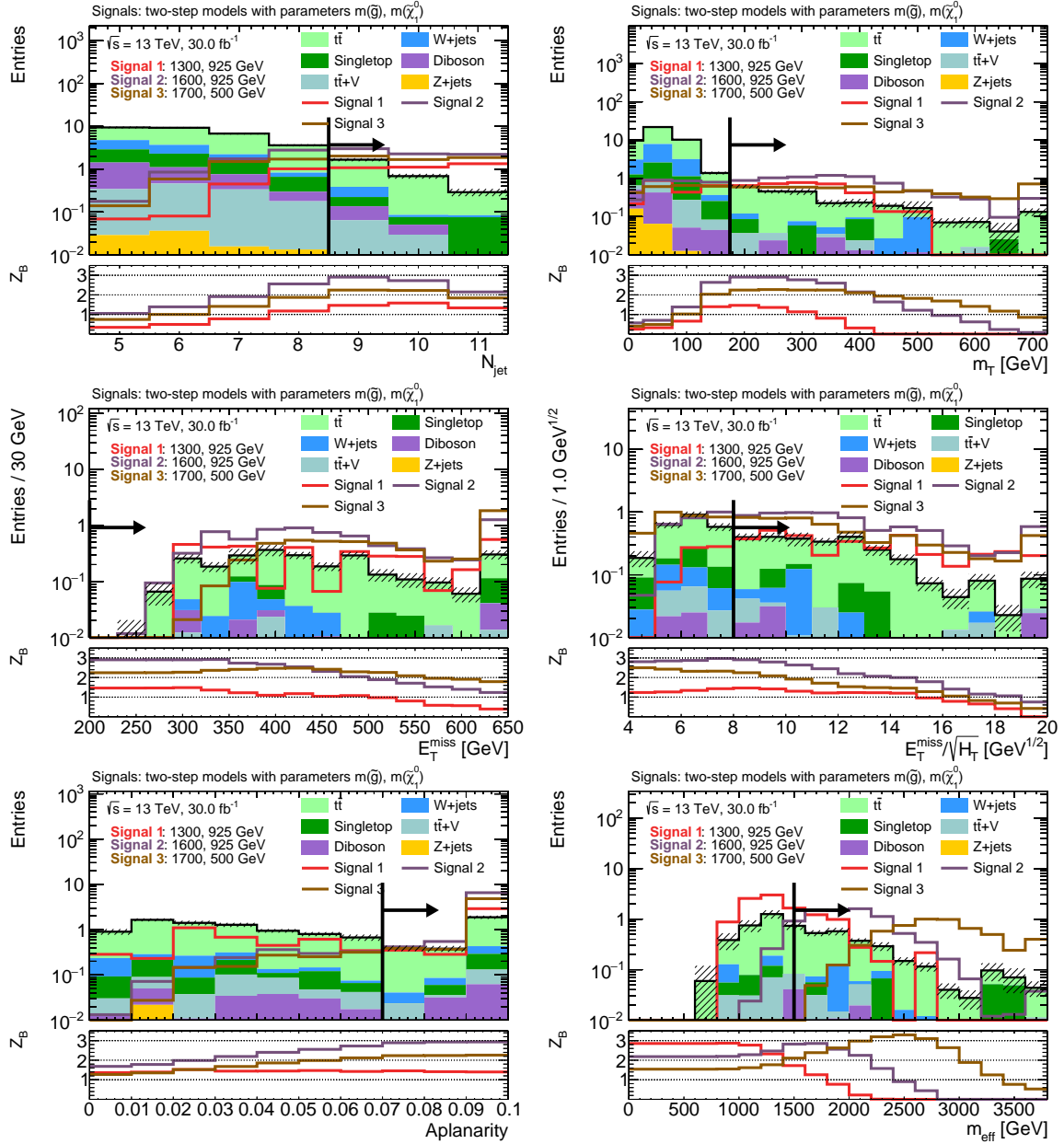


Figure 5.8: N-1 plots for the multijet discovery signal region. The significance scan for three signal points from the two-step grid are shown as a reference.



# Chapter 6

## Background estimation

The estimation of backgrounds only from MC simulation is often problematic. Uncertainties on the theoretical prediction are in many cases not statistically rigorous, e.g. varying parameters by arbitrary factors or comparing different methods/programs for the simulation. Furthermore, the extreme phase space regions for searches for new physics often show mismodelling that is not covered by the uncertainties on the simulated prediction. It is desirable to constrain background predictions as much as possible from data, leaving uncertainties of statistical nature which have a more clear interpretation.

### 6.1 The transfer factor approach

The simplest way of constraining background predictions from data is the *transfer factor* approach. Here, the ratio of events in a signal and control region  $\frac{N_{\text{SR}}}{N_{\text{CR}}}$  is the only prediction taken from simulation. The control regions are designed to be approximately free of signal. This was briefly discussed in section 4.3 for a simple setup where no further uncertainties were assumed. In this approach, the total background in the control region can be determined from data. If the control region has much more data events than the signal region the uncertainty on the total background prediction solely depends on the number of observed data events in the control region. In practice, the transfer factor is not known exactly. Instead, the impact of uncertainties is evaluated on the transfer factor. The final setup uses the equivalent description where not the total background is fitted to data, but a normalisation factor  $\mu_b$ . The expected number of events in the signal and control region ( $b_{\text{SR}}, b_{\text{CR}}$ ) are normalised to the cross section and luminosity and the background

prediction in the signal and control regions is given by

$$\begin{array}{ll}
 \textit{Transfer factor} & \textit{Normalisation factor} \\
 N_{\text{bkg,SR,pred}} = b_{\text{fit,CR}} \times \frac{b_{\text{SR}}}{b_{\text{CR}}} & = \mu_{b,\text{fit}} \times b_{\text{SR}} \quad (6.1)
 \end{array}$$

$$\begin{array}{ll}
 N_{\text{bkg,CR,pred}} = b_{\text{fit,CR}} \times 1 & = \mu_{b,\text{fit}} \times b_{\text{CR}} \quad (6.2)
 \end{array}$$

As seen in Equations 6.1 and 6.2, the transfer factor approach is equivalent to the normalisation factor approach since one approach can be related to the other by scaling the free fit parameter by a constant factor,

$$\mu_{b,\text{fit}} = \frac{1}{b_{\text{CR}}} \times b_{\text{fit,CR}}. \quad (6.3)$$

In more complex setups multiple backgrounds can be constrained simultaneously and contributions from backgrounds without normalisation factors are added. To have a sufficiently determined minimisation problem, at least the same number bins/measurements as the number of fit parameters are needed. Technically, the transfer factor approach is implemented in the HistFitter [106] package. The  $\pm 1\sigma$  variations on the background predictions are normalised to leave the predicted sum of event counts in all control regions unchanged. This procedure does not introduce additional assumptions. Effectively it removes correlations between the normalisation factors and the systematic parameters beforehand.

## 6.2 Blind analysis

By knowing the data beforehand while designing an analysis strategy there is the danger of unintentionally tuning the result in a particular direction. To avoid this *experimenters bias*, blinding [116] techniques are used. In searches for new signals the data in the signal regions are usually kept hidden until the complete analysis strategy is decided. The analyses described in this thesis start with optimisation of signal region selections using simulated data. Next, control regions are designed and checked for potential signal contamination. The statistical analysis is divided in a *background-only fit*, performed in the control regions with zero signal contamination assumed and the *model-dependent signal fit*, performed in the signal and control regions where the predicted signal contamination is taken into account in all regions. The fitted parameters of the background-only fit are applied (and the uncertainties propagated) to *validation regions* that do not participate in the fit. Those are defined to be closer to the signal regions and validate the extrapolations. In a typical scenario control regions are defined by selection criteria that differ in two observables from the signal regions. Validation regions can then be defined by inverting only one of the two requirements, to validate the extrapolation of the fit parameters in the other one. Another

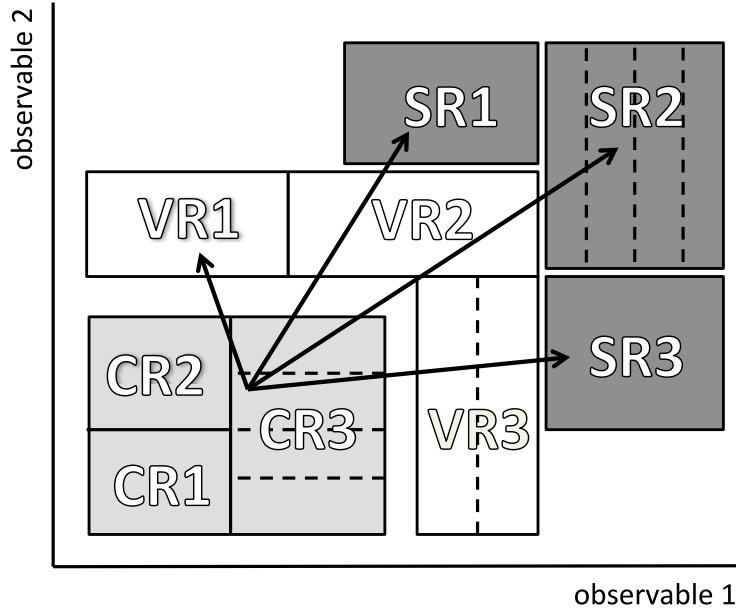


Figure 6.1: Schematic view of a possible configuration with control, validation and signal regions (CR, VR, SR). The validation regions are used to check the extrapolations of fit parameters into the signal regions (Figure from [106])

possibility is to place a validation region at intermediate values for an observable, while the control region is at low and the signal region at high values (see Figure 6.1). Once the extrapolation assumptions are validated, the signal region data is looked at and a potential excess of data is quantified or exclusion limits on absent signals are evaluated. The HistFitter package provides the functionality for all these steps.

### 6.3 Convention for data/MC comparison plots

Throughout this chapter, several plots show simulated SM processes compared to data. They are derived by an approximation instead of the full statistical procedure. The level of compatibility shown should reflect what is relevant in terms of the statistical treatment that is used for the final results. The convention is as follows:

- The contributions of the main backgrounds,  $t\bar{t}$  and  $W$ +jets are normalised to simultaneously fit the total number of data events in the category with at least one b-tagged jet and a veto on b-tagged jets by solving the system of equations

$$\begin{aligned}
 N_{\text{Data},b\text{-tag}} &= \mu_W \cdot b_{W,b\text{-tag}} + \mu_{\text{Top}} \cdot b_{\text{Top},b\text{-tag}} + b_{\text{other},b\text{-tag}} \\
 N_{\text{Data},b\text{-veto}} &= \mu_W \cdot b_{W,b\text{-veto}} + \mu_{\text{Top}} \cdot b_{\text{Top},b\text{-veto}} + b_{\text{other},b\text{-veto}}
 \end{aligned}$$

for the normalisation factors  $\mu_W$  and  $\mu_{\text{Top}}$ , where  $b_{W/\text{Top}/\text{other},b\text{-tag}/b\text{-veto}}$  are the predicted background yields in the b-tagged and b-veto categories from MC, normalised to cross section, for the  $W$ +jets,  $t\bar{t}$  and other (remaining) contributions.

- The uncertainty bands on the simulated processes include the uncertainty due to the limited MC sample size and the experimental uncertainties. For the latter, the single variations are normalised to the same integral as the nominal prediction for the  $t\bar{t}$  and  $W$ +jets processes, so the variation only affects the shape of the distributions. For the other processes, both normalisation and shape uncertainties are included. Each variation is correlated across all processes and bins and the total uncertainty band corresponds to the sum in quadrature.
- The uncertainty bars on the data points correspond to the 68% central confidence interval, assuming the data is drawn from a Poisson distribution.

## 6.4 Background estimation for the 2-6-jet channels

As discussed in Section 5.3 the Analysis in the 2-6-jet signal regions is designed for a binned likelihood fit in the effective mass  $m_{\text{eff}}$ . The tails of several  $p_T$  spectra show substantially different shapes for data and MC simulation. This translates into a mismodelling of the  $m_{\text{eff}}$  shape that is not covered by systematic uncertainties (see Figure 6.2). For the  $t\bar{t}$  background the origin of the mismodelling has been studied extensively [114]. One attempt included reweighting the top  $p_T$  distribution to the predicted shapes calculated at next-to-next-to-leading-order (NNLO) [117]. Another approach was reweighting a reconstructed top  $p_T$  and other distributions to data in a loose selection. Different simulation programs showed a similar mismodelling. None of the approaches showed a clear indication on where the mismodelling originates from. Also, the reweighting attempts did not show a consistent improvement in all observables.

To get a reliable description of the background, the statistical model for the 2-6-jet signal regions has to constrain the  $m_{\text{eff}}$  shape from data. This is done by fitting one normalisation factor for each bin in  $m_{\text{eff}}$ , for each signal region. The control regions have the same  $m_{\text{eff}}$  bin boundaries as the signal regions. The fit effectively performs a bin wise reweighting of the  $m_{\text{eff}}$  distributions to match the data in the control regions.

Table 6.1 shows the detailed definitions for the selection criteria of all control and validation regions. The control region selection criteria are widely consistent with the corresponding signal regions except for two well modelled observables. One of the two observables is the transverse mass  $m_T$ , while the other one is the Aplanarity for the **4J-lowx/highx** and the **6J** signal region and  $E_T^{\text{miss}}$  for the **2J** signal region. The top and  $W$ +jets background components are normalised simultaneously. For each bin there is one top and one  $W$ +jets normalisation factor. Both signal and control regions are split into a category requiring no (*b-veto*) and at least one (*b-tag*) b-tagged jet. The b-tagged category is enriched in the

top background while the b-veto category has a large contribution from  $W$ +jets. The top processes include  $t\bar{t}$  and single top (dominated by  $Wt$ ) production. Validation regions are defined to include the same  $m_{\text{eff}}$  bins, to validate the extrapolation for each bin.

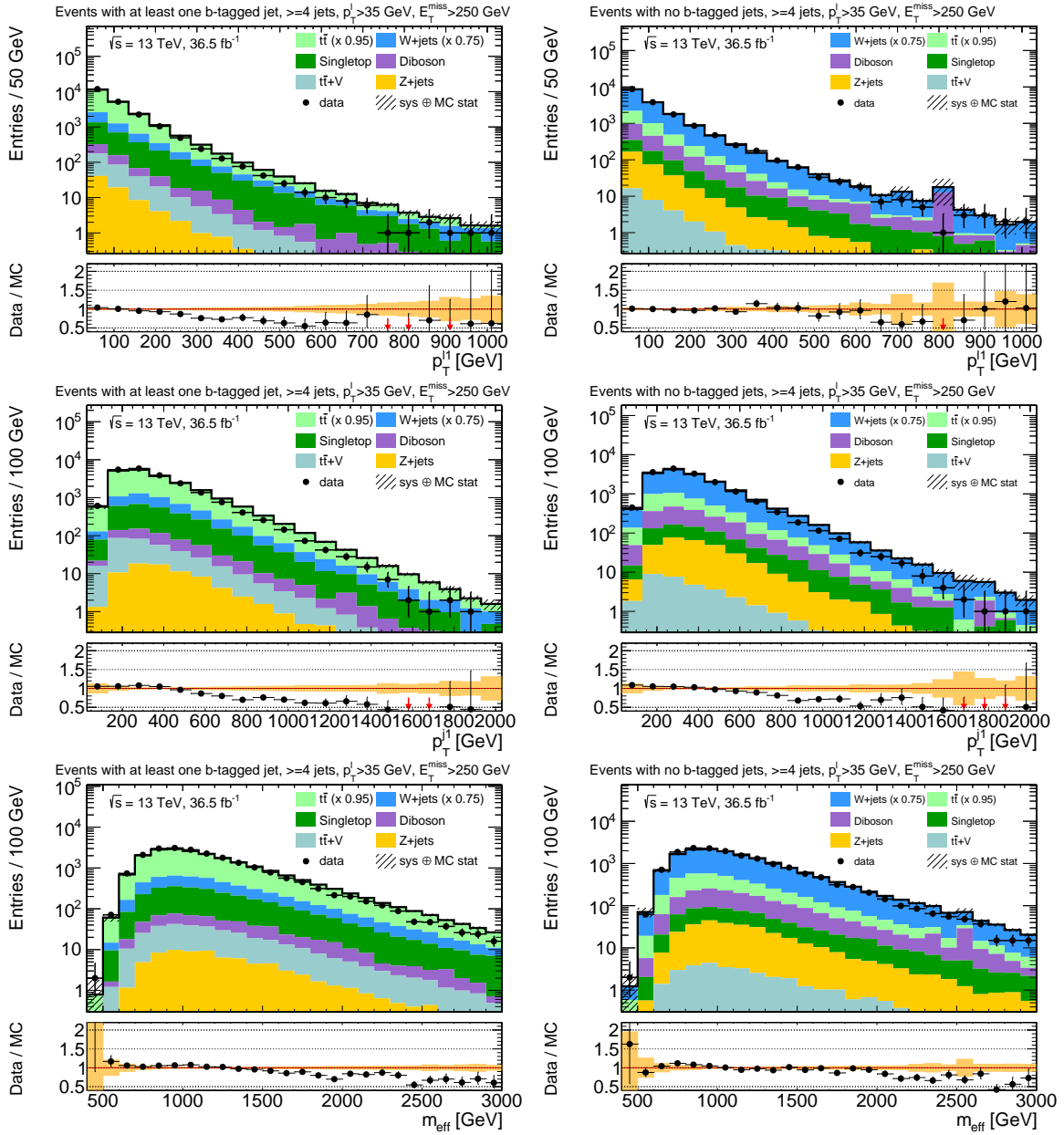


Figure 6.2: Mismodellings in the tails of several  $p_T$  spectra. The left column shows events with at least one b-tagged jet, the right column with a veto on b-tagged jets. Too many events are predicted at high values of the lepton  $p_T$ , mainly for the  $t\bar{t}$  background (first row). The jet  $p_T$  spectrum (the  $p_T$  of the leading jet is shown in the second row) shows a similar trend, both for the  $W$ +jets and the  $t\bar{t}$  simulation. This leads to a mismodelling in the  $m_{\text{eff}}$  shape (third row). A common selection of at least 4 jets,  $p_T^\ell > 35$  GeV and  $E_T^{\text{miss}} > 250$  GeV is applied for all plots.

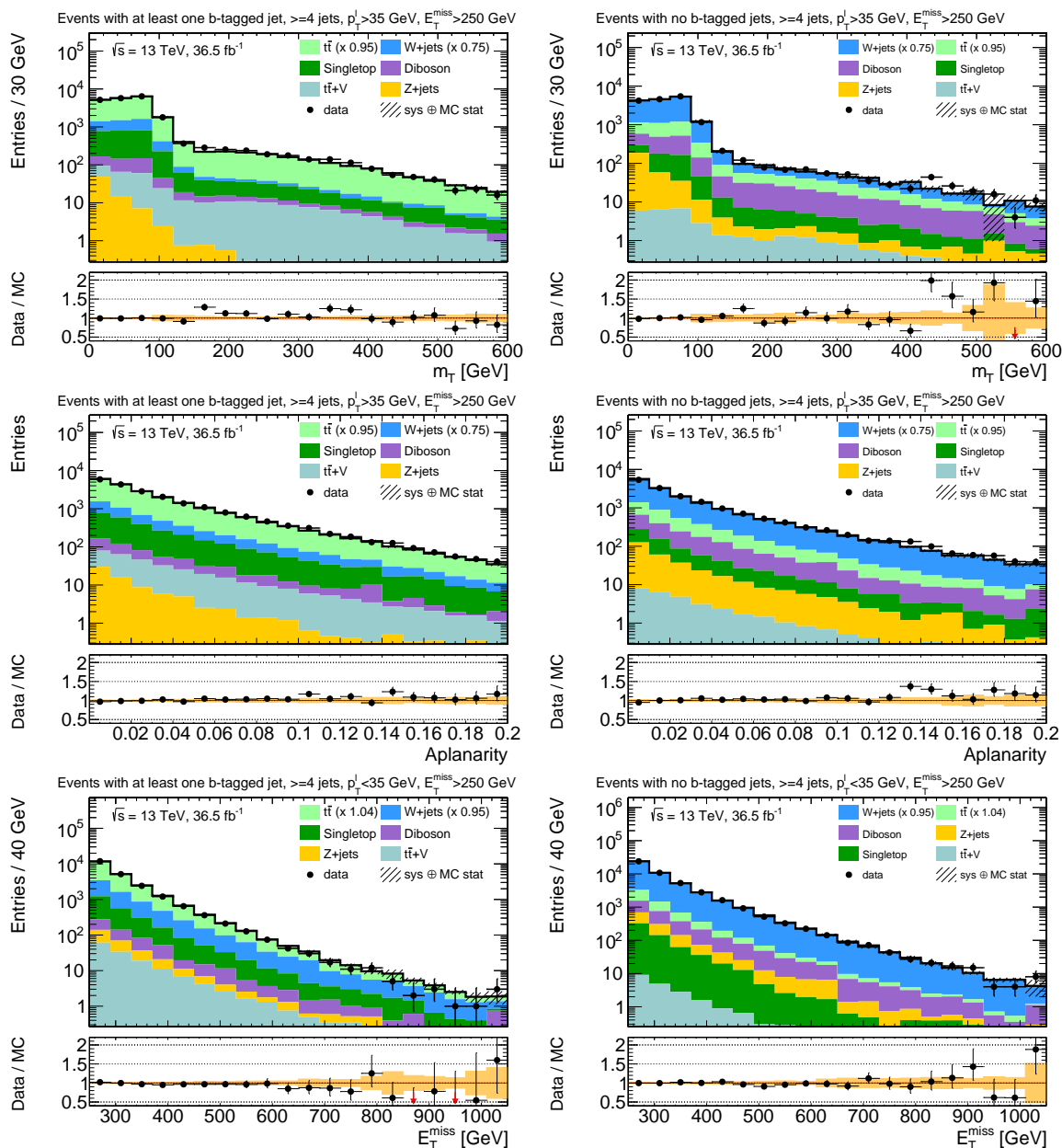


Figure 6.3: Distributions of the observables that are used to extrapolate the control region data to the signal region. Good agreement between data and simulation is found within the experimental uncertainties. The transverse mass  $m_T$  (first row) and the Aplanarity (second row) are used for the **4J-lowx/highx** and **6J** signal region while the **2J** signal region uses  $E_T^{\text{miss}}$  (third row) instead of Aplanarity. The plots for  $m_T$  and Aplanarity are shown after a preselection of at least 4 jets,  $p_T^\ell > 35$  GeV and  $E_T^{\text{miss}} > 250$  GeV and the  $E_T^{\text{miss}}$  distributions after a preselection of at least 2 jets,  $p_T^\ell < 35$  GeV and  $E_T^{\text{miss}} > 250$  GeV.

<b>2J</b>	SR	CR	VR $E_T^{\text{miss}}$	VR $m_T$	
$p_T^\ell$ [GeV]		$> 7(6)$ for $e(\mu)$ and $< \min(5 \cdot N_{\text{jet}}, 35)$			
$N_{\text{jet}}$			$\geq 2$		
$N_{b\text{-jet}}$	$= 0 / \geq 1$	$= 0 / \geq 1$	–	–	
$m_T$ [GeV]	$> 100$	[40, 100]	[40, 100]	$> 100$	
$E_T^{\text{miss}}$ [GeV]	$> 430$	[300, 430]	$> 430$	[300, 430]	
Aplanarity	–	–	–	–	
$E_T^{\text{miss}}/m_{\text{eff}}$	$> 0.25$	$> 0.15$	$> 0.25$	$> 0.1$	
$m_{\text{eff}}$ [GeV]		3 bins $\in$ [700,1900] + [ $> 1900$ ]			
<b>4J high-x</b>	SR	CR	VR Aplanarity	VR $m_T$	VR Hybrid
$p_T^\ell$ [GeV]			$> 35$		
$N_{\text{jet}}$			4–5		
$N_{b\text{-jet}}$	$= 0 / \geq 1$	$= 0 / \geq 1$	–	–	–
$m_T$ [GeV]	$> 450$	[50, 200]	[50, 150]	$> 200$	[150, 450]
$E_T^{\text{miss}}$ [GeV]	$> 300$	$> 300$	$> 250$	$> 250$	$> 250$
Aplanarity	$> 0.01$	$< 0.01$	$> 0.05$	$< 0.01$	[0.01, 0.05]
$E_T^{\text{miss}}/m_{\text{eff}}$	$> 0.25$	$> 0.25$	$> 0.25$	$> 0.25$	–
$m_{\text{eff}}$ [GeV]		2 bins $\in$ [1000,2000] + [ $> 2000$ ]			
<b>4J low-x</b>	SR	CR	VR Aplanarity	VR Hybrid	
$p_T^\ell$ [GeV]			$> 35$		
$N_{\text{jet}}$			4–5		
$N_{b\text{-jet}}$	$= 0 / \geq 1$	$= 0 / \geq 1$	–	–	
$m_T$ [GeV]	150–450	[50, 150]	[50, 150]	[150, 450]	
$E_T^{\text{miss}}$ [GeV]			$> 250$		
Aplanarity	$> 0.05$	[0.01, 0.05]	$> 0.05$	[0.01, 0.05]	
$m_{\text{eff}}$ [GeV]		2 bins $\in$ [1300,2000] + [ $> 2000$ ]			
<b>6J</b>	SR	CR	VR Aplanarity	VR $m_T$	
$p_T^\ell$ [GeV]			$> 35$		
$N_{\text{jet}}$			$\geq 6$		
$N_{b\text{-jet}}$	$= 0 / \geq 1$	$= 0 / \geq 1$	–	–	
$m_T$ [GeV]	$> 175$	[50, 175]	[50, 175]	[175, 400]	
$E_T^{\text{miss}}$ [GeV]	$> 350$	$> 350$	$> 350$	$> 250$	
Aplanarity	$> 0.06$	$< 0.06$	$> 0.06$	$< 0.06$	
$m_{\text{eff}}$ [GeV]		3 bins $\in$ [700,2300] + [ $> 2300$ ]			

Table 6.1: Definitions of selection criteria for the 2-6-jet control and validation regions. The corresponding signal regions from Table 5.3 are shown again, for easier comparison (Table adapted from Ref. [57]).

## 6.5 $t\bar{t}/Wt$ decay modes

In the b-tagged category the background is dominated by the top background. Each of the two  $W$  bosons from the  $t\bar{t}$  or  $Wt$  decay can either decay leptonically or hadronically. Semi-leptonic decays are greatly reduced due to their kinematic endpoint for  $m_T$ . The tail of the  $m_T$  distribution is therefore enriched in events where one branch decays into a hadronically decaying tau ( $\ell\nu\tau_{\text{had}}\nu$ ), or dileptonic decays where the second lepton did not pass the lepton selection (missing lepton) and the event was therefore not vetoed (see Figure 6.4). In contrast to the  $\ell\nu qq$  decays, for the same minimum required number of jets, the  $\ell\nu\tau_{\text{had}}\nu$  decays have one more extra jet<sup>1</sup> from additional radiation and the missing lepton decays two. This raises concern that the  $m_T$  extrapolation may be an unsafe prediction, although loose selections show a good modelling. An alternative way of estimating the  $\ell\nu\tau_{\text{had}}\nu$  and missing lepton top decays was carried out to gain confidence in the background estimation. Here, the data in a 2-lepton control region is extrapolated to the signal region by replacing one lepton into a hadronically decaying  $\tau$  or a missing lepton followed by a recalculation of  $E_T^{\text{miss}}$  and all observables that depend on it. The predicted background of this method was shown to be consistent with the nominal method [57].

---

<sup>1</sup>In this analysis hadronic taus are reconstructed as jets

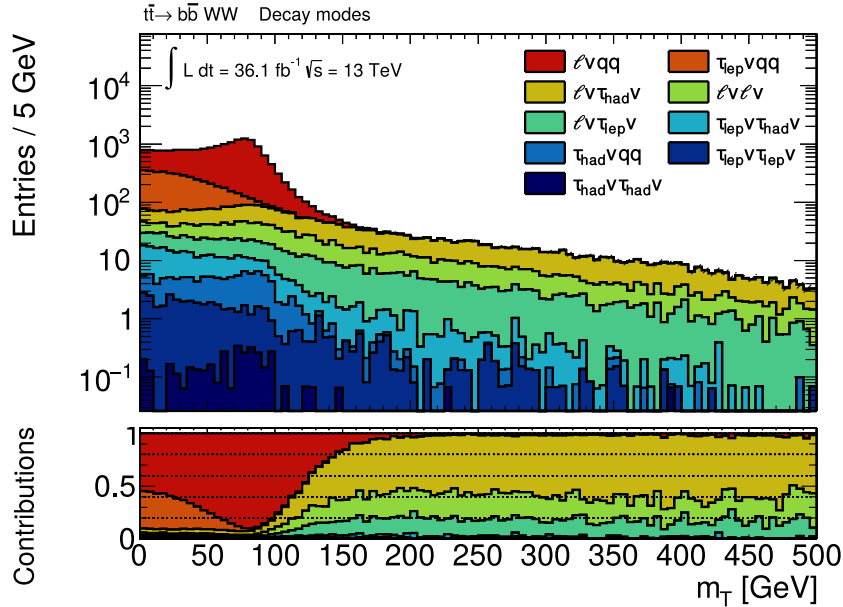


Figure 6.4: Transverse mass distribution for different (non-allhadronic) decay modes of the  $W$  bosons in a  $t\bar{t}$  decay. Far from the kinematic endpoint at the  $W$  boson mass, the semi-leptonic ( $l\nu qq$ ) mode is almost absent and the events are enriched in light lepton+tau ( $l\nu\tau\nu$ ) and dileptonic ( $l\nu l\nu$ ) decays. The taus decay hadronically ( $\tau_{\text{had}}$ ) or leptonically ( $\tau_{\text{lep}}$ ).

## 6.6 Background estimation for the 9-jet signal region

Background predictions from MC simulation in events with high jet multiplicity are challenging. In events with at least 9 jets, all significant contributions from SM processes are events with multiple additional partons from QCD initial state radiation (ISR) or final state radiation (FSR). For the  $t\bar{t}$  process 9-jet events in  $l\nu qq$  decays need to have 5,  $l\nu\tau_{\text{had}}\nu$  6 and  $l\nu l\nu$  decays 7 additional partons to pass the event selection. For the  $W$ +jets process, all jets are coming from additional radiation. It is therefore strongly suppressed in high jet multiplicity events, since the production rate of each further parton is suppressed by the coupling constant  $\alpha_s$  for each additional emission. In all cases the simulation of events with that large number of jets relies on the parton shower procedure and is very sensitive to theoretical uncertainties. The simulation of  $W$ +jets events severely overpredicts the number of events with high jet multiplicities, getting worse with higher number of jets (see Figure 6.5). The jet multiplicity distribution for  $t\bar{t}$  events is modelled well within experimental uncertainties.

To get a reliable estimate of the background as much information as possible is derived from data. This requires to extend the transfer factor approach and determine the transfer factor  $\frac{N_{\text{SR}}}{N_{\text{CR}}}$  from data as well. If two observables are uncorrelated, this can be done since

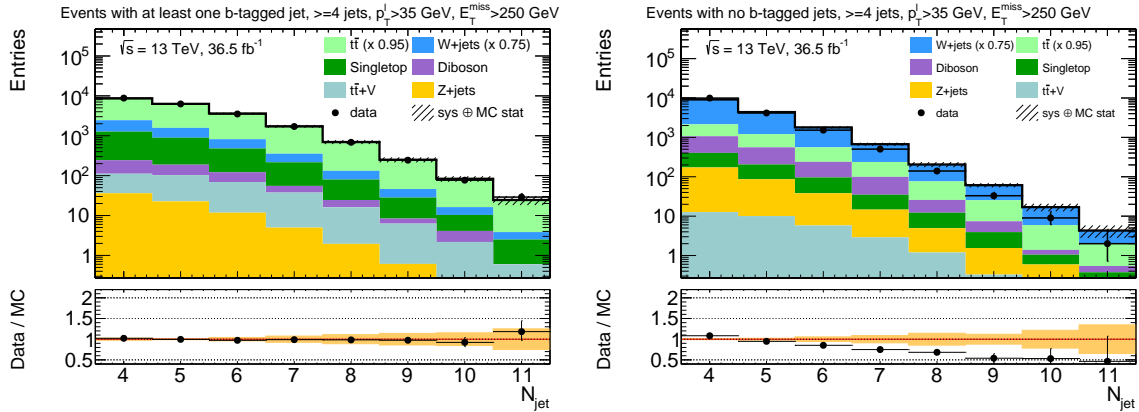


Figure 6.5: Modelling of the jet multiplicity distribution in events with  $p_T^{\ell} > 35 \text{ GeV}$ ,  $E_T^{\text{miss}} > 250 \text{ GeV}$ . The left plot shows events with at least one b-tagged jet, enriched in the top-quark backgrounds, the right plot events with a veto on b-tagged jets, enriched in  $W$ +jets. While the  $t\bar{t}$  MC simulation shows a good description of the jet multiplicity, for  $W$ +jets the number of events in higher jet multiplicities is overpredicted.

the transfer factor in one observable does not change when the selection on the other one is inverted. The approach is often referred to as the *double sidebands* or *ABCD* method. The 2-dimensional plane of the uncorrelated observables is divided into 4 regions  $A$ ,  $B$ ,  $C$  and  $D$  (see Figure 6.6) where  $D$  corresponds to the signal region and  $A$ ,  $B$  and  $C$  to control regions with negligible signal contribution. The background estimate in the signal region  $D$  can then be derived from the observed control region yields  $A$ ,  $B$  and  $C$  by a simple cross multiplication,

$$\frac{A}{B} = \frac{D}{C} \rightarrow D = \frac{A}{B} \cdot C. \quad (6.4)$$

In this analysis, the presumably uncorrelated variables are the jet multiplicity and the transverse mass  $m_T$ . The transfer factor  $\frac{A}{B}$  is given by the ratio of the number of events in the tail of the  $m_T$  distribution to the number of events in the  $m_T$  peak in events with lower number of jets. The details are discussed in the next sections.

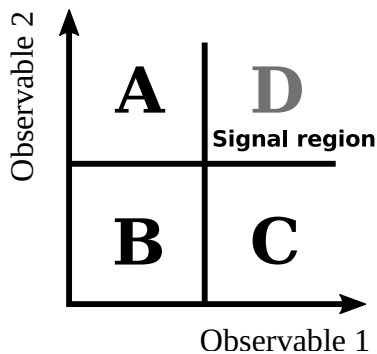


Figure 6.6: Concept for the *ABCD* method. When two observables are uncorrelated, an extrapolation in one of them can be derived from data by inverting the requirement on the other one.

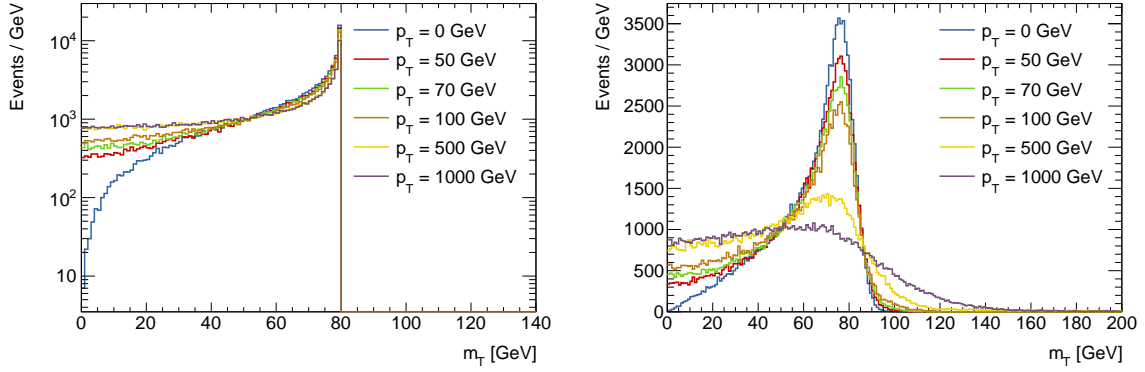


Figure 6.7: Transverse mass distribution of 2 massless particles, coming from the decay of an 80 GeV particle. The distributions for different transverse boosts  $p_T$  of the initial particle are shown. For the right plot a smearing of 10% for the components of one of the 4-vectors is applied. This gives an idea of the impact of finite  $E_T^{\text{miss}}$  resolution.

### 6.6.1 Motivation

The background estimation for the 9-jet signal region assumes the transverse mass  $m_T$  to be invariant for different number of jet events. The main influences on the transverse mass shape from leptonic  $W$  boson decays are the  $E_T^{\text{miss}}$  resolution and the transverse boost of the  $W$  boson (see Figure 6.7). If selection criteria fix the distribution of  $W$  boson transverse momenta and lead to a regime with consistent  $E_T^{\text{miss}}$  resolution, then the  $m_T$  distribution should not depend on the number of jets. The similar distribution of boosts is ensured by common cuts on  $m_{\text{eff}}$  and the  $E_T^{\text{miss}}$  resolution by a cut on the  $E_T^{\text{miss}}$  significance  $E_T^{\text{miss}}/\sqrt{H_T}$ . Without this cut, events at higher jet multiplicities show a larger fraction of events where too much  $E_T^{\text{miss}}$  is reconstructed. After applying the criterion  $E_T^{\text{miss}}/\sqrt{H_T} > 8 \text{ GeV}^{1/2}$  the  $E_T^{\text{miss}}$  resolution looks similar for lower and higher jet multiplicities (see Figure 6.8). Figure 6.9 shows the  $m_T$  distribution for different number of jet events.

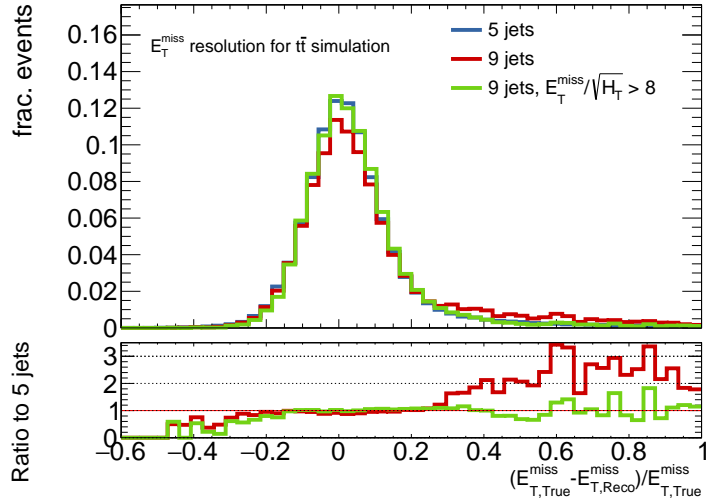


Figure 6.8: The  $E_T^{\text{miss}}$  resolution in simulated  $t\bar{t}$  events for events with 5 and 9 jets. After applying the  $E_T^{\text{miss}}/\sqrt{H_T}$  cut, the enlarged tail for too much reconstructed  $E_T^{\text{miss}}$  in 9-jet events goes back to the same level as for 5-jet events. The *true*  $E_T^{\text{miss}}$  is calculated by the sum of neutrino momenta in the simulation.

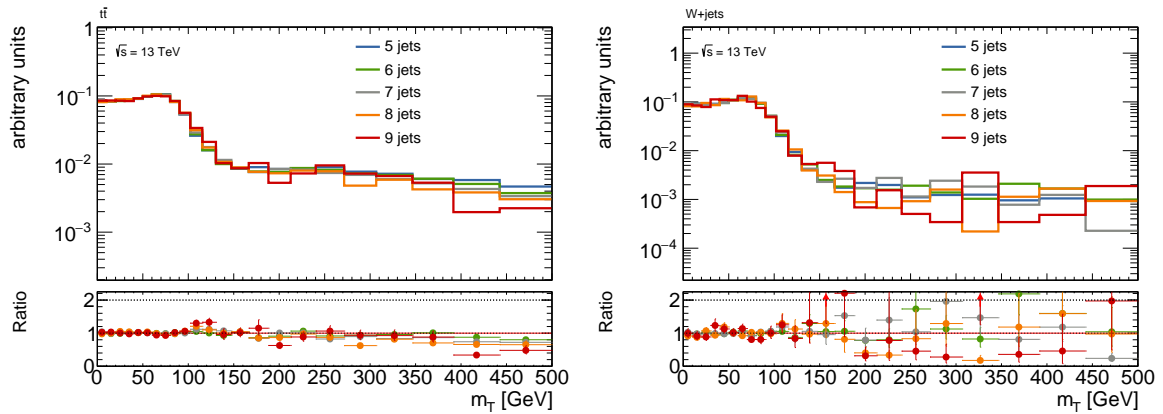


Figure 6.9: The  $m_T$  distribution in events with different numbers of jets for  $t\bar{t}$  (left) and  $W$ +jets (right) after a common selection of  $m_{\text{eff}} > 1000$  GeV and  $E_T^{\text{miss}}/\sqrt{H_T} > 8$  GeV $^{1/2}$ .

### 6.6.2 Region definitions

Figure 6.10 shows the configuration that is used in the background estimation for the 9-jet signal region. The precise cut values are given in Table 6.2. The selection was optimised to keep the control regions as close as possible to the signal region, while maintaining a reasonable amount of statistics to keep the uncertainties on the fit parameters acceptable. Except for the jet multiplicity and  $m_T$ , the selections were chosen to be the same for all regions to keep the  $m_T$  shape invariant for events with different number of jets. A compromise had to be made for the Aplanarity selection. The closeness to the signal regions induces potential signal contamination in the control regions. To keep the relative signal contamination in the high  $m_T$ , low  $N_{\text{jet}}$  region  $A$  low, the Aplanarity cut had to be dropped for the low  $N_{\text{jet}}$  regions. The control regions  $A$  and  $B$  select events with 5-6 jets. The low  $m_T$  regions  $B$  and  $C$  have an upper cut on  $m_T$  of 100 GeV. Gaps in  $m_T$  and  $N_{\text{jet}}$  between the control regions  $A, B, C$  and the signal region serve as validation regions where the setup is repeated similarly with the control regions  $A'$  and  $C'$ . The region VR  $m_T$  validates the extrapolation of the  $m_T$  transfer factor from lower jet multiplicity data to higher jet multiplicities and the region VR  $N_{\text{jet}}$  shows the validity of the method in 9-jet events, at intermediate  $m_T$ . To keep potential signal contamination at an acceptable level, an upper cut on  $\text{Aplanarity} < 0.05$  had to be applied for VR  $m_T$ , control region  $C'$  and VR  $N_{\text{jet}}$ . Figure 6.11 shows the regions and corresponding signal grids where potential contamination was found to be largest. The other regions and all signal grids considered in this thesis have also been checked (see Appendix B). After the mentioned compromises in selection criteria, the signal contamination was found acceptable in all regions for signal models that were not excluded by previous search results. Signal contaminations in control regions are shown in terms of the relative signal contributions  $s/b$ , since this measures best how a signal in this region would bias the background normalisation. In the validation region the contamination is measured in terms of  $s/\sqrt{b}$  which resembles the significance of an excess that would be seen if this signal would be present and therefore lead to a wrong conclusion about the modelling of the background.

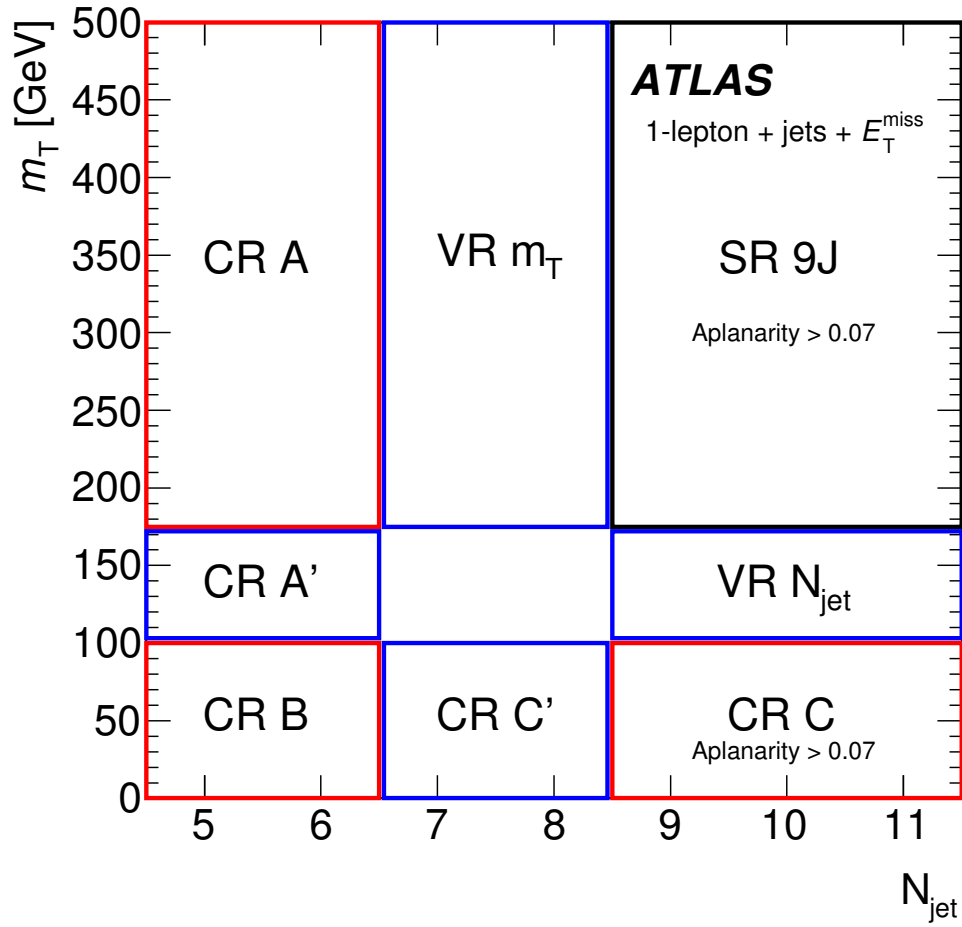


Figure 6.10: Setup for the 9-jet control, validation and signal regions in the  $m_T$  versus  $N_{\text{jet}}$  plane (Figure contributed to [57] by the author).

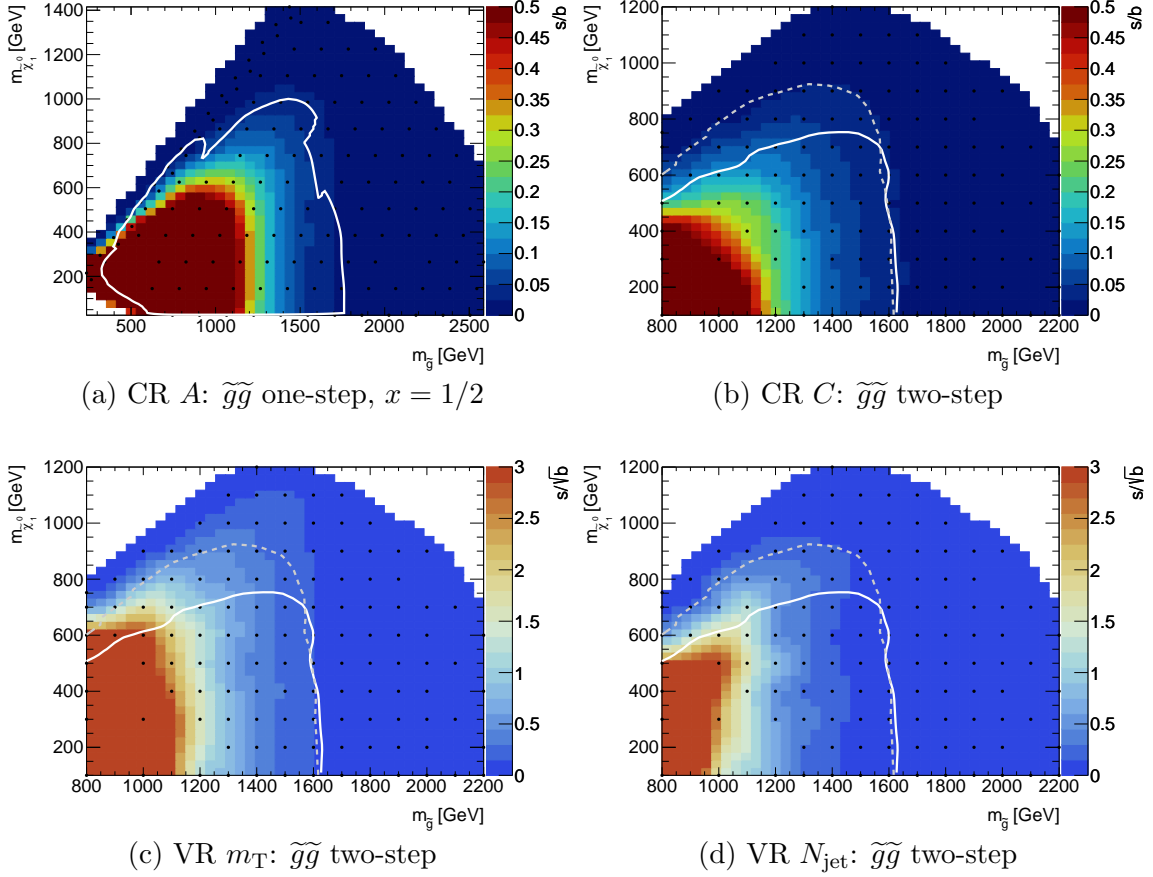


Figure 6.11: Signal contaminations for CR  $A$ ,  $C$  and the two validation regions VR  $m_T$ ,  $N_{\text{jet}}$ . Each plot shows the signal contamination from MC for the signal model with the strongest signal contaminations. For the control regions the signal contamination is evaluated in terms of the signal over background ratio  $s/b$  and for the validation regions in terms of  $s/\sqrt{b}$ . For points that were not already excluded by previous analyses, the signal contamination is low enough to neither impact the background estimation in case of a signal appearing in the control regions, nor to change the conclusions about its validity in case of a signal appearing in the validation regions. The lines in the plots correspond to preliminary ATLAS results that were publicly available at the time the regions were designed. The solid line for the  $\tilde{g}\tilde{g}$  one-step grid shows the limit set by the 1-lepton analysis [113], the solid line for the  $\tilde{g}\tilde{g}$  two-step grid the limit from the 0-lepton multijet analysis [118] and the dashed line the limit from the same-sign/3-lepton analysis [119].

<b>9J</b>	CR <sub>A</sub>	CR <sub>B</sub>	CR <sub>C</sub>	VR $m_T$	CR <sub>C'</sub>	VR $N_{\text{jet}}$	CR <sub>A'</sub>
$p_T^\ell$ [GeV]				$\geq 35$			
$N_{\text{jet}}$	5–6	5–6	$\geq 9$	7–8	7–8	$\geq 9$	5–6
$N_{b\text{-jet}}$	= 0 / $\geq 1$	= 0 / $\geq 1$	= 0 / $\geq 1$	–	= 0 / $\geq 1$	–	= 0 / $\geq 1$
$m_T$ [GeV]	> 175	< 100	< 100	> 175	< 100	[100, 175]	[100, 175]
$E_T^{\text{miss}}$ [GeV]				> 200			
$E_T^{\text{miss}}/\sqrt{H_T}$				$\geq 8$			
Aplanarity	–	–	> 0.07	< 0.05	< 0.05	< 0.05	–
$m_{\text{eff}}$ [GeV]	> 1000	> 1000	> 1000	[1000, 1500], [> 1500]	> 1000	> 1000	> 1000

Table 6.2: Overview of the selection criteria for control and validation regions for the **9J** SR. The control regions (Table adapted from [57])

### 6.6.3 Invariance of the transverse mass distribution

Several assumptions of an invariant  $m_T$  shape for different jet multiplicity events have been checked in simulation for the finally chosen selection. In particular, this involves comparing events with 5–6 jets and no requirement on Aplanarity to events with 7–8 jets and an upper cut of Aplanarity < 0.05 and events with at least 9 jets and Aplanarity > 0.07. The  $m_T$  distribution is compared in three bins:  $m_T < 100$  GeV,  $100 \text{ GeV} < m_T < 175$  GeV and  $m_T > 175$  GeV, since those are the relevant ranges for the control, validation and signal regions. The **9J** SR is by far dominated by the top backgrounds. Most plots are focused on validating the assumption for  $t\bar{t}$  and single top. Figure 6.12 shows the  $E_T^{\text{miss}}$  resolution and the  $m_T$  bins for the relevant selections for the  $t\bar{t}$  background. For the nominal samples, the  $m_T$  tail to peak fraction in the high  $N_{\text{jet}}$  selection is consistent within 10% with the 5–6 jets selection for the signal regions and within 20% for the validation regions. Further studies can be found in appendix C.

### 6.6.4 Statistical model

Most of the conclusions about the invariance of the transverse mass shape are based on MC simulation. The knowledge of the non-correlation of  $m_T$  and  $N_{\text{jet}}$  is therefore subject to uncertainties. A potential deviation from this assumption can be formulated in terms of the closure factor  $f_{\text{Closure}}$ , the ratio of the raw MC prediction to the MC prediction from the  $ABCD$  estimate (equation 6.4), or in other words the ratio of transfer factors,

$$f_{\text{Closure}} = \left( \frac{D}{C \cdot \frac{A}{B}} \right)_{\text{MC}} = \left( \frac{D}{C} / \frac{A}{B} \right)_{\text{MC}}. \quad (6.5)$$

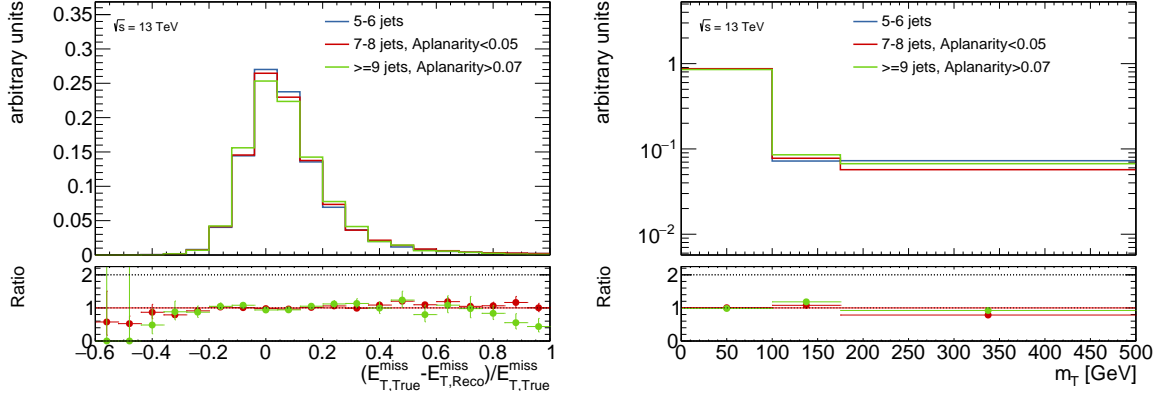


Figure 6.12: The  $E_T^{\text{miss}}$  resolution (left) and  $m_T$  bins (right) for the selections that are relevant for the control, signal and validation regions for the  $t\bar{t}$  background.

In case of no correlation,  $f_{\text{Closure}} = 1$ . Similar to the transfer factor approach, the setup in the regions  $A, B, C, D$  can be formulated as a likelihood fit. Here,  $f_{\text{Closure}}$  is the only parameter that has to be predicted from simulation. Three fit parameters are needed:

$$\begin{aligned}
 N_{\text{bkg},A,\text{pred}} &= \left( \frac{N_A}{N_B} \right)_{\text{fit}} \times N_{B,\text{fit}} \times 1 &= \mu_{A/B,\text{fit}} \times \mu_{B,\text{fit}} \times b_A & (6.6) \\
 N_{\text{bkg},B,\text{pred}} &= N_{B,\text{fit}} \times 1 &= \mu_{B,\text{fit}} \times b_B \\
 N_{\text{bkg},C,\text{pred}} &= N_{C,\text{fit}} \times 1 &= \mu_{C,\text{fit}} \times b_C \\
 N_{\text{bkg},D,\text{pred}} &= \left( \frac{N_A}{N_B} \right)_{\text{fit}} \times N_{C,\text{fit}} \times f_{\text{Closure}} = \mu_{A/B,\text{fit}} \times \mu_{C,\text{fit}} \times b_D
 \end{aligned}$$

The values  $b_A, b_B, b_C, b_D$  correspond to the total background predictions from MC in the regions  $A, B, C, D$ . Again, the two equivalent formulations are related to each other by scaling the free fit parameters by a constant factor,

$$\begin{aligned}
 \mu_{A/B,\text{fit}} &= \frac{b_B}{b_A} \times \left( \frac{N_A}{N_B} \right)_{\text{fit}} \\
 \mu_{B,\text{fit}} &= \frac{1}{b_B} \times N_{B,\text{fit}} \\
 \mu_{C,\text{fit}} &= \frac{1}{b_C} \times N_{C,\text{fit}}
 \end{aligned}$$

The formulation after the first equality sign in equations 6.6 can be seen as a modification of the  $ABCD$  method, where the predicted yield is corrected by the simulation based factor  $f_{\text{Closure}}$ , while the formulation after the second equality sign indicates an extension of the

normalisation factor approach by the additional fit parameter  $\mu_{A/B}$ . The second approach was chosen to model the background estimation for the **9J** signal region (corresponding to Region D). The normalisation factor  $\mu_{A/B}$  scales the predicted ratio of high  $m_T$  to low  $m_T$  events, while the parameter  $\mu_C$  corresponds to the normalisation in the **9J** control region. For the validation regions, the setup is repeated in the same way. Figure 6.13 shows an overview of the parameters applied in the different regions. All parameters exist twice, to simultaneously scale the Top ( $t\bar{t}$  and single top) and  $W$ +jets contributions. The control regions are therefore split in two categories, one requiring at least one b-tagged jet and the other one with a veto on b-tagged jets. This requires the b-tagging efficiencies for  $W$ +jets and the Top backgrounds as an additional information from MC simulation.

The signal region is split into bins in  $m_{\text{eff}}$ . Since the available data statistics in the 9-jet control region  $C$  is not sufficient to perform the background estimation bin-by-bin (like for the 2-6-jet signal regions) and the signal contamination in such a binned region would become too large, the normalisation factors are applied for all bins in  $m_{\text{eff}}$ . This limits the range of  $m_{\text{eff}}$  that can be used to avoid being affected by the mismodelling seen for high  $m_{\text{eff}}$ . A split into  $1000 \text{ GeV} < m_{\text{eff}} < 1500 \text{ GeV}$  and  $m_{\text{eff}} > 1500 \text{ GeV}$  has been shown to be well described<sup>2</sup> by normalisation factors applied for both bins. In this setup, the efficiency  $\epsilon_i = \frac{N_{\text{bin } i, \text{SR}}}{N_{\text{tot}, \text{SR}}}$  of the  $m_{\text{eff}}$  selection for each of the two bins  $D_i$  is an additional information that has to be provided by simulation and affected by uncertainties. The total correction factor for each bin is

$$f_{\text{Closure}} \cdot \epsilon_i = \left( \frac{D}{C \cdot \frac{A}{B}} \right) \cdot \frac{D_i}{D} = \frac{D_i}{C \cdot \frac{A}{B}} \quad (6.7)$$

The validation region VR  $m_T$  is split in the same bins, to validate the extrapolation into the bins.

---

<sup>2</sup>This will be seen later by the good agreement of data and background prediction in VR  $m_T$

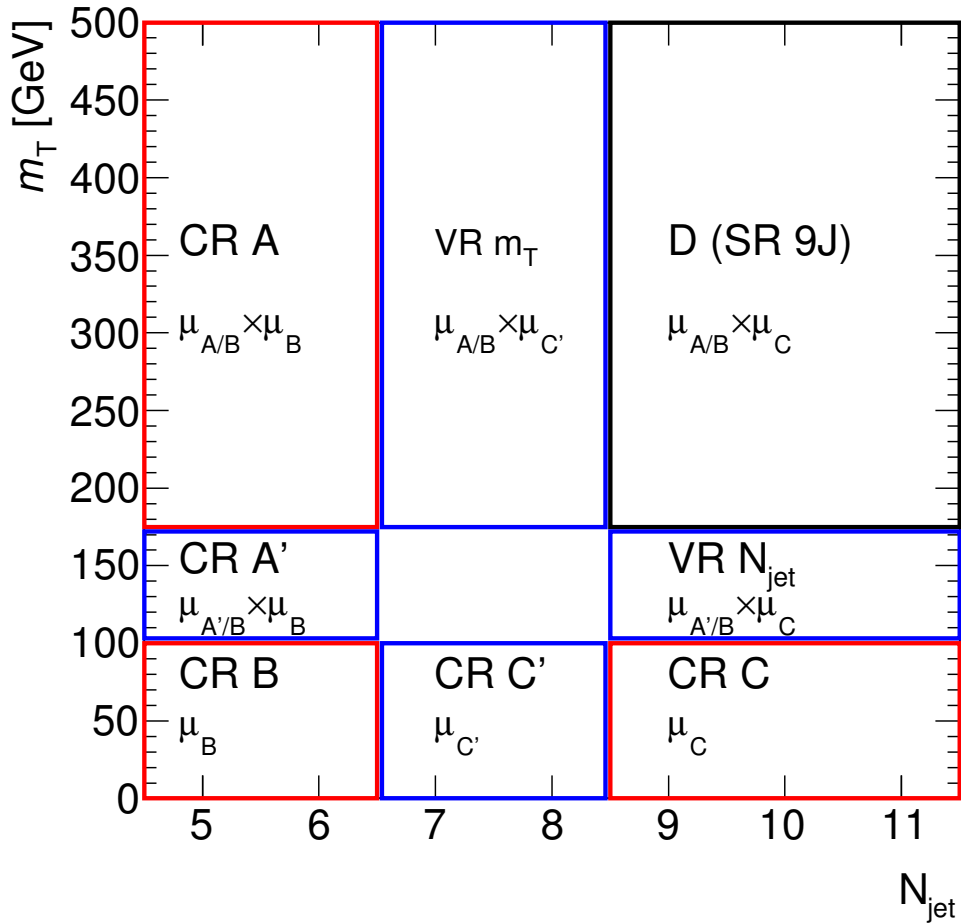


Figure 6.13: Normalisation parameters in the statistical model for the  $9J$  signal region background estimation. For the regions VR  $m_T$  and VR  $N_{jet}$ , the normalisation factor from the background-only fit is applied for validation, but the regions do not participate in the fit. Each parameter exists twice, one for the Top backgrounds and one for  $W$ +jets. The control regions are split in one b-tag and one b-veto category.

# Chapter 7

## Uncertainties

### 7.1 Experimental uncertainties

The reconstruction, calibration and certain selection efficiencies of the analysis objects are subject to uncertainties. They are provided as up and down variations which are either applied as event weights (for efficiency uncertainties) or as changed parameters in the reconstruction and calibration. For the latter, the object selection is repeated for each variation.

#### 7.1.1 Scale factors

One category of experimental uncertainties is related to the imperfect detector simulation. Efficiencies of object selections in data do not always match the ones in simulation. In some cases efficiencies can be measured in data and the MC efficiency is scaled to match reproduce the measured efficiencies.

The event wise efficiency is given by the product of efficiencies for objects that passed a selection and inefficiencies for products that failed the selection,

$$\epsilon_{\text{event}} = \prod_{i \in \text{passed}} \epsilon_i \prod_{i \in \text{failed}} (1 - \epsilon_i).$$

The scale factor is then given by  $\frac{\epsilon_{\text{event,Data}}}{\epsilon_{\text{event,MC}}}$ . Uncertainties on the efficiency determination are propagated to the scale factor. This procedure is applied for the JVT and the b-tagging efficiency. The JVT efficiencies are measured in  $Z \rightarrow \mu\mu + \text{jets}$  events [91]. The efficiency of the b-tagging selection is measured in  $t\bar{t}$  events with two leptons for b, c and light quark jets, with a method similar to the one used during Run 1 [120]. The uncertainty parameters correspond to variations of the three different efficiencies and uncertainties on the extrapolation of the measured efficiencies to high  $p_T$ .

The electron and muon efficiencies are applied as efficiency corrections on the signal object only. Electron reconstruction, identification and isolation efficiencies are determined

from  $Z \rightarrow ee$  events with the tag and probe method, where one electron is identified by tight selection criteria, and the other one, only satisfying criteria for compatibility of the electron pair with the  $Z$  boson mass window, is used to determine the efficiencies [94]. Three independent systematic variations for the reconstruction, identification and isolation efficiencies are used in this analysis. A similar procedure is performed for the muons [95], where efficiencies of reconstruction (+identification), isolation and track to vertex association are determined by a tag and probe method with  $Z \rightarrow \mu\mu$  events and  $J/\psi \rightarrow \mu\mu$  events for lower  $p_T$  muons. Also here, a parameter set with independent variations for the three efficiencies is used.

### 7.1.2 Pileup reweighting and luminosity

The distribution of the number of average interactions per bunch crossing  $\langle\mu\rangle$  and the number of reconstructed primary vertices  $N_{\text{Vertex}}$  depends on the luminosity of the respective data runs. Since the MC samples were generated before the full data was taken, the number of simultaneous interactions in simulation does not generally follow the same distribution as in data. The  $\langle\mu\rangle$  distribution in MC is therefore reweighted to the distribution in data. To cover differences between the measured inelastic p-p cross section [121] and the cross section predicted by the MC generator,  $\langle\mu\rangle$  in data is scaled by a factor of 1/1.09 before reweighting MC to the data distribution. The scaling of the  $\langle\mu\rangle$  value in data is preferred instead to scaling the value in MC, since the MC is generated for discrete values of  $\langle\mu\rangle$ , while the value in data is continuous.

The difference between not applying the scale factor and applying a stronger scale factor of 1/1.18 determines the uncertainty on the pileup reweighting. The distributions of  $\langle\mu\rangle$  and  $N_{\text{Vertex}}$  do not simultaneously match after the reweighting, but the uncertainty covers the discrepancies (see Figure 7.1).

The luminosity was determined from a preliminary calibration by x-y beam-separation scans (*van der Meer scans*) performed in August 2015 and May 2016. The uncertainty on the combined 2015+2016 integrated luminosity is 3.2%. The methodology is described in Ref. [122].

### 7.1.3 Jets

The calibration of jets to the absolute JES and the applied corrections, including the in-situ corrections from data/MC (see Section 3.5.2) comparisons are subject to uncertainties. This analysis uses a set of 21 systematic variations, provided by the ATLAS Jet/ $E_T^{\text{miss}}$  group [89]. The first 7 parameters are determined by an eigenvalue decomposition of the covariance matrix of parameters that influence the in-situ calibrations. They correspond to 6 leading principal components and a 7th parameter that combines the remaining components. This keeps the numbers of parameters reasonable while maintaining the description of jet-jet correlations in the parameters. Of the remaining 13 parameters three are related

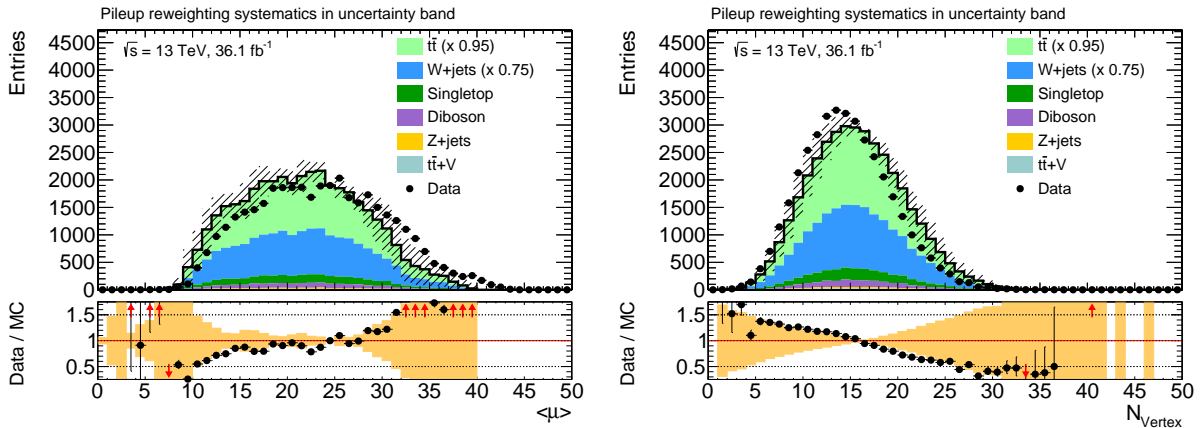


Figure 7.1: The  $\langle \mu \rangle$  (left) and  $N_{\text{Vertex}}$  (right) distribution in data and MC. Due to different inelastic p-p cross sections in data and MC the  $\langle \mu \rangle$  and  $N_{\text{Vertex}}$  distribution cannot be simultaneously matched by reweighting one distribution. This is accounted for by a data scale factor that is applied to the  $\langle \mu \rangle$  values in data before reweighting the MC. The variation of this factor covers the discrepancies (included in the uncertainty band in the plots).

to the  $\eta$  inter calibration, where the energy of well measured central jets is compared to forward jets that balance in  $p_T$ . Four parameters describe the uncertainties of the pileup corrections and three the different jet energy responses of light-quark, b-quark and gluon initiated jets. Another parameter is a dedicated uncertainty for jets that are not contained in the calorimeter, leading to additional hits in the muon spectrometer (*punch-through* jets) and a last parameter is dedicated to samples that use the fast detector simulation.

The difference between the jet energy resolution (JER) [123] in data and MC is applied as the nominal smearing to the jets in MC. An alternative smearing based on the systematic uncertainties on the JER measurement is applied as a single systematic variation.

#### 7.1.4 Electron and Muon calibration

The uncertainties on the electron calibration [93] are combined into two parameters, one varying the energy scale and another one the energy resolution (smearing in MC). The muon momentum scale and resolution are measured in  $Z \rightarrow \mu\mu$  and  $J/\psi \rightarrow \mu\mu$  events [95]. The uncertainties are combined into one parameter for the momentum scale and two parameters for the resolution, one of the inner detector track and the other one of the muon spectrometer track.

Signal region	2J <i>b</i> -tag	2J <i>b</i> -veto	4J high- <i>x</i> <i>b</i> -tag	4J high- <i>x</i> <i>b</i> -veto
Total background expectation	55.07	39.95	57.03	52.23
Total statistical ( $\sqrt{N_{\text{exp}}}$ )	$\pm 7.42$	$\pm 6.32$	$\pm 7.55$	$\pm 7.23$
Total experimental uncertainty	$\pm 1.54$ [2.8%]	$\pm 2.43$ [6.1%]	$\pm 2.82$ [5.0%]	$\pm 5.82$ [11.1%]
JES and JER	$\pm 0.64$	$\pm 1.78$	$\pm 2.11$	$\pm 3.28$
JVT efficiency	$\pm 0.01$	$\pm 0.01$	$\pm 0.03$	$\pm 0.11$
B-tagging efficiency	$\pm 1.24$	$\pm 1.35$	$\pm 1.19$	$\pm 1.26$
Lepton efficiency	$\pm 0.26$	$\pm 0.55$	$\pm 0.50$	$\pm 0.59$
Lepton calibration	$\pm 0.13$	$\pm 0.40$	$\pm 0.63$	$\pm 0.88$
$E_{\text{T}}^{\text{miss}}$ track soft terms	$\pm 0.33$	$\pm 0.43$	$\pm 0.21$	$\pm 0.17$
Pileup reweighting	$\pm 0.49$	$\pm 0.49$	$\pm 1.18$	$\pm 4.51$

Table 7.1: Breakdown of the experimental uncertainties on the total background in the **2J** and **4J high-*x*** signal regions. For background components that are normalised in control regions, the contribution of the uncertainty was evaluated on the transfer factor. The percentages show the size of the uncertainty relative to the total expected background.

### 7.1.5 Missing transverse energy

The  $E_{\text{T}}^{\text{miss}}$  calculation is repeated for all systematic variations of the analysis objects. The uncertainty on the track soft terms (TST) is determined in  $Z \rightarrow \mu\mu$  events, where the hard objects and soft terms are expected to cancel in case of perfect  $E_{\text{T}}^{\text{miss}}$  resolution [96]. The soft term scale and resolution can then be inferred from the hard objects. The uncertainty on the absolute scale of the TST is combined in one parameter while the uncertainty on the resolution of the TST is expressed in two parameters, corresponding to the components parallel and perpendicular to the total transverse momentum of the hard objects.

### 7.1.6 Impact on signal regions

Tables 7.1 and 7.2 show the impact on the total background predictions of the different experimental uncertainties for the 2-6-jet signal regions. The dominant uncertainties arise from the JES and JER, and the *b*-tagging efficiencies. The sometimes large contributions from pileup reweighting originate from statistical fluctuations in the MC samples. The total experimental uncertainty is between 3% and 13.5%, depending on the signal regions. In most cases this is significantly lower than the statistical uncertainty. The given statistical uncertainty  $\sqrt{N_{\text{exp}}}$  is not directly used, but rather given for comparison to show roughly the impact of limited overall statistics on the sensitivity.

Signal region	4J low-x $b$ -tag	4J low-x $b$ -veto	6J $b$ -tag	6J $b$ -veto
Total background expectation	35.20	19.08	28.49	9.90
Total statistical ( $\sqrt{N_{\text{exp}}}$ )	$\pm 5.93$	$\pm 4.37$	$\pm 5.34$	$\pm 3.15$
Total experimental uncertainty	$\pm 2.06$ [5.9%]	$\pm 1.29$ [6.8%]	$\pm 1.09$ [3.8%]	$\pm 1.33$ [13.5%]
JES and JER	$\pm 1.53$	$\pm 0.94$	$\pm 0.88$	$\pm 1.19$
JVT efficiency	$\pm 0.07$	$\pm 0.00$	$\pm 0.02$	$\pm 0.03$
B-tagging efficiency	$\pm 0.92$	$\pm 0.78$	$\pm 0.47$	$\pm 0.53$
Lepton efficiency	$\pm 0.03$	$\pm 0.09$	$\pm 0.06$	$\pm 0.04$
Lepton calibration	$\pm 0.15$	$\pm 0.07$	$\pm 0.14$	$\pm 0.14$
$E_{\text{T}}^{\text{miss}}$ track soft terms	$\pm 0.19$	$\pm 0.37$	$\pm 0.10$	$\pm 0.11$
Pileup reweighting	$\pm 1.00$	$\pm 0.14$	$\pm 0.41$	$\pm 0.23$

Table 7.2: Breakdown of the experimental uncertainties on the total background in the **4J low-x** and **6J** signal regions. For background components that are normalised in control regions, the contribution of the uncertainty was evaluated on the transfer factor. The percentages show the size of the uncertainty relative to the total expected background.

## 7.2 Theory uncertainties

Theory uncertainties arise from parameters in the MC simulation. Those include unphysical scales that have to be introduced due to finite order calculations. Most of them affect the amount and hardness of additional radiation. Varying those parameters determines an uncertainty on the prediction. Another method is to compare different simulation techniques, e.g. different shower programs or matching schemes.

In contrast to the evaluation of experimental uncertainties, theory uncertainties affect the event kinematics prior to any detector simulation. The full propagation of all variations is therefore very computing intense. For some samples and variations, the full simulation chain was ran, but with less simulated events. For other cases, approximations were made that use directly objects before detector simulation.

For backgrounds that are normalised in control regions the variations are propagated bin-by-bin to the transfer factor  $N_{\text{SR}}/N_{\text{CR}}$  and applied in the 2-6-jet signal and validation regions and on  $f_{\text{Closure}} \cdot \epsilon_i$  (see Equation 6.7) for the 9-jet signal and validation region bins. This is the case for the top ( $t\bar{t}$  and single top) and  $W$ +jets backgrounds. For the other processes, the uncertainties are evaluated on the predicted yield in each bin in the signal, control and validation regions. When statistically independent samples are compared, the MC statistical uncertainty is added in quadrature to the variation, but the sign of the variation (up or down) is kept. For comparisons between the nominal sample and one alternative, the full difference is taken as a symmetric up and down variation. If an up and a down variation are given, the uncertainty is taken symmetrically as half the total

difference.

### 7.2.1 Truth selection

When variations are evaluated on objects before detector simulation, the event selection is run on objects that are directly reconstructed from the generator level objects. Jets are clustered by an anti- $k_t$  algorithm, radius parameter  $R = 0.4$  with truth particles as input. They are flagged as b-tagged jets, if at least one b-quark hadron with  $p_T > 5 \text{ GeV}$  was associated to the jet. Electrons and muons correspond to the truth particles from the hard interaction.  $E_T^{\text{miss}}$  is created from the vector sum of the transverse momenta of non-interacting particles.

### 7.2.2 Backgrounds

The choice of variations follows closely the recommendations from the ATLAS physics modelling group [58–61]. They are considered for the following processes.

#### $t\bar{t}$ and Single top

Both for  $t\bar{t}$  and Single top, systematic variations include the change of additional radiation, comparing different showering programs or exchanging the matrix element generator. More or less additional QCD radiation is achieved by simultaneously varying several parameters in the POWHEG+PYTHIA6 samples. The showering of the nominal sample with PYTHIA6 is compared to HERWIG++ [124]. The matrix element generation and matrix element to parton shower matching is compared between POWHEG-BOX and MADGRAPH5\_AMC@NLO.

Most variations have a large impact on the  $m_{\text{eff}}$  distribution and the jet multiplicity while the  $m_T$  and Aplanarity distribution which are used for extrapolation between control and signal region are affected less (see Figure 7.2 and 7.3). Since the top background is normalised in control regions with the same requirements on the jet multiplicity and  $m_{\text{eff}}$  as the signal region, the large variations in the jet multiplicity and  $m_{\text{eff}}$  have little effect on the background prediction.

For the 9-jet signal region the variations on  $m_{\text{eff}}$  can have an effect, since the two  $m_{\text{eff}}$  bins are not normalised independently. Figure 7.4 shows the  $t\bar{t}$  variations for the 9-jet signal region. The variations are mainly dominated by the MC statistical uncertainty of the variational samples. The  $t\bar{t}$  theory uncertainties correspond to the dominant systematic uncertainties for the 9-jet signal region. Nevertheless, the sensitivity is not limited by systematic uncertainties, since the statistical uncertainty on the total event count is still in the same order.

For the single top background an additional uncertainty arises from the neglected interference between the  $Wt$  (with 2 b quarks in the final state) and  $t\bar{t}$  process. The size

of this effect is estimated by comparing a  $WWbb$  sample that includes the interference generated by MADGRAPH5\_AMC@NLO with the sum of  $t\bar{t}$  and  $Wt$  production. For the 9-jet signal region, the statistics of this sample was not sufficient to evaluate the impact of this variation. A conservative uncertainty of 80% on the single top contribution was used instead, based on the largest deviations observed in previous versions of the analysis [113], which were derived by comparing samples with diagram removal and diagram subtraction schemes [125].

### $W/Z$ +jets and Diboson

For the Sherpa  $W/Z$ +jets samples, as well as the Diboson samples, different scales are varied independently up and down. In addition, the Sherpa  $W/Z$ +jets samples are compared to samples generated with MADGRAPH5\_AMC@NLO and the Sherpa Diboson samples to POWHEG+PYTHIA. For the  $W$ +jets contribution in each b-tag bin an uncertainty of 30% per bin on the modelling of heavy flavour (b or c quark) jets is introduced.

In the 9-jet signal region, the contribution from  $W$ +jets is subdominant and the uncertainty on its contribution dominated by the limited data statistics in the b-veto category of the 9-jet control region CR C. The  $Z$ +jets contribution is negligible. Nevertheless, an uncertainty of 50% is introduced for both the  $W/Z$ +jets samples with a negligible impact on the total background prediction. For the diboson contribution the uncertainty for the 9-jet signal region and corresponding control and validation regions is estimated from truth samples based on the number of jets in the respective selections since the variations have the largest impact on the  $N_{\text{jet}}$  distribution (see Figure 7.5). The diboson background has a small contribution in the 9-jet signal region but it affects the uncertainty on the  $W$ +jets estimation, since the contribution in the b-veto category of the 9-jet control region CR C is significant.

### 7.2.3 Signal

For most signal models considered in this thesis, the event kinematics is dominated by the decay products of heavy SUSY particles. Jets are highly energetic and well separated and additional radiation has little impact on the observables. Those signals are therefore less affected by theoretical uncertainties as the backgrounds, where ISR and FSR play an important role. Significant theory uncertainties arise for signals with compressed spectra, where additional radiation is needed to pass the event selection and dominates the event kinematics. The uncertainties correspond to variations of the scales in the MADGRAPH5\_AMC@NLO parameters and the PYTHIA parameters and range from around 1% for signal models with large mass splittings to 35% for signals with compressed spectra [57].

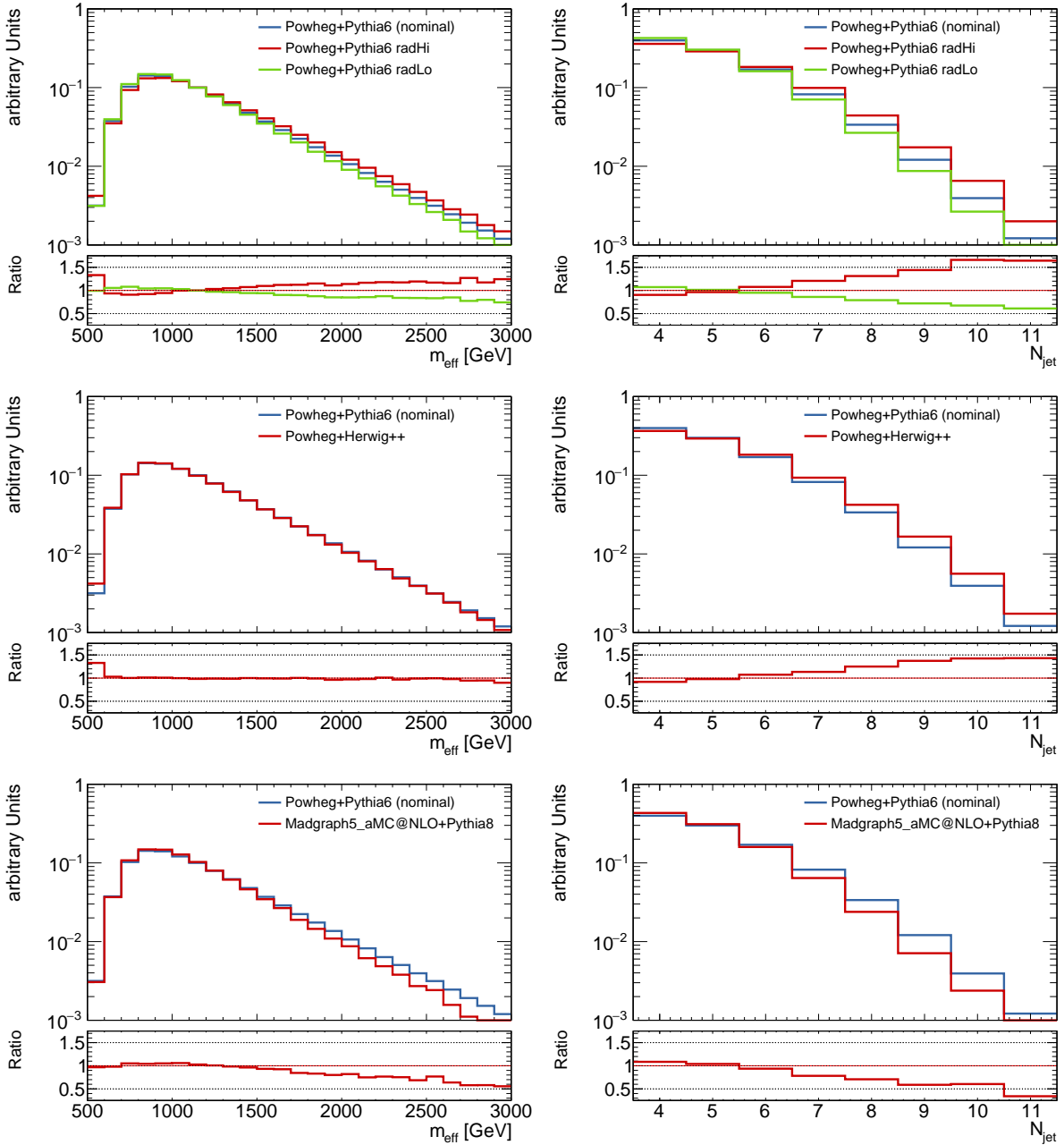


Figure 7.2: Theory variations for the  $t\bar{t}$  simulation for the  $m_{\text{eff}}$  (left) and the  $N_{\text{jet}}$  (right) distribution. The first row shows the impact of more (radHi) and less (radLo) QCD radiation, the second row the difference between PYTHIA6 and HERWIG++ as showering programs and the third row the difference between POWHEG-BOX and MADGRAPH5\_AMC@NLO for the matrix element generation. The impact of systematic variations on  $m_{\text{eff}}$  and  $N_{\text{jet}}$  is significant, but does not have a large impact on the analysis, since the  $t\bar{t}$  background is normalised in control regions with the same requirements on these quantities.

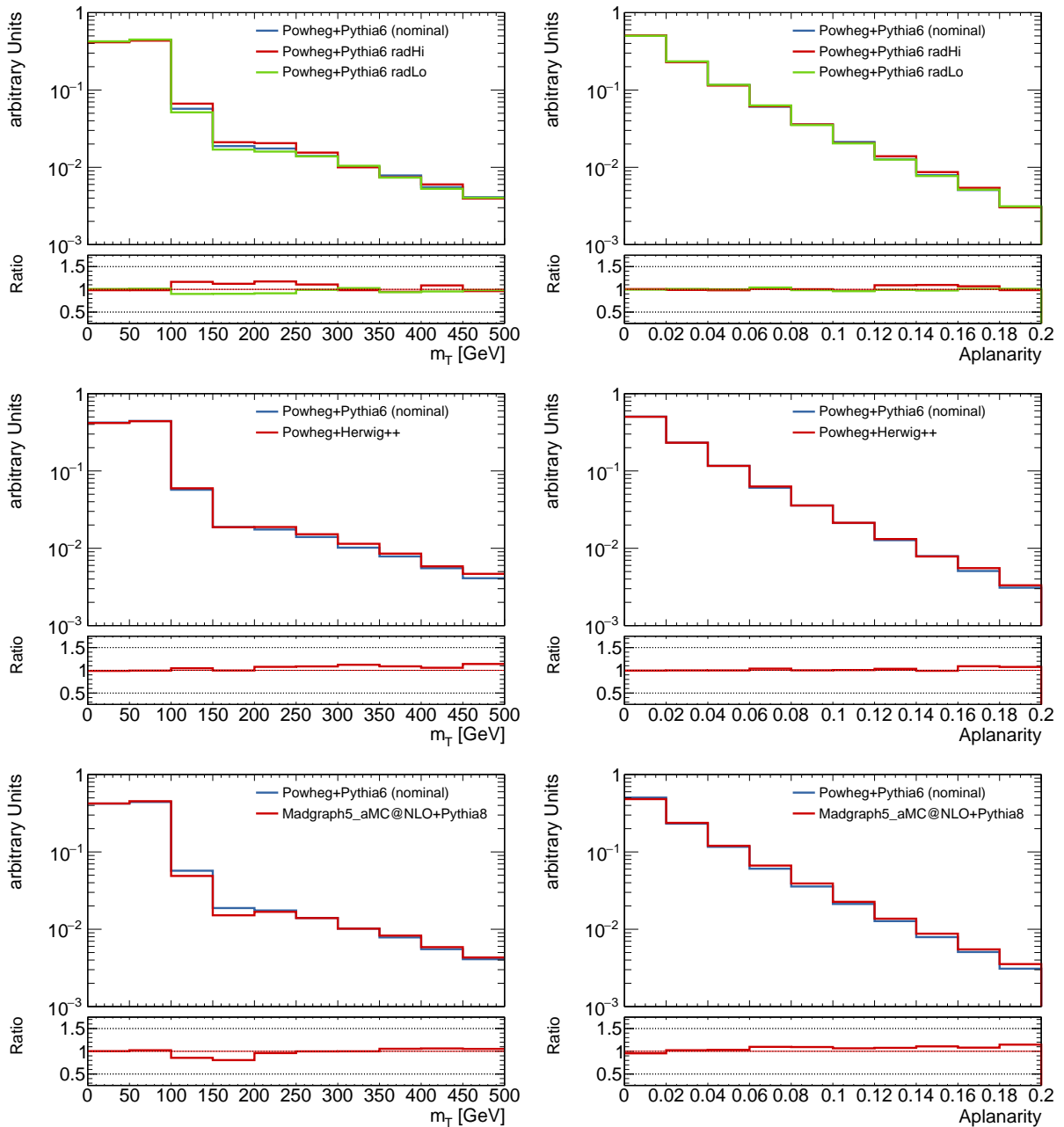
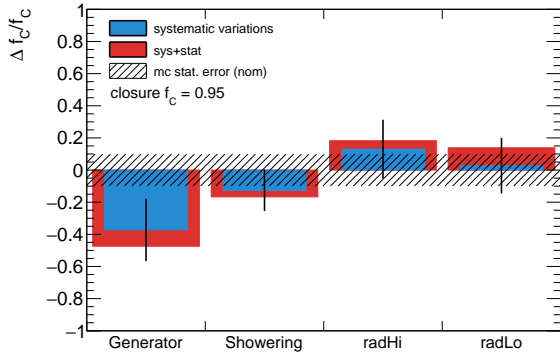
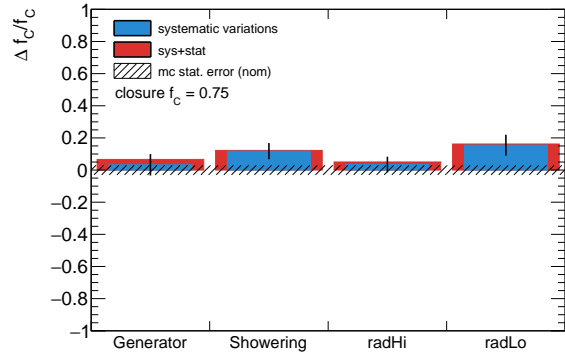


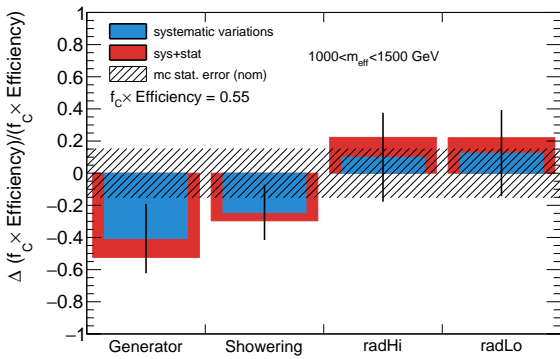
Figure 7.3: Theory variations for the  $t\bar{t}$  simulation for the  $m_T$  (left) and the Aplanarity (right) distribution which are used for most signal regions to extrapolate from control to signal regions. The first row shows the impact of more (radHi) and less (radLo) QCD radiation, the second row the difference between PYTHIA6 and HERWIG++ as showering programs and the third row the difference between POWHEG-BOX and MADGRAPH5\_AMC@NLO for the matrix element generation.



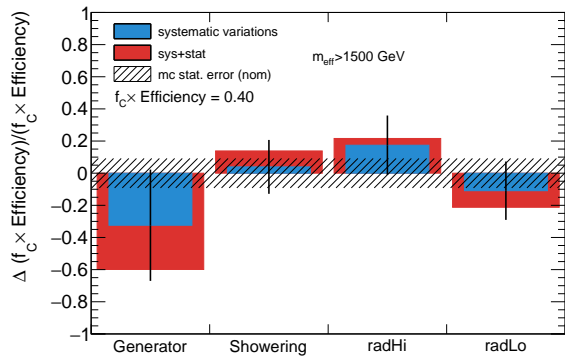
(a)  $f_{\text{Closure}}$  for the 9-jet SR



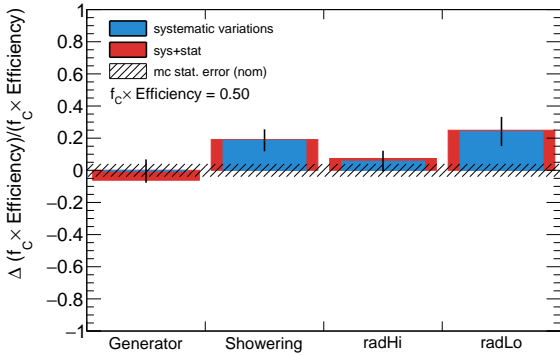
(b)  $f_{\text{Closure}}$  for VR  $m_T$



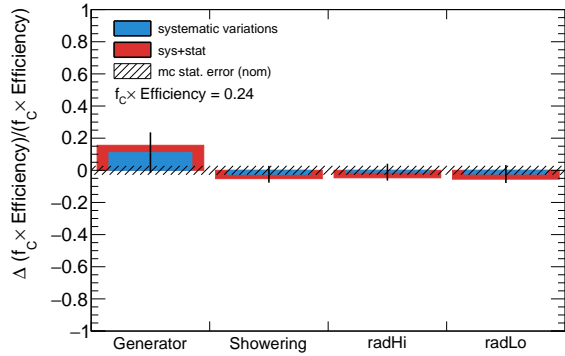
(c)  $f_{\text{Closure}} \cdot \epsilon_1$  for the 9-jet SR



(d)  $f_{\text{Closure}} \cdot \epsilon_2$  for the 9-jet SR



(e)  $f_{\text{Closure}} \cdot \epsilon_1$  for VR  $m_T$



(f)  $f_{\text{Closure}} \cdot \epsilon_2$  for VR  $m_T$

Figure 7.4: Variations for the  $t\bar{t}$  theory systematics in the 9-jet signal region and VR  $m_T$ . The first row shows the variations propagated on  $f_{\text{Closure}}$ , the second row on  $f_{\text{Closure}} \cdot \epsilon_i$ , where  $\epsilon_i$  corresponds to the efficiency of the first or second  $m_{\text{eff}}$  bin. The blue bars correspond to the absolute difference, the uncertainty bars on the blue bars to the MC statistical uncertainty and the red bars to the sum in quadrature of the variation and the statistical uncertainty.

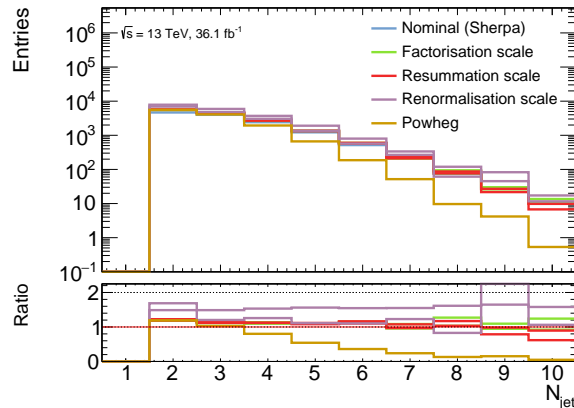


Figure 7.5: Theory systematic variations for the  $N_{\text{jet}}$  distribution for the diboson sample. The largest difference is given by the comparison between SHERPA and POWHEG-BOX

### 7.2.4 Cross section uncertainties

Uncertainties on the total cross section affect the predicted number of events for samples that are not normalised to data in control regions. In this analysis, they are much smaller than the variations discussed above.

The uncertainty on the total signal cross section is not included in the statistical model a priori. Instead, the results will be given in terms of the nominal signal rate and the  $\pm 1\sigma$  variations of the total cross section uncertainty.

### 7.2.5 Impact on signal regions

Tables 7.3 and 7.4 show the impact on the total background predictions of the theory uncertainties of the different background samples for the 2-6-jet signal regions. In the b-tagged bins, where the top backgrounds have the largest contribution, the uncertainty on the  $t\bar{t}$  and single top processes dominate. In the b-veto bins, the uncertainty is dominated by the  $W$ +jets and diboson background. The total theory uncertainty on the background is around 10%-20%, depending on the signal region. In most cases it is of the same order as the statistical uncertainty.

Signal region	2J <i>b</i> -tag	2J <i>b</i> -veto	4J high-x <i>b</i> -tag	4J high-x <i>b</i> -veto
Total background expectation	55.07	39.95	57.03	52.23
Total statistical ( $\sqrt{N_{\text{exp}}}$ )	$\pm 7.42$	$\pm 6.32$	$\pm 7.55$	$\pm 7.23$
Total theory uncertainty	$\pm 3.83$ [6.9%]	$\pm 8.82$ [22.1%]	$\pm 5.12$ [9.0%]	$\pm 6.29$ [12.0%]
MC statistical uncertainty	$\pm 1.46$	$\pm 2.00$	$\pm 1.76$	$\pm 8.02$
$t\bar{t}$	$\pm 2.58$	$\pm 0.45$	$\pm 4.44$	$\pm 0.44$
Single top/ $Wt$	$\pm 2.15$	$\pm 0.38$	$\pm 2.34$	$\pm 0.34$
$W$ +jets	$\pm 1.11$	$\pm 4.27$	$\pm 0.43$	$\pm 3.85$
Diboson	$\pm 1.37$	$\pm 7.55$	$\pm 0.91$	$\pm 4.88$
$Z$ +jets	$\pm 0.50$	$\pm 1.52$	$\pm 0.07$	$\pm 0.76$

Table 7.3: Breakdown of the theory uncertainties on the total background in the **2J** and **4J high-x** signal regions. For background components that are normalised in control regions, the contribution of the uncertainty was evaluated on the transfer factor. The percentages show the size of the uncertainty relative to the total expected background.

Signal region	4J low-x <i>b</i> -tag	4J low-x <i>b</i> -veto	6J <i>b</i> -tag	6J <i>b</i> -veto
Total background expectation	35.20	19.08	28.49	9.90
Total statistical ( $\sqrt{N_{\text{exp}}}$ )	$\pm 5.93$	$\pm 4.37$	$\pm 5.34$	$\pm 3.15$
Total theory uncertainty	$\pm 5.77$ [16.4%]	$\pm 4.41$ [23.1%]	$\pm 2.81$ [9.9%]	$\pm 2.07$ [20.9%]
MC statistical uncertainty	$\pm 1.38$	$\pm 1.16$	$\pm 0.86$	$\pm 0.83$
$t\bar{t}$	$\pm 4.25$	$\pm 0.51$	$\pm 2.48$	$\pm 0.21$
Single top/ $Wt$	$\pm 3.68$	$\pm 0.68$	$\pm 1.12$	$\pm 0.18$
$W$ +jets	$\pm 0.99$	$\pm 2.88$	$\pm 0.27$	$\pm 0.80$
Diboson	$\pm 0.86$	$\pm 3.23$	$\pm 0.65$	$\pm 1.89$
$Z$ +jets	$\pm 0.03$	$\pm 0.07$	$\pm 0.03$	$\pm 0.12$

Table 7.4: Breakdown of the theory uncertainties on the total background in the **4J low-x** and **6J** signal regions. For background components that are normalised in control regions, the contribution of the uncertainty was evaluated on the transfer factor. The percentages show the size of the uncertainty relative to the total expected background.

# Chapter 8

## Results

### 8.1 Convention for uncertainties in tables and plots

Tables and plots in this chapter show uncertainties derived from the full statistical model using HistFitter [106]. When uncertainties *after fit* are shown, they are derived by standard error propagation from the covariance matrix determined in the fit. Uncertainties *before fit* are calculated only from the systematic and MC statistical uncertainties, where all parameters are assumed to be uncorrelated and the MC samples are normalised to cross section.

The compatibility of Data and the background prediction in a certain bin is described by the *pull*  $(N_{\text{obs}} - N_{\text{pred}})/\sigma_{\text{tot}}$ , where  $\sigma_{\text{tot}}$  includes the total uncertainty on the background prediction, as well as the variation expected from the 68% central confidence interval of a Poisson distribution,

$$\sigma_{\text{tot}} = \sqrt{\Delta b_{\text{fit}}^2 + \Delta b_{\text{Poisson}, N_{\text{pred}}}^2}.$$

For a positive excess, the pull approximates the significance of the discovery p-value. The actual discovery p-value will be evaluated separately by a hypothesis test for each discovery signal region.

### 8.2 Background fit

To derive background estimates in signal and validation regions, a fit to data that only includes the control regions and the parameters that describe the background is performed. Figure 8.1 shows the fitted normalisation parameters for the 2-6-jet control regions. The tendency for decreasing normalisation factors with increasing  $m_{\text{eff}}$  is a result of the mis-modelling in the tails of  $p_{\text{T}}$  spectra of the jets and the lepton (see Figure 6.2). The fit is effectively re-weighting the MC  $m_{\text{eff}}$  distribution to data. This is illustrated for the 6-jet control region as an example in Figure 8.2.

Bkg fit for 9-jet SR	CR A (low $m_T$ )		CR B (high $m_T$ )		CR C ( $\geq 9$ jets)		SR (inclusive)
	b veto	b tag	b veto	b tag	b veto	b tag	
Observed events	3157	4947	130	385	8	84	
Fitted bkg events	$3160 \pm 60$	$4950 \pm 70$	$130 \pm 11$	$385 \pm 20$	$8.0 \pm 2.0$	$84 \pm 9$	$7 \pm 4$
Fitted $W$ +jets events	$2280 \pm 190$	$550 \pm 90$	$49 \pm 24$	$12 \pm 6$	$1.3^{+2.2}_{-1.3}$	$0.6^{+1.1}_{-0.6}$	$0.03^{+0.06}_{-0.03}$
Fitted $t\bar{t}$ events	$440 \pm 70$	$3670 \pm 110$	$35 \pm 6$	$303 \pm 21$	$5.3 \pm 1.3$	$72 \pm 9$	$6 \pm 4$
Fitted Single top events	$98 \pm 16$	$577 \pm 19$	$7.4 \pm 1.5$	$40.3 \pm 3.4$	$0.68 \pm 0.20$	$7.4 \pm 1.5$	$0.7 \pm 0.6$
Fitted $t\bar{t} + V$ events	$6.8 \pm 3.5$	$55 \pm 27$	$1.9 \pm 1.0$	$21 \pm 10$	$0.10 \pm 0.07$	$1.7 \pm 1.0$	$0.30 \pm 0.17$
Fitted Diboson events	$270 \pm 150$	$80 \pm 40$	$33 \pm 19$	$8 \pm 5$	$0.34^{+0.35}_{-0.34}$	$1.8^{+1.9}_{-1.8}$	$0.15^{+0.16}_{-0.15}$
Fitted $Z$ +jets events	$67 \pm 34$	$21 \pm 11$	$3.2 \pm 1.7$	$0.9 \pm 0.5$	$0.25 \pm 0.22$	$0.21 \pm 0.11$	$0.008^{+0.011}_{-0.008}$
MC exp. SM events	$4400 \pm 500$	$5500 \pm 500$	$154 \pm 26$	$400 \pm 34$	$18 \pm 5$	$68 \pm 18$	$5.3 \pm 2.9$
MC exp. $W$ +jets events	$3400 \pm 400$	$830 \pm 130$	$72 \pm 9$	$17.7 \pm 2.5$	$13 \pm 4$	$6.3 \pm 2.1$	$0.27 \pm 0.24$
MC exp. $t\bar{t}$ events	$470 \pm 70$	$3900 \pm 400$	$36 \pm 6$	$312 \pm 26$	$3.9 \pm 1.3$	$52 \pm 13$	$4.1 \pm 2.8$
MC exp. Single top events	$104 \pm 17$	$610 \pm 50$	$7.6 \pm 1.5$	$41.4 \pm 2.9$	$0.49 \pm 0.19$	$5.3 \pm 2.0$	$0.5^{+0.5}_{-0.5}$
MC exp. $t\bar{t} + V$ events	$6.8 \pm 3.5$	$55 \pm 27$	$1.9 \pm 1.0$	$21 \pm 10$	$0.10 \pm 0.07$	$1.7 \pm 1.0$	$0.30 \pm 0.17$
MC exp. Diboson events	$270 \pm 150$	$80 \pm 50$	$33 \pm 19$	$8 \pm 5$	$0.34^{+0.35}_{-0.34}$	$1.8^{+1.9}_{-1.8}$	$0.15^{+0.16}_{-0.15}$
MC exp. $Z$ +jets events	$67 \pm 34$	$21 \pm 11$	$3.2 \pm 1.7$	$0.9 \pm 0.5$	$0.25 \pm 0.22$	$0.21 \pm 0.11$	$0.008^{+0.011}_{-0.008}$

Table 8.1: Background fit results for the control regions for the 9-jet signal region. The fitted event counts in the signal region correspond to values calculated from the parameters in the background fit. Nominal MC expectations (normalised to cross-sections) are given for comparison. Uncertainties on the fitted yields are symmetric by construction, where the negative uncertainty is truncated when reaching to zero event yield.

The normalisation factors for the fit in the control regions for the 9-jet signal region are shown in Figure 8.3. The tendency of decreasing normalisation factors for increasing number of jets for the  $W$ +jets background results from the overprediction of events in high jet multiplicities in the Sherpa  $W$ +jets samples (see Figure 6.5). This results in a low normalisation factor for the  $W$ +jets contribution in the 9-jet signal region with a large uncertainty. This has a small impact on the total background prediction, since the  $W$ +jets contribution in the 9-jet signal region is even when neglecting the normalisation factor only up to 5%. Including the  $W$ +jets normalisation parameters nevertheless improves the statistical model, since the  $W$ +jets contributions are significant in the control regions. The normalisation factors for the Top background are compatible with unity within the uncertainties, as a result of the good modelling of the  $m_T$  and  $N_{\text{jet}}$  shape in the  $t\bar{t}$  samples. The  $\mu_{A/B}$  parameters are also compatible with one for the  $W$ +jets background.

Table 8.1 shows the yields before and after the fit for the control regions and the integrated (both  $m_{\text{eff}}$  bins) signal region. Table 8.2 shows the impact of the total systematic uncertainties on the background yields after the fit.

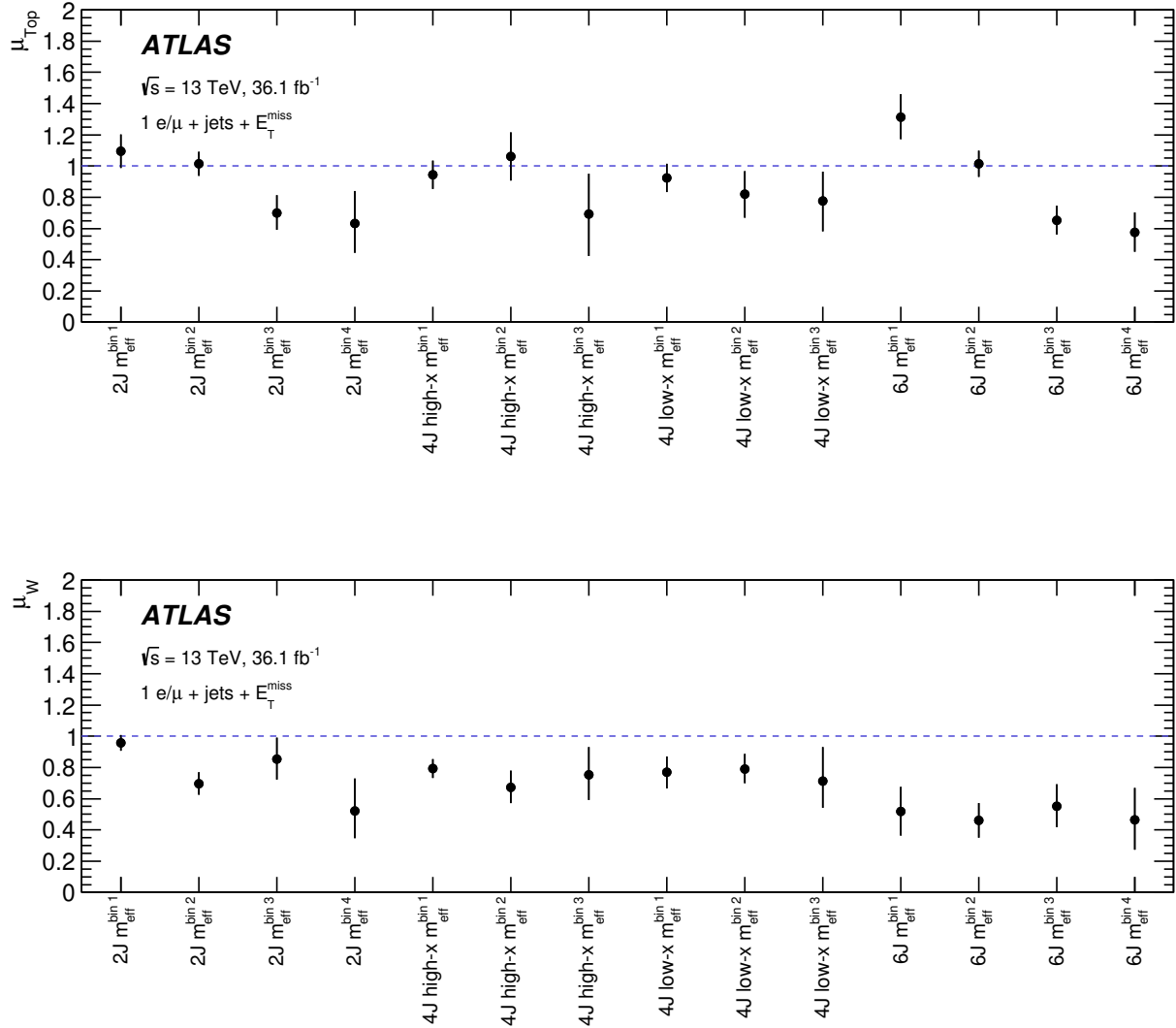


Figure 8.1: Fitted Normalisation factors for the 2-6-jet control regions for the Top (top) and  $W$ +jets (bottom) backgrounds (Figure from [57]).

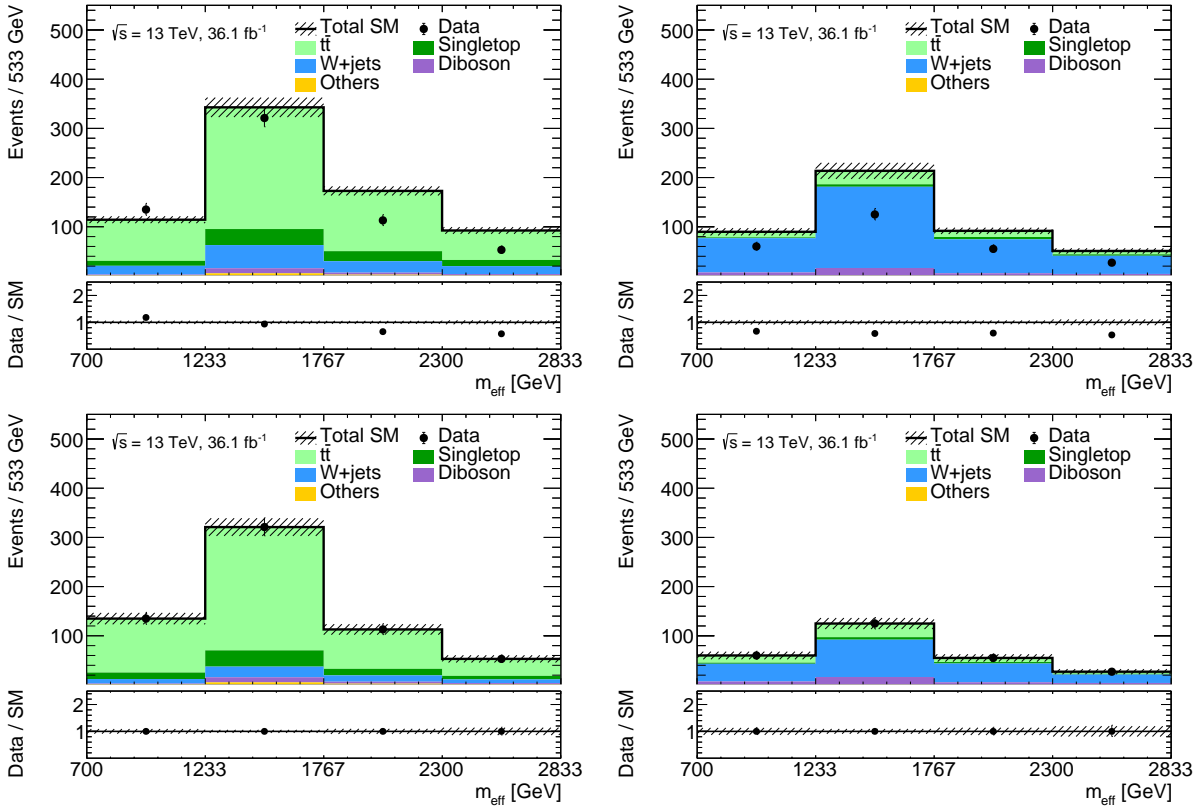


Figure 8.2: The **6J** control region before (top) and after the fit (bottom). The left hand side shows the b-tag category, enriched in the Top backgrounds and the right hand side the b-veto category, enriched in  $W$ +jets.

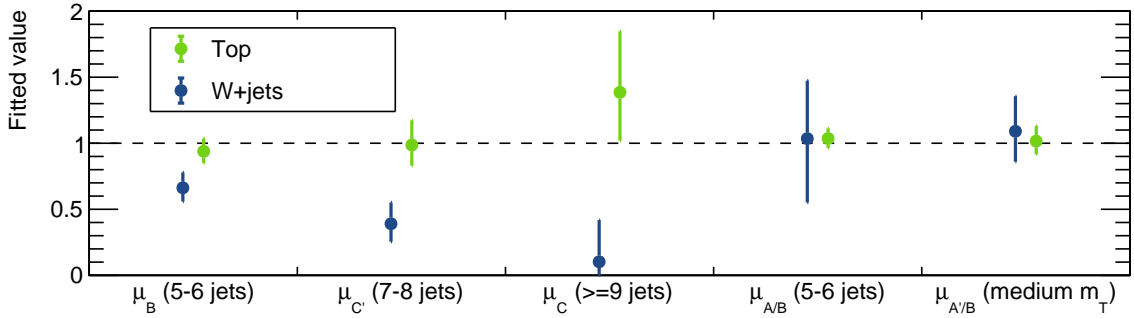


Figure 8.3: Fitted normalisation factors for the control regions for the 9-jet signal region. The parameters  $\mu_C$  and  $\mu_{A/B}$  are used to scale the signal region prediction. The parameters  $\mu_{C'}$  and  $\mu_{A'/B}$  are applied in the corresponding validation regions.  $\mu_B$  fixes the normalisation in the 5-6-jet control regions (also see Figure 6.13).

<b>Signal region</b>	<b>2J <math>b</math>-tag</b>	<b>2J <math>b</math>-veto</b>	<b>4J high-x <math>b</math>-tag</b>	<b>4J high-x <math>b</math>-veto</b>
Total background expectation	47	36	54	44
Total background syst. uncertainty	$\pm 4$ [9%]	$\pm 9$ [24%]	$\pm 7$ [12%]	$\pm 10$ [23%]
Experimental uncertainty	$\pm 1.3$	$\pm 2.2$	$\pm 2.6$	$\pm 5$
Normalisation uncertainty	$\pm 3.5$	$\pm 9$	$\pm 5$	$\pm 6$
Theoretical uncertainty	$\pm 1.6$	$\pm 8$	$\pm 2.3$	$\pm 5$
Statistical uncertainty of MC samples	$\pm 1.4$	$\pm 1.8$	$\pm 1.7$	$\pm 7$
<b>Signal region</b>	<b>4J low-x <math>b</math>-tag</b>	<b>4J low-x <math>b</math>-veto</b>	<b>6J <math>b</math>-tag</b>	<b>6J <math>b</math>-veto</b>
Total background expectation	31	16	27	7.3
Total background syst. uncertainty	$\pm 6$ [21%]	$\pm 4$ [25%]	$\pm 4$ [15%]	$\pm 2.0$ [27%]
Experimental uncertainty	$\pm 1.8$	$\pm 1.0$	$\pm 1.1$	$\pm 0.8$
Normalisation uncertainty	$\pm 2.3$	$\pm 0.8$	$\pm 1.4$	$\pm 0.5$
Theoretical uncertainty	$\pm 6$	$\pm 4$	$\pm 4$	$\pm 2.0$
Statistical uncertainty of MC samples	$\pm 1.2$	$\pm 1.0$	$\pm 0.9$	$\pm 0.6$
<b>Signal region</b>	<b>9J</b>			
Total background expectation	7			
Total background syst. uncertainty	$\pm 4$ [50%]			
Theoretical uncertainty	$\pm 4$			
Normalisation uncertainty	$\pm 2.0$			
Experimental uncertainty	$\pm 1.9$			
Statistical uncertainty of MC samples	$\pm 0.7$			

Table 8.2: Breakdown of the total systematic uncertainties in the background estimates after the fit. (Table adapted from [57], **9J** numbers contributed by the author)

### 8.3 Validation regions

To validate the extrapolation from MC, the fitted parameters from the background fit were propagated to the validation regions (as defined in Table 6.1 and 6.2). While most of the predicted background yields in the validation regions showed good compatibility with deviations below  $2\sigma$ , a deviation slightly above  $2\sigma$  is seen in the VR Aplanarity for the 4-jet high x signal region. Given the large number of validation regions, this is well compatible with a statistical fluctuation. No clear indications of a systematic effect were found in further studies. Nevertheless, since the validation region in question should validate the modelling of the Aplanarity shape, an uncertainty on the extrapolation over Aplanarity was introduced. The size of the uncertainty corresponds to the ratio between Data and MC for the efficiencies of the Aplanarity cut. The uncertainty is applied for the  $t\bar{t}$ , single top and  $W$ +jets backgrounds. For the 4-jet high x VR Aplanarity it amounts to 10%, for other region it ranges between 4% and 11%. After introducing this uncertainty, the pull in the region in question went down below  $2\sigma$ .

### 8.4 Signal regions

None of the signal regions shows a significant excess of data. Within the uncertainties the observations are compatible with the SM background. Figures 8.4-8.6 show the pulls in the signal regions, together with the corresponding validation regions. The absence of a significant excess is translated into model independent upper limits on the number of additional events in the discovery signal regions (see Table 8.3). The upper limits were derived in a simplified statistical model for each signal region separately. In this, the total uncertainty on the background prediction, as determined from the background fit, is described by one parameter. The number of potential signal events above the SM background is the second parameter and corresponds to the parameter of interest (POI). The limits correspond to the number of signal events above background at the 95% confidence level (CL), the value for which  $CL_s = 0.05$ . The p-value for rejecting the background hypothesis in favour of a positive signal is given as well. It is above 0.1 ( $\hat{=}$  below  $1.3\sigma$ ) for all discovery signal regions, giving no indication for a signal.

### 8.5 Interpretation

The absence of an excess of data is translated into limits on the model parameters of the signals considered. A combined fit in control and signal regions is performed for each signal model in the two-dimensional grids (see Section 3.2). The statistical model includes a potential signal contribution in all bins of all regions. Figure 8.7 shows the results. The fit in the 2-6-jet signal and control regions was interpreted in the squark and gluino one-step models, while the 9-jet signal and control region fit was used to derive limits for the

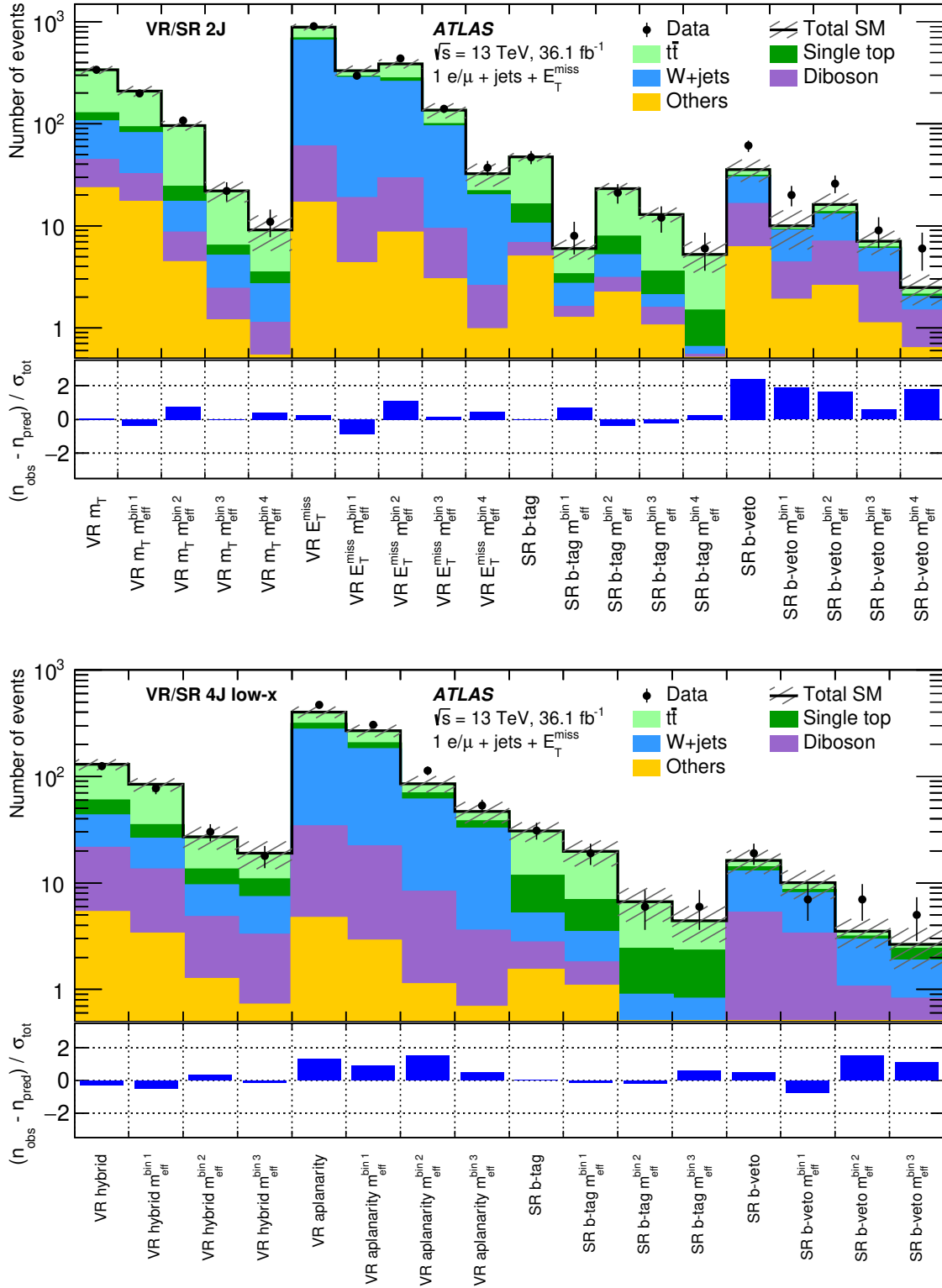


Figure 8.4: Comparison of the observed and expected event yields in the **2J** (top) and **4J low-x** (bottom) validation and signal regions. The validation regions are shown in the left and the signal regions in the right part of the plots, first the b-tag and then the b-veto categories. Both the integrated (sum of all bins) regions and the single  $m_{\text{eff}}$  bins are presented. (Figures from [57]).

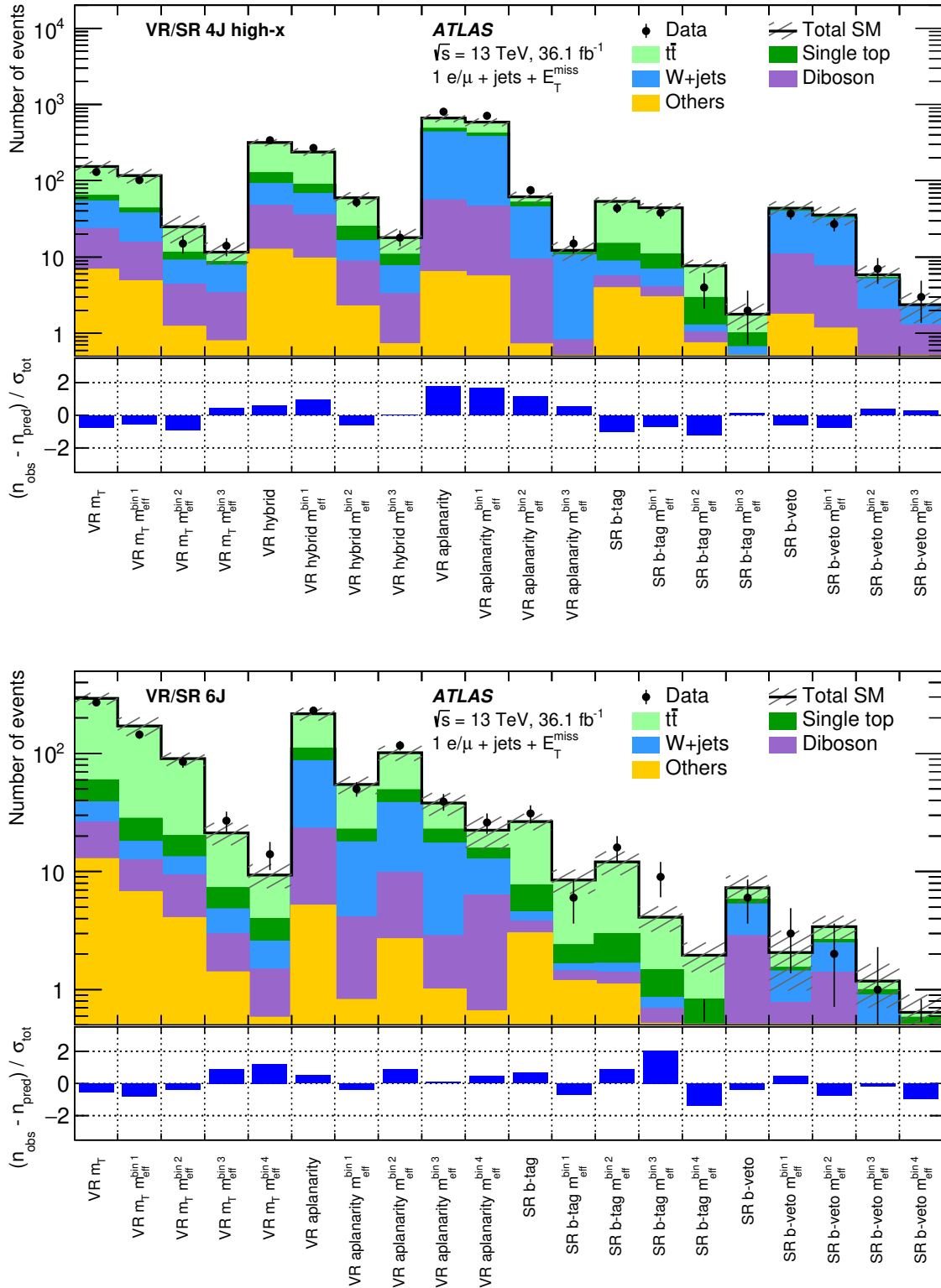


Figure 8.5: Comparison of the observed and expected event yields in the **4J high-x** (top) and **6J** (bottom) validation and signal regions. The validation regions are shown in the left and the signal regions in the right part of the plots, first the b-tag and then the b-veto categories. Both the integrated (sum of all bins) regions and the single  $m_{\text{eff}}$  bins are presented. (Figures from [57]).

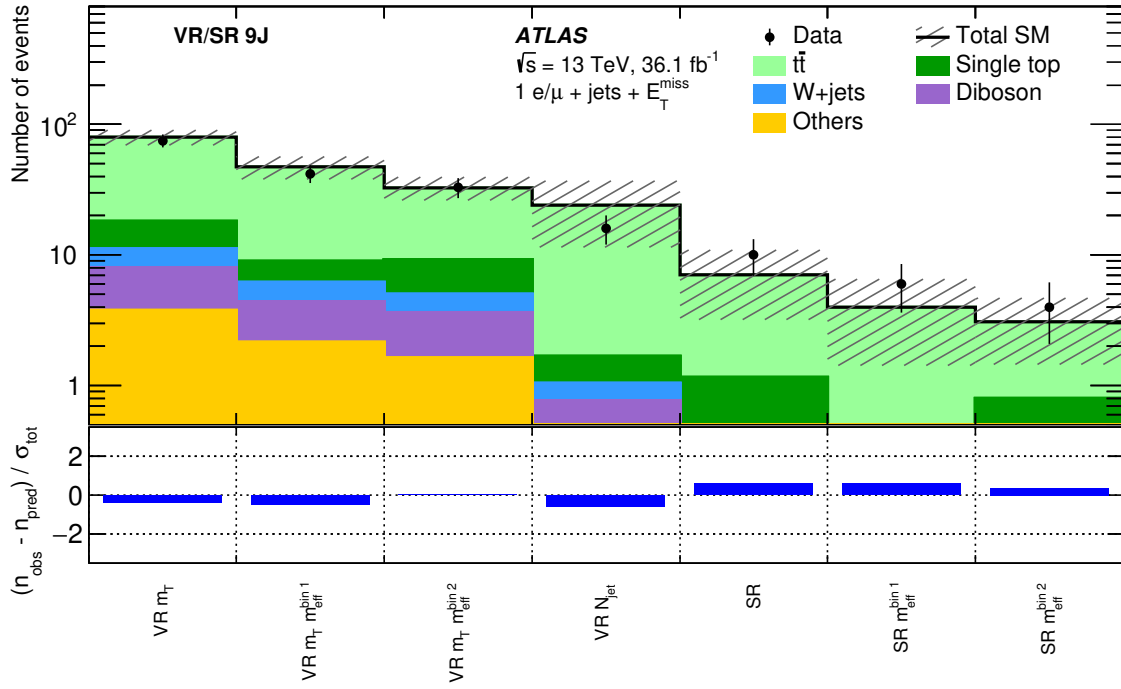


Figure 8.6: Comparison of the observed and expected event yields in the **9J** validation and signal regions. The validation regions are shown in the left and the signal regions in the right part of the plots. Both the integrated (sum of all bins) regions and the single  $m_{\text{eff}}$  bins are presented. (Figure contributed to [57] by the author).

$\mathbf{SR}_{\text{disc}}$	<b>2J</b>	<b>4J high-x</b>	<b>4J low-x</b> (gluino)	<b>4J low-x</b> (squark)	<b>6J</b> (gluino)	<b>6J</b> (squark)	<b>9J</b>
Observed events	80	16	24	50	0	28	4
Fitted bkg events	$67 \pm 6$	$17.7 \pm 2.7$	$17.2 \pm 3.2$	$47 \pm 7$	$2.6 \pm 0.6$	$23.4 \pm 3.1$	$3.1 \pm 1.6$
$\langle \epsilon \sigma \rangle_{\text{obs}}^{95}$ [fb]	0.92	0.27	0.50	0.62	0.08	0.46	0.20
$S_{\text{obs}}^{95}$	33.1	9.8	18.0	22.5	3.0	16.6	7.1
$S_{\text{exp}}^{95}$	$21.6^{+9.2}_{-5.6}$	$10.8^{+3.7}_{-3.0}$	$11.8^{+4.8}_{-2.7}$	$19.9^{+7.5}_{-5.6}$	$4.5^{+1.8}_{-1.0}$	$12.7^{+5.0}_{-4.0}$	$6.0^{+2.2}_{-1.2}$
$p(s = 0)$	0.10	0.50	0.10	0.35	0.50	0.21	0.34

Table 8.3: Model independent upper limits for the discovery signal regions. For each SR, the observed ( $S_{\text{obs}}^{95}$ ) and expected ( $S_{\text{exp}}^{95}$ ) upper limit at 95% CL on the number of signal events over SM background is given. The observed limit is also given in terms of the visible cross-section ( $\langle \epsilon \sigma \rangle_{\text{obs}}^{95}$ ), where  $\epsilon$  corresponds to the efficiency for the event selection of the corresponding signal region. The p-values for rejecting the background hypothesis in favour of a positive signal are given as well (capped at 0.5 if fewer events than the fitted background estimate are observed) (Table from [57], **9J** numbers contributed by the author).

gluino two-step and pMSSM models. The contour lines in the plots correspond to the model parameters for which  $CL_s = 0.05$ . Parameter values that lie inside the contour are excluded at the 95% CL. The dashed line corresponds to the expected limit for the Asimov data set (see Section 4.1) and the border of the expected  $\pm 1\sigma$  band to the model parameters where the  $\pm 1\sigma$  values of the expected  $CL_s$  value reached 0.05. The band indicates the range in which 68% of all derived limits would lie for repeated observations distributed according to the background only hypothesis. The observed limit is recalculated after varying the theoretical signal cross section up and down and shown as a red dashed line.

For one-step models with large mass splittings gluino masses are excluded up to 2.1 TeV and squark masses up to 1.25 TeV. The limits are weaker for very high  $x$  and low  $x$  scenarios as well as compressed spectra close to the diagonal line at  $m_{\tilde{g}} = m_{\tilde{\chi}_1^0}$  in the  $x = 1/2$  grids. For gluinos no limit can be given for an LSP mass above around 1 TeV and for squarks for an LSP mass above around 550 GeV. In the gluino two-step models, gluino masses are excluded up to 1.75 TeV for low LSP masses, while no limit can be given for LSP masses above 800 GeV. For the pMSSM models considered, gluino masses below 1650 GeV to 1700 GeV are excluded.

## 8.6 Discussion

The absence of signal increases the limit for SUSY particles substantially for the simplified models considered. Depending on the scenario, squark mass limits are pushed above 1 TeV

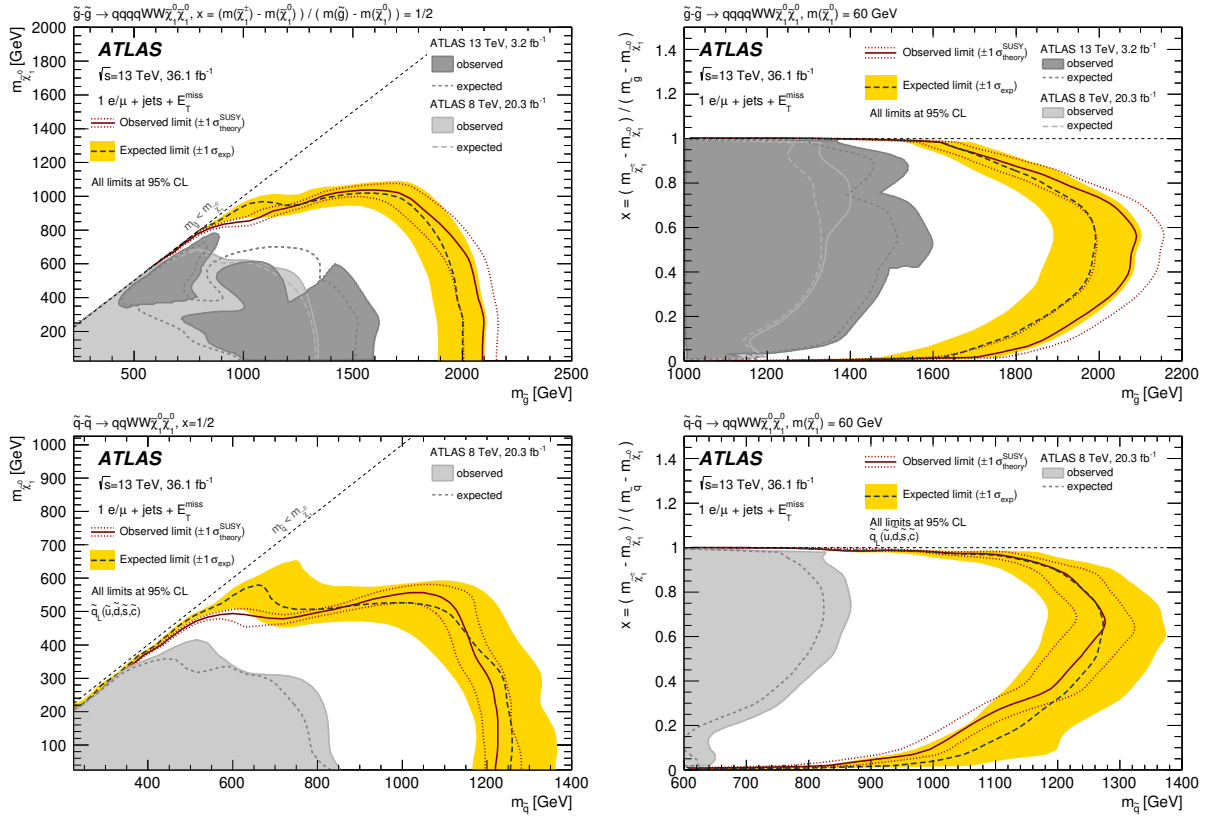


Figure 8.7: Exclusion contours in the gluino and squark one-step models, derived from the fit in the 2-6-jet control and signal regions. The top row shows the limits for the gluino, the bottom row for the squark models. The  $x = 1/2$  grids are shown on the left and the variable  $x$  grids on the right. For reference, exclusion bounds from previous searches with  $20.3 \text{ fb}^{-1}$  at 8 TeV centre-of-mass energy [126] and  $3.2 \text{ fb}^{-1}$  at 13 TeV centre-of-mass energy [110] are overlaid where applicable by the gray area (the observed limit is shown by the solid line, while the dashed line shows the expected limit). (Figures from [57])

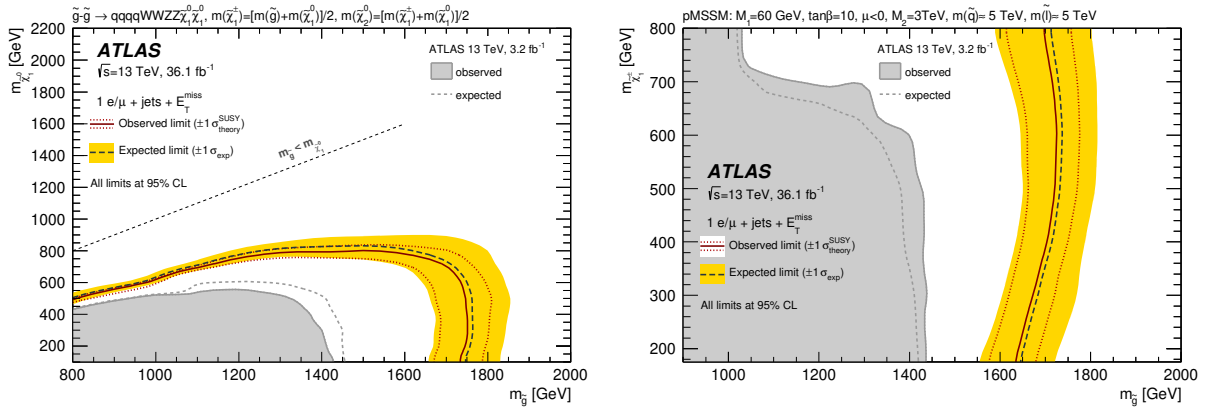


Figure 8.8: Exclusion contours in the gluino 2-step (left) and pMSSM (right) models, derived from the fit in the 9-jet control and signal regions. For reference, exclusion bounds from previous searches with  $3.2 \text{ fb}^{-1}$  at 13 TeV centre-of-mass energy [127] are overlaid by the gray area (the observed limit is shown by the solid line, while the dashed line shows the expected limit) (Figures contributed to [57] by the author).

and gluino limits above 2 TeV. The hypothesis of SUSY at the TeV scale is challenged more and more by the experimental data. Other searches at ATLAS and CMS reach similar conclusions. No striking hints of new physics beyond the SM were observed with the LHC data so far.

Several other searches consider similar models in different decay channels. Figure 8.9 shows a comparison of gluino mass limits at ATLAS, including the ones presented in this thesis. The one-step simplified models are also used in an interpretation by the ATLAS search without leptons. The latest preliminary results [128] lead to similar results for low LSP masses, while the analysis presented in this thesis sets slightly stricter limits for scenarios with higher LSP masses. The other models considered by the zero lepton search are characterised by the absence of leptons or by the presence of  $Z$  instead of  $W$  bosons. Most of the limits in these models also reach the TeV scale for squarks, in one scenario up to 1.58 TeV and  $\approx 2 \text{ TeV}$  for the gluino models.

The gluino two-step models are also used in an interpretation by the ATLAS zero lepton multijet search [36] and the same-sign/3-lepton search [129]. These two searches and the one lepton analysis in the 9-jet signal region presented in this thesis have partly complementary sensitivity. While the same-sign/3-lepton analysis sets the strictest limits towards the compressed region, the analysis of this thesis and the zero lepton multijet search result in stricter limits for the low LSP scenarios.

A one-lepton search at CMS [130] also interprets the results in the gluino one-step  $x = 1/2$  models. The limits are comparable, but slightly lower than the ones presented in this thesis. The results of the CMS analysis with two same-sign leptons [131] are interpreted both in the gluino one-step  $x = 1/2$  models, and in another grid with a fixed low mass difference

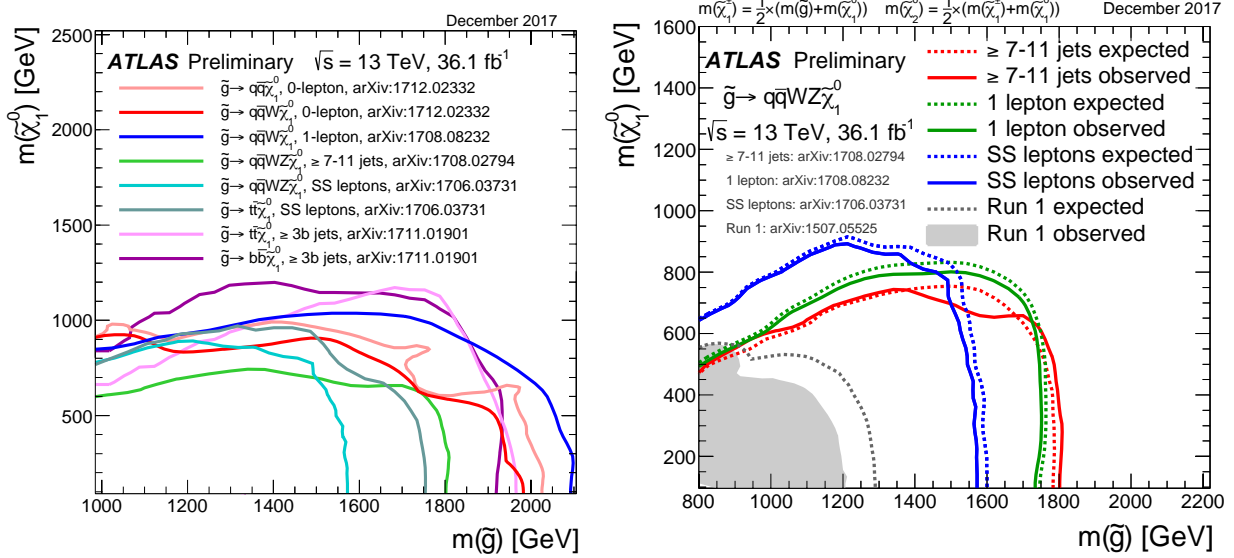


Figure 8.9: Summary plots for ATLAS limits on gluino masses [132]. The limit on gluino masses in the one-step models derived from the 2-6-jet signal regions described in this thesis is shown in the left plot by the blue line. The limit on gluino masses in the two-step models as derived from the 9-jet signal region is shown on the right plot by the green lines.

between the chargino and the LSP of 20 GeV. For low LSP masses, those limits can be compared to the very low  $x$  models in the variable  $x$  grid considered in this thesis. The high LSP mass case can be compared to the compressed region close to the  $m_{\tilde{g}} = m_{\tilde{\chi}_1^0}$  diagonal in the  $x = 1/2$  grid. The limits for the gluino one-step models are generally weaker for the same-sign analysis (up to 1.4 TeV) than for the one lepton analysis.



# Chapter 9

## Summary and Outlook

In this thesis a search for strongly produced supersymmetric particles in events with one isolated lepton, missing transverse momentum and multiple jets with ATLAS data was presented. The search is performed inclusively, meaning both final states with and without b-tagged jets are considered. The targeted signal models are different scenarios for decays of superpartners of the first and second generation quarks and the gluons. In 2015, the first year of the LHC Run 2, a boost in sensitivity towards higher masses for particles beyond the SM was expected due to the increased centre of mass energy. In order to analyse the new data quickly, an optimisation procedure was carried out to find the best search regions for several distinct models of gluino decays. Based on this search, the analysis was refined to a more sophisticated setup that was used to analyse the full 2015 and 2016 data of  $36.1 \text{ fb}^{-1}$ . The strategy is based on different signal categories, mainly defined by the jet multiplicity and several other selection criteria that define the targeted scenarios for the corresponding signal regions. The minimum requirement on the jet multiplicity ranges from 2 to 6 jets, where the 2-jet signal region selects soft leptons with  $p_T < 35 \text{ GeV}$  and the 4-6-jet signal regions select hard leptons with  $p_T > 35 \text{ GeV}$ . All regions are designed to have no overlap, so a simultaneous fit can be used for the statistical evaluation that uses the binned effective mass distribution in each signal region that is further split into a category requiring no and at least one b-tagged jet.

As part of this thesis, the search was extended by a 9-jet signal region that targets scenarios with longer decay chains. A data-driven background estimation technique, based on the invariance of the transverse mass shape in different number of jet events, has been developed to achieve a reliable prediction of the SM background in 9-jet events.

No significant excess was found in any of the search regions. Therefore, limits on the model parameters are derived. The 2-6-jet signal regions are interpreted in simplified models of gluino and squark decays via an intermediate chargino that decays into a  $W$  boson and the LSP. For low LSP masses, the limits reach up to 2.1 TeV for gluinos and 1.25 TeV for squarks. The 9-jet signal region is interpreted in models with a higher number of particles in the final state, namely gluino decays via two steps with a  $W$  and a  $Z$  boson

and a subset of the pMSSM, characterised by gluino decays into top or bottom quarks and a neutralino or chargino from a higgsino multiplet and finally into the LSP. Limits on the two-step model parameters reach up to 1.75 TeV for the low LSP scenario and limits in the pMSSM models exclude gluino masses below 1.65 TeV to 1.7 TeV.

These results, together with the results of other searches at the LHC severely challenge the assumption of SUSY at the TeV scale. Although it could be that all superpartners are just too heavy to influence the physics seen at the LHC, there is still hope that signals could show up with future LHC data. Signals could be hidden due to compressed spectra where the current limits are weaker. Furthermore, the simplified models assume 100% branching fraction, so the complete picture is only given by the full set of searches in different final states, where the limits assuming 100% branching fraction could be substantially weakened when considering the decay to different, potentially difficult final states. Another possibility is that strongly interacting particles are out of the reach of the LHC while electroweakly interacting particles are light enough. In that case, there could be a chance to see indications for electroweakly interacting particles that are produced with much lower cross sections in the coming years when more data is available. Searches for these scenarios will be one of the focuses of the coming years. Furthermore, many parameters connected to the observed Higgs boson at 125 GeV are still to be measured and deviations from the SM could hint to an extended Higgs sector, as in the MSSM. There is also still the possibility for additional Higgs bosons to be discovered. Until the end of Run 2 in 2018, an integrated luminosity of  $120 \text{ fb}^{-1}$  is planned. Afterwards, the LHC is planned to be upgraded to run at 14 TeV and run until 2023 while collecting  $300 \text{ fb}^{-1}$  of data in total [133], 10 times more than the data set analysed in this thesis. After 2023 an upgrade to even higher luminosity (high luminosity LHC) is planned where the total integrated luminosity is expected to reach  $3000 \text{ fb}^{-1}$ . With more data also the reach in mass is expected to increase significantly. The expected exclusion limit could reach as far as 2 TeV for squarks and 3 TeV for gluinos with  $3000 \text{ fb}^{-1}$  of data [134]. In this sense only around 1% of the total LHC data that is expected to come has been analysed so far, leaving a large potential for surprises.

# Bibliography

- [1] S. L. Glashow, “Partial-symmetries of weak interactions,” *Nuclear Physics* **22** no. 4, (1961) 579 – 588.
- [2] S. Weinberg, “A model of leptons,” *Phys. Rev. Lett.* **19** (Nov, 1967) 1264–1266.
- [3] A. Salam and J. C. Ward, “Weak and electromagnetic interactions,” *Il Nuovo Cimento (1955-1965)* **11** no. 4, (Feb, 1959) 568–577.
- [4] M. E. Peskin and D. V. Schroeder, *An Introduction To Quantum Field Theory*. Westview Press, 1995.
- [5] F. Englert and R. Brout, “Broken Symmetry and the Mass of Gauge Vector Mesons,” *Physical Review Letters* **13** (Aug., 1964) 321–323.
- [6] P. W. Higgs, “Broken Symmetries and the Masses of Gauge Bosons,” *Physical Review Letters* **13** (Oct., 1964) 508–509.
- [7] G. S. Guralnik, C. R. Hagen, and T. W. Kibble, “Global Conservation Laws and Massless Particles,” *Physical Review Letters* **13** (Nov., 1964) 585–587.
- [8] **ATLAS** Collaboration, “Observation of a new particle in the search for the Standard Model Higgs boson with the ATLAS detector at the LHC,” *Phys. Lett. B* **716** (Aug, 2012) 1–29. 39 p, [arXiv:1207.7214](https://arxiv.org/abs/1207.7214) [hep-ex]. <https://cds.cern.ch/record/1471031>.
- [9] **CMS** Collaboration, “Observation of a new boson at a mass of 125 GeV with the CMS experiment at the LHC,” *Phys. Lett. B* **716** (Jul, 2012) 30–61. 32 p, [arXiv:1207.7235](https://arxiv.org/abs/1207.7235) [hep-ex]. <http://cds.cern.ch/record/1471016>.
- [10] **Particle Data Group** Collaboration, C. Patrignani *et al.*, “Review of Particle Physics,” *Chin. Phys.* **C40** no. 10, (2016) 100001. <http://pdg.lbl.gov>.
- [11] M. Kobayashi and T. Maskawa, “CP-Violation in the Renormalizable Theory of Weak Interaction,” *Progress of Theoretical Physics* **49** no. 2, (1973) 652–657.

- [12] B. T. Cleveland, T. Daily, J. Raymond Davis, J. R. Distel, K. Lande, C. K. Lee, P. S. Wildenhain, and J. Ullman, “Measurement of the Solar Electron Neutrino Flux with the Homestake Chlorine Detector,” *The Astrophysical Journal* **496** no. 1, (1998) 505.
- [13] Z. Maki, M. Nakagawa, and S. Sakata, “Remarks on the unified model of elementary particles,” *Progress of Theoretical Physics* **28** no. 5, (1962) 870–880.
- [14] G. Hooft, “Renormalizable Lagrangians for massive Yang-Mills fields,” *Nuclear Physics B* **35** no. 1, (1971) 167 – 188.
- [15] G. ’t Hooft and M. Veltman, “Regularization and renormalization of gauge fields,” *Nuclear Physics B* **44** no. 1, (1972) 189 – 213.
- [16] T. Kinoshita, “Mass singularities of feynman amplitudes,” *Journal of Mathematical Physics* **3** no. 4, (1962) 650–677.
- [17] T. D. Lee and M. Nauenberg, “Degenerate systems and mass singularities,” *Phys. Rev.* **133** (Mar, 1964) B1549–B1562.
- [18] E. Noether, “Invariante Variationsprobleme,” *Nachr. D. König. Gesellsch. D. Wiss. Zu Göttingen, Math-phys. Klasse 1918: 235-257* (1918) 57, [arXiv:physics/0503066](https://arxiv.org/abs/physics/0503066).
- [19] S. P. Martin, “A Supersymmetry primer,” *Adv. Ser. Direct. High Energy Phys* **21** (2010) 1–153, [arXiv:hep-ph/9709356](https://arxiv.org/abs/hep-ph/9709356) [hep-ph].
- [20] V. C. Rubin and W. K. Ford, Jr., “Rotation of the Andromeda Nebula from a Spectroscopic Survey of Emission Regions,” *The Astrophysical Journal* **159** (Feb., 1970) 379.
- [21] F. Zwicky, “Die Rotverschiebung von extragalaktischen Nebeln,” *Helvetica Physica Acta* **6** (1933) 110–127.
- [22] D. Clowe, M. Bradač, A. H. Gonzalez, M. Markevitch, S. W. Randall, C. Jones, and D. Zaritsky, “A direct empirical proof of the existence of dark matter,” *The Astrophysical Journal Letters* **648** no. 2, (2006) L109.
- [23] **Planck** Collaboration, “Planck 2015 results. XIII. Cosmological parameters,” *Astron. Astrophys.* **594** (2016) A13, [arXiv:1502.01589](https://arxiv.org/abs/1502.01589) [astro-ph.CO].
- [24] S. Pokorski, K. Rolbiecki, and K. Sakurai, “Proton decay testing low energy SUSY,” [arXiv:1707.06720](https://arxiv.org/abs/1707.06720) [hep-ph].

- [25] H. Baer and X. Tata, *Weak scale supersymmetry: From superfields to scattering events*. Cambridge University Press, 2006.
- [26] **Super-Kamiokande** Collaboration, “Search for proton decay via  $p \rightarrow e^+\pi^0$  and  $p \rightarrow \mu^+\pi^0$  in 0.31 megaton·years exposure of the Super-Kamiokande water Cherenkov detector,” *Physical Review D* **95** no. 1, (2017) 012004, [arXiv:1610.03597 \[hep-ex\]](#).
- [27] W. Beenakker, R. Hopker, M. Spira, and P. Zerwas, “Squark and gluino production at hadron colliders,” *Nucl. Phys. B* **492** (1997) 51–103, [arXiv:hep-ph/9610490](#).
- [28] A. Kulesza and L. Motyka, “Threshold resummation for squark-antisquark and gluino-pair production at the LHC,” *Phys.Rev.Lett.* **102** (2009) 111802, [arXiv:0807.2405 \[hep-ph\]](#).
- [29] A. Kulesza and L. Motyka, “Soft gluon resummation for the production of gluino-gluino and squark-antisquark pairs at the LHC,” *Phys. Rev. D* **80** (2009) 095004, [arXiv:0905.4749 \[hep-ph\]](#).
- [30] W. Beenakker, S. Brensing, M. Kramer, A. Kulesza, E. Laenen, *et al.*, “Soft-gluon resummation for squark and gluino hadroproduction,” *JHEP* **12** (2009) 041, [arXiv:0909.4418 \[hep-ph\]](#).
- [31] W. Beenakker *et al.*, “Squark and gluino hadroproduction,” *Int.J.Mod.Phys. A* **26** (2011) 2637–2664, [arXiv:1105.1110 \[hep-ph\]](#).
- [32] C. Borschensky, M. Krämer, A. Kulesza, M. Mangano, S. Padhi, T. Plehn, and X. Portell, “Squark and gluino production cross sections in pp collisions at  $\sqrt{s} = 13, 14, 33$  and 100 TeV,” *Eur. Phys. J. C* **74** no. 12, (2014) 3174, [arXiv:1407.5066 \[hep-ph\]](#).
- [33] J. Alwall, P. Schuster, and N. Toro, “Simplified Models for a First Characterization of New Physics at the LHC,” *Phys. Rev. D* **79** (2009) 075020, [arXiv:0810.3921 \[hep-ph\]](#).
- [34] D. Alves *et al.*, “Simplified Models for LHC New Physics Searches,” *J. Phys. G: Nucl. Part. Phys.* **39** (2012) 105005, [arXiv:1105.2838 \[hep-ph\]](#).
- [35] **MSSM Working Group** Collaboration, A. Djouadi *et al.*, “The Minimal supersymmetric standard model: Group summary report,” in *GDR (Groupement De Recherche) - Supersymetrie Montpellier, France, April 15-17, 1998*. 1998. [arXiv:hep-ph/9901246 \[hep-ph\]](#).

- [36] **ATLAS** Collaboration, “Search for new phenomena with large jet multiplicities and missing transverse momentum using large-radius jets and flavour-tagging at ATLAS in 13 TeV  $pp$  collisions,” [arXiv:1708.02794 \[hep-ex\]](#).
- [37] **ATLAS** Collaboration, “Summary of the ATLAS experiment’s sensitivity to supersymmetry after LHC Run 1 — interpreted in the phenomenological MSSM,” *JHEP* **10** (2015) 134, [arXiv:1508.06608 \[hep-ex\]](#).
- [38] B. C. Allanach, “SOFTSUSY: a program for calculating supersymmetric spectra,” *Comput. Phys. Commun.* **143** (2002) 305, [arXiv:hep-ph/0104145](#).
- [39] A. Djouadi, M. Mühlleitner, and M. Spira, “Decays of supersymmetric particles: The Program SUSY-HIT (SUSpect-SdecaY-Hdecay-InTerface),” *Acta Phys. Polon. B* **38** (2007) 635, [arXiv:hep-ph/0609292](#).
- [40] A. Buckley, “PySLHA: a Pythonic interface to SUSY Les Houches Accord data,” *Eur. Phys. J. C* **75** no. 10, (2015) 467, [arXiv:1305.4194 \[hep-ph\]](#).
- [41] LEP2 SUSY Working Group. Notes LEPSUSYWG/02-04.1 and LEPSUSYWG/01-03.1 <http://lepsusy.web.cern.ch/lepsusy>. Accessed: 19-10-2017.
- [42] “CMS Supersymmetry Publications.” <http://cms-results.web.cern.ch/cms-results/public-results/publications/SUS/index.html>. Accessed: 05-09-2017.
- [43] “Summary plots from the ATLAS Supersymmetry physics group.” <https://atlas.web.cern.ch/Atlas/GROUPS/PHYSICS/CombinedSummaryPlots/SUSY/index.html>. Accessed: 05-09-2017.
- [44] A. Buckley, J. Butterworth, S. Gieseke, D. Grellscheid, S. Höche, H. Hoeth, F. Krauss, L. Lönnblad, E. Nurse, P. Richardson, *et al.*, “General-purpose event generators for LHC physics,” *Physics Reports* **504** no. 5, (2011) 145–233.
- [45] **NNPDF** Collaboration, R. D. Ball *et al.*, “Parton distributions for the LHC Run II,” *JHEP* **04** (2015) 040, [arXiv:1410.8849 \[hep-ph\]](#).
- [46] A. D. Martin, W. J. Stirling, R. S. Thorne, and G. Wat, “Parton distributions for the LHC,” *Eur. Phys. J. C* **63** (2009) 189, [arXiv:0901.0002 \[hep-ph\]](#).
- [47] H.-L. Lai, M. Guzzi, J. Huston, Z. Li, P. M. Nadolsky, J. Pumplin, and C. P. Yuan, “New parton distributions for collider physics,” *Phys. Rev. D* **82** (2010) 074024, [arXiv:1007.2241 \[hep-ph\]](#).

- [48] T. Gleisberg, S. Höche, F. Krauss, M. Schönherr, S. Schumann, *et al.*, “Event generation with SHERPA 1.1,” *JHEP* **02** (2009) 007, [arXiv:0811.4622 \[hep-ph\]](#).
- [49] L. Evans and P. Bryant, “LHC Machine,” *Journal of Instrumentation* **3** no. 08, (2008) S08001.
- [50] E. A. Mobs, “The CERN accelerator complex,” Oct, 2016. <https://cds.cern.ch/record/2225847>. General Photo.
- [51] **ATLAS** Collaboration, “The ATLAS Experiment at the CERN Large Hadron Collider,” *JINST* **3** (2008) S08003.
- [52] F. Pastore, “ATLAS Run-2 status and performance,” Tech. Rep. ATL-GEN-PROC-2015-001, CERN, Geneva, Sep, 2015. <http://cds.cern.ch/record/2048973>.
- [53] **ATLAS** Collaboration, M. Capeans, G. Darbo, K. Einsweiler, M. Elsing, T. Flick, M. Garcia-Sciveres, C. Gemme, H. Pernegger, O. Rohne, and R. Vuillermet, “ATLAS Insertable B-Layer Technical Design Report,” Tech. Rep. CERN-LHCC-2010-013. ATLAS-TDR-19, Sep, 2010. <http://cds.cern.ch/record/1291633>.
- [54] **ATLAS** Collaboration, “Performance of the ATLAS Trigger System in 2015,” *Eur. Phys. J.* **C77** no. 5, (2017) 317, [arXiv:1611.09661 \[hep-ex\]](#).
- [55] **ATLAS TDAQ** Collaboration, “The ATLAS Data Acquisition and High Level Trigger system,” *Journal of Instrumentation* **11** no. 06, (2016) P06008.
- [56] “ATLAS Luminosity public results.” <https://twiki.cern.ch/twiki/bin/view/AtlasPublic/LuminosityPublicResultsRun2>. Accessed: 03-10-2017.
- [57] **ATLAS** Collaboration, “Search for squarks and gluinos in events with an isolated lepton, jets, and missing transverse momentum at  $\sqrt{s} = 13$  TeV with the ATLAS detector,” *Phys. Rev.* **D96** no. 11, (2017) 112010, [arXiv:1708.08232 \[hep-ex\]](#).
- [58] **ATLAS** Collaboration, “Multi-Boson Simulation for 13 TeV ATLAS Analyses.” ATL-PHYS-PUB-2017-005, 2017. <https://cds.cern.ch/record/2261933>.
- [59] **ATLAS** Collaboration, “ATLAS simulation of boson plus jets processes in Run 2.” ATL-PHYS-PUB-2017-006, 2017. <https://cds.cern.ch/record/2261937>.
- [60] **ATLAS** Collaboration, “Simulation of top-quark production for the ATLAS experiment at  $\sqrt{s} = 13$  TeV.” ATL-PHYS-PUB-2016-004, 2016. <https://cds.cern.ch/record/2120417>.

- [61] **ATLAS** Collaboration, “Modelling of the  $t\bar{t}H$  and  $t\bar{t}V(V = W, Z)$  processes for  $\sqrt{s} = 13$  TeV ATLAS analyses.” ATL-PHYS-PUB-2016-005, 2016. <https://cds.cern.ch/record/2120826>.
- [62] S. Alioli, P. Nason, C. Oleari, and E. Re, “A general framework for implementing NLO calculations in shower Monte Carlo programs: the POWHEG BOX,” *JHEP* **06** (2010) 043, [arXiv:1002.2581](https://arxiv.org/abs/1002.2581) [hep-ph].
- [63] S. Frixione, P. Nason, and C. Oleari, “Matching NLO QCD computations with Parton Shower simulations: the POWHEG method,” *JHEP* **11** (2007) 070, [arXiv:0709.2092](https://arxiv.org/abs/0709.2092) [hep-ph].
- [64] T. Sjöstrand, S. Mrenna, and P. Z. Skands, “PYTHIA 6.4 Physics and Manual,” *JHEP* **05** (2006) 026, [arXiv:hep-ph/0603175](https://arxiv.org/abs/hep-ph/0603175).
- [65] P. Z. Skands, “Tuning Monte Carlo Generators: The Perugia Tunes,” *Phys. Rev. D* **82** (2010) 074018, [arXiv:1005.3457](https://arxiv.org/abs/1005.3457) [hep-ph].
- [66] T. Gleisberg, S. Höche, F. Krauss, M. Schönherr, S. Schumann, *et al.*, “Event generation with SHERPA 1.1,” *JHEP* **02** (2009) 007, [arXiv:0811.4622](https://arxiv.org/abs/0811.4622) [hep-ph].
- [67] S. Höche, F. Krauss, M. Schönherr, and F. Siegert, “QCD matrix elements + parton showers: The NLO case,” *JHEP* **04** (2013) 027, [arXiv:1207.5030](https://arxiv.org/abs/1207.5030) [hep-ph].
- [68] J. Alwall, R. Frederix, S. Frixione, V. Hirschi, F. Maltoni, O. Mattelaer, H. S. Shao, T. Stelzer, P. Torrielli, and M. Zaro, “The automated computation of tree-level and next-to-leading order differential cross sections, and their matching to parton shower simulations,” *JHEP* **07** (2014) 079, [arXiv:1405.0301](https://arxiv.org/abs/1405.0301) [hep-ph].
- [69] L. Lönnblad and S. Prestel, “Matching Tree-Level Matrix Elements with Interleaved Showers,” *JHEP* **03** (2012) 019, [arXiv:1109.4829](https://arxiv.org/abs/1109.4829) [hep-ph].
- [70] T. Sjöstrand, S. Mrenna, and P. Z. Skands, “A Brief Introduction to PYTHIA 8.1,” *Comput. Phys. Commun.* **178** (2008) 852, [arXiv:0710.3820](https://arxiv.org/abs/0710.3820) [hep-ph].
- [71] **ATLAS** Collaboration, “ATLAS Pythia 8 tunes to 7 TeV data.” ATL-PHYS-PUB-2014-021, 2014. <https://cdsweb.cern.ch/record/1966419>.
- [72] R. D. Ball *et al.*, “Parton distributions with LHC data,” *Nucl. Phys.* **B867** (2013) 244–289, [arXiv:1207.1303](https://arxiv.org/abs/1207.1303) [hep-ph].
- [73] “Summary of ATLAS Pythia 8 tunes,” Tech. Rep. ATL-PHYS-PUB-2012-003, CERN, Geneva, Aug, 2012. <https://cds.cern.ch/record/1474107>.

- [74] **GEANT4** Collaboration, S. Agostinelli *et al.*, “GEANT4: A simulation toolkit,” *Nucl. Instrum. Meth. A* **506** (2003) 250.
- [75] **ATLAS** Collaboration, “The ATLAS Simulation Infrastructure,” *Eur. Phys. J. C* **70** (2010) 823, [arXiv:1005.4568 \[hep-ex\]](#).
- [76] M. Czakon and A. Mitov, “Top++: A Program for the Calculation of the Top-Pair Cross-Section at Hadron Colliders,” *Comput. Phys. Commun.* **185** (2014) 2930, [arXiv:1112.5675 \[hep-ph\]](#).
- [77] P. Kant, O. M. Kind, T. Kintscher, T. Lohse, T. Martini, S. Mölbitz, P. Rieck, and P. Uwer, “HatHor for single top-quark production: Updated predictions and uncertainty estimates for single top-quark production in hadronic collisions,” *Comput. Phys. Commun.* **191** (2015) 74–89, [arXiv:1406.4403 \[hep-ph\]](#).
- [78] N. Kidonakis, “Two-loop soft anomalous dimensions for single top quark associated production with a W- or H-,” *Phys. Rev. D* **82** (2010) 054018, [arXiv:1005.4451 \[hep-ph\]](#).
- [79] R. Gavin, Y. Li, F. Petriello, and S. Quackenbush, “FEWZ 2.0: A code for hadronic Z production at next-to-next-to-leading order,” *Comput. Phys. Commun.* **182** (2011) 2388–2403, [arXiv:1011.3540 \[hep-ph\]](#).
- [80] A. Lazopoulos, T. McElmurry, K. Melnikov, and F. Petriello, “Next-to-leading order QCD corrections to  $t\bar{t}Z$  production at the LHC,” *Phys. Lett. B* **666** (2008) 62–65, [arXiv:0804.2220 \[hep-ph\]](#).
- [81] J. M. Campbell and R. K. Ellis, “ $t\bar{t}W^{+-}$  production and decay at NLO,” *JHEP* **07** (2012) 052, [arXiv:1204.5678 \[hep-ph\]](#).
- [82] R. Frühwirth, “Application of kalman filtering to track and vertex fitting,” *Nuclear Instruments and Methods in Physics Research Section A: Accelerators, Spectrometers, Detectors and Associated Equipment* **262** no. 2, (1987) 444 – 450.
- [83] **ATLAS** Collaboration, “The Optimization of ATLAS Track Reconstruction in Dense Environments.” ATL-PHYS-PUB-2015-006, 2015. <https://cds.cern.ch/record/2002609>.
- [84] **ATLAS** Collaboration, “Early Inner Detector Tracking Performance in the 2015 Data at  $\sqrt{s} = 13$  TeV.” ATL-PHYS-PUB-2015-051, 2015. <https://cds.cern.ch/record/2110140>.
- [85] **ATLAS** Collaboration, “Performance of the ATLAS Inner Detector Track and Vertex Reconstruction in High Pile-Up LHC Environment.” ATLAS-CONF-2012-042, 2012. <https://cds.cern.ch/record/1435196>.

- [86] **ATLAS** Collaboration, “Topological cell clustering in the ATLAS calorimeters and its performance in LHC Run 1,” *Eur. Phys. J. C* **77** (2017) 490, [arXiv:1603.02934 \[hep-ex\]](#).
- [87] M. Cacciari, G. P. Salam, and G. Soyez, “The anti- $k_t$  jet clustering algorithm,” *JHEP* **04** (2008) 063, [arXiv:0802.1189 \[hep-ph\]](#).
- [88] M. Cacciari, G. P. Salam, and G. Soyez, “FastJet User Manual,” *Eur. Phys. J. C* **72** (2012) 1896, [arXiv:1111.6097 \[hep-ph\]](#).
- [89] **ATLAS** Collaboration, “Jet energy scale measurements and their systematic uncertainties in proton–proton collisions at  $\sqrt{s} = 13$  TeV with the ATLAS detector,” *Phys. Rev. D* **96** (2017) 072002, [arXiv:1703.09665 \[hep-ex\]](#).
- [90] M. Cacciari and G. P. Salam, “Pileup subtraction using jet areas,” *Phys. Lett. B* **659** (2008) 119–126, [arXiv:0707.1378 \[hep-ph\]](#).
- [91] **ATLAS** Collaboration, “Tagging and suppression of pileup jets,” <http://cds.cern.ch/record/1700870>.
- [92] **ATLAS** Collaboration, “Optimisation of the ATLAS  $b$ -tagging performance for the 2016 LHC Run.” ATL-PHYS-PUB-2016-012, 2016. <https://cds.cern.ch/record/2160731>.
- [93] **ATLAS** Collaboration, G. Aad *et al.*, “Electron and photon energy calibration with the ATLAS detector using LHC Run 1 data,” *Eur. Phys. J. C* **74** no. 10, (2014) 3071, [arXiv:1407.5063 \[hep-ex\]](#).
- [94] **ATLAS** Collaboration, “Electron efficiency measurements with the ATLAS detector using the 2015 LHC proton–proton collision data.” ATL-CONF-2016-024, 2016. <https://cds.cern.ch/record/2157687>.
- [95] **ATLAS** Collaboration, “Muon reconstruction performance of the ATLAS detector in proton–proton collision data at  $\sqrt{s} = 13$  TeV,” *Eur. Phys. J. C* **76** (2016) 292, [arXiv:1603.05598 \[hep-ex\]](#).
- [96] **ATLAS** Collaboration, “Expected performance of missing transverse momentum reconstruction for the ATLAS detector at  $\sqrt{s} = 13$  TeV.” ATL-PHYS-PUB-2015-023, 2015. <https://cds.cern.ch/record/2037700>.
- [97] D. Adams, C. Anastopoulos, A. Andreazza, M. Aoki, L. Asquith, M. Begel, F. Bernlochner, U. Blumenschein, A. Bocci, S. Cheatham, W. Davey, P.-A. Delsart, P.-O. DeViveiros, A. Dewhurst, D. Duschinger, F. Filthaut, P. Francavilla, F. Garberon, S. Head, A. Henrichs, A. Hoecker, M. Kagan, B. Kersevan, T. Khoo,

- B. Lenzi, D. Lopez Mateos, B. Malaescu, Z. Marshall, T. Martin, C. Meyer, A. Morley, W. Murray, M. zur Nedden, R. Nicolaidou, S. Pagan Griso, G. Pasztor, P. Petroff, C. Pizio, R. Polifka, X. Poveda, R. Reece, F. Ruehr, F. Salvatore, R. Sandstroem, T. Scanlon, D. Scheirich, S. Schramm, A. Schwartzman, K. Suruliz, M. Sutton, E. Thompson, M. Tripiana, A. Tuna, S. Viel, M. Vinciter, I. Vivarelli, M. Wieters, A. Wildauer, and Z. Zinonos, “Recommendations of the Physics Objects and Analysis Harmonisation Study Groups 2014.” ATL-COM-PHYS-2014-451 - Internal note, May, 2014.  
<https://cds.cern.ch/record/1700874>.
- [98] **ATLAS** Collaboration, “Selection of jets produced in 13 TeV proton–proton collisions with the ATLAS detector.” ATLAS-CONF-2015-029, 2015.  
<https://cds.cern.ch/record/2037702>.
- [99] **UA1** Collaboration, G. Arnison *et al.*, “Further evidence for charged intermediate vector bosons at the SPS collider,” *Physics Letters B* **129** no. 3, (1983) 273 – 282.
- [100] C. Chen, “New approach to identifying boosted hadronically decaying particles using jet substructure in its center-of-mass frame,” *Phys. Rev. D* **85** (2012) 034007, [arXiv:1112.2567](https://arxiv.org/abs/1112.2567) [hep-ph].
- [101] K. Cranmer, “Statistical Challenges for Searches for New Physics at the LHC,” [arXiv:physics/0511028](https://arxiv.org/abs/physics/0511028) [physics.data-an].
- [102] ATLAS, CMS, LHC Higgs Combination Group, “Procedure for the LHC Higgs boson search combination in summer 2011,”  
<http://cds.cern.ch/record/1379837>.
- [103] G. Cowan, K. Cranmer, E. Gross, and O. Vitells, “Asymptotic formulae for likelihood-based tests of new physics,” *Eur. Phys. J. C* **71** (2011) 1554, [arXiv:1007.1727](https://arxiv.org/abs/1007.1727).
- [104] A. L. Read, “Presentation of search results: the CL<sub>s</sub> technique,” *Journal of Physics G: Nuclear and Particle Physics* **28** no. 10, (2002) 2693.
- [105] **ROOT** Collaboration, K. Cranmer, G. Lewis, L. Moneta, A. Shibata, and W. Verkerke, “HistFactory: A tool for creating statistical models for use with RooFit and RooStats,” <https://cds.cern.ch/record/1456844>.
- [106] M. Baak, G. J. Besjes, D. Côté, A. Koutsman, J. Lorenz, and D. Short, “Histfitter software framework for statistical data analysis,” *The European Physical Journal C* **75** no. 4, (Apr, 2015) 153, [arXiv:1410.1280](https://arxiv.org/abs/1410.1280) [hep-ex].

- [107] R. D. Cousins, J. T. Linnemann, and J. Tucker, “Evaluation of three methods for calculating statistical significance when incorporating a systematic uncertainty into a test of the background-only hypothesis for a poisson process,” *Nuclear Instruments and Methods in Physics Research Section A: Accelerators, Spectrometers, Detectors and Associated Equipment* **595** no. 2, (2008) 480 – 501, [arXiv:physics/0702156](#).
- [108] I. Antcheva, M. Ballintijn, B. Bellenot, M. Biskup, R. Brun, N. Buncic, P. Canal, D. Casadei, O. Couet, V. Fine, L. Franco, G. Ganis, A. Gheata, D. G. Maline, M. Goto, J. Iwaszkiewicz, A. Kreshuk, D. M. Segura, R. Maunder, L. Moneta, A. Naumann, E. Offermann, V. Onuchin, S. Panacek, F. Rademakers, P. Russo, and M. Tadel, “ROOT — A C++ framework for petabyte data storage, statistical analysis and visualization,” *Computer Physics Communications* **180** no. 12, (2009) 2499 – 2512, [arXiv:1508.07749 \[physics.data-an\]](#).
- [109] “TMVA User’s Guide.” <https://github.com/root-project/root/blob/master/documentation/tmva/UsersGuide/TMVAUsersGuide.pdf>. Accessed: 22-10-2017.
- [110] **ATLAS** Collaboration, “Search for gluinos in events with an isolated lepton, jets and missing transverse momentum at  $\sqrt{s} = 13$  TeV with the ATLAS detector,” *Eur. Phys. J. C* **76** (2016) 565, [arXiv:1605.04285 \[hep-ex\]](#).
- [111] **ATLAS** Collaboration, “Search for squarks and gluinos in events with isolated leptons, jets and missing transverse momentum at  $\sqrt{s} = 8$  TeV with the ATLAS detector,” *JHEP* **04** (2015) 116, [arXiv:1501.03555 \[hep-ex\]](#).
- [112] **ATLAS** Collaboration, “First look at  $pp$  collisions data at  $\sqrt{s} = 13$  TeV in preparation for a search for squarks and gluinos in final states with jets and missing transverse momentum with the ATLAS detector.” ATL-PHYS-PUB-2015-028, 2015. <https://atlas.web.cern.ch/Atlas/GROUPS/PHYSICS/PUBNOTES/ATL-PHYS-PUB-2015-028>.
- [113] **ATLAS** Collaboration, “Search for squarks and gluinos in events with an isolated lepton, jets and missing transverse momentum at  $\sqrt{s} = 13$  TeV with the ATLAS detector.” ATLAS-CONF-2016-054, 2016. <https://cds.cern.ch/record/2206136>.
- [114] M. Backes, D. Bogavac, H. Cheng, M. Gignac, N. M. Hartmann, J. Lorenz, M. Morii, N. Ruthmann, M. Simon, T. Saito, S. Chen, V. Tudorache, S. Zambito, D. Xu, and X. Zhuang, “Another search for squarks and gluinos in events with an isolated lepton, jets and missing transverse momentum at  $\sqrt{s} = 13$  TeV with the

- ATLAS detector.” ATL-COM-PHYS-2016-1615 - Internal Note.  
<https://cds.cern.ch/record/2231788>.
- [115] **ATLAS** Collaboration, “Search for new phenomena in a lepton plus high jet multiplicity final state with the ATLAS experiment using  $\sqrt{s} = 13$  TeV proton-proton collision data,” *JHEP* **09** (2017) 088, [arXiv:1704.08493](https://arxiv.org/abs/1704.08493) [hep-ex].
- [116] A. Roodman, “Blind analysis in particle physics,” in *Statistical problems in particle physics, astrophysics and cosmology. Proceedings, Conference, PHYSTAT 2003, Stanford, USA, September 8-11, 2003*, vol. C030908, p. TUIT001. 2003.  
[arXiv:physics/0312102](https://arxiv.org/abs/physics/0312102) [physics.data-an].
- [117] M. Czakon, D. Heymes, and A. Mitov, “Dynamical scales for multi-TeV top-pair production at the LHC,” *JHEP* **04** (2017) 071, [arXiv:1606.03350](https://arxiv.org/abs/1606.03350) [hep-ph].
- [118] **ATLAS** Collaboration, “Pursuit of new phenomena in final states with high jet multiplicity, high jet masses and missing transverse momentum with ATLAS at  $\sqrt{s} = 13$  TeV.” ATLAS-CONF-2016-095, 2016.  
<https://cds.cern.ch/record/2212161>.
- [119] **ATLAS** Collaboration, “Search for supersymmetry with two same-sign leptons or three leptons using  $13.2 \text{ fb}^{-1}$  of  $\sqrt{s} = 13$  TeV  $pp$  collision data collected by the ATLAS detector.” ATLAS-CONF-2016-037, 2016.  
<https://cds.cern.ch/record/2205745>.
- [120] **ATLAS** Collaboration, “Performance of  $b$ -jet identification in the ATLAS experiment,” *JINST* **11** (2016) P04008, [arXiv:1512.01094](https://arxiv.org/abs/1512.01094) [hep-ex].
- [121] **ATLAS** Collaboration, “Measurement of the Inelastic Proton-Proton Cross Section at  $\sqrt{s} = 13$  TeV with the ATLAS Detector at the LHC,” *Phys. Rev. Lett.* **117** no. 18, (2016) 182002, [arXiv:1606.02625](https://arxiv.org/abs/1606.02625) [hep-ex].
- [122] **ATLAS** Collaboration, “Luminosity determination in  $pp$  collisions at  $\sqrt{s} = 8$  TeV using the ATLAS detector at the LHC,” *Eur. Phys. J. C* **76** (2016) 653,  
[arXiv:1608.03953](https://arxiv.org/abs/1608.03953) [hep-ex].
- [123] **ATLAS** Collaboration, “Jet energy resolution in proton-proton collisions at  $\sqrt{s} = 7$  TeV recorded in 2010 with the ATLAS detector,” *Eur. Phys. J. C* **73** (2013) 2306, [arXiv:1210.6210](https://arxiv.org/abs/1210.6210) [hep-ex].
- [124] M. Bahr *et al.*, “Herwig++ Physics and Manual,” *Eur. Phys. J. C* **58** (2008) 639,  
[arXiv:0803.0883](https://arxiv.org/abs/0803.0883) [hep-ph].

- [125] S. Frixione, E. Laenen, P. Motylinski, B. R. Webber, and C. D. White, “Single-top hadroproduction in association with a W boson,” *JHEP* **07** (2008) 029, [arXiv:0805.3067 \[hep-ph\]](#).
- [126] **ATLAS** Collaboration, ATLAS Collaboration, “Summary of the searches for squarks and gluinos using  $\sqrt{s} = 8$  TeV pp collisions with the ATLAS experiment at the LHC,” *JHEP* **10** (2015) 054, [arXiv:1507.05525 \[hep-ex\]](#).
- [127] **ATLAS** Collaboration, “Search for new phenomena in final states with large jet multiplicities and missing transverse momentum with ATLAS using  $\sqrt{s} = 13$  TeV proton–proton collisions,” *Phys. Lett. B* **757** (2016) 334, [arXiv:1602.06194 \[hep-ex\]](#).
- [128] **ATLAS** Collaboration, “Search for squarks and gluinos in final states with jets and missing transverse momentum using  $36 \text{ fb}^{-1}$  of  $\sqrt{s} = 13$  TeV *pp* collision data with the ATLAS detector.” ATLAS-CONF-2017-022, 2017. <https://cds.cern.ch/record/2258145>.
- [129] **ATLAS** Collaboration, “Search for supersymmetry in final states with two same-sign or three leptons and jets using  $36 \text{ fb}^{-1}$  of  $\sqrt{s} = 13$  TeV *pp* collision data with the ATLAS detector,” *JHEP* **09** (2017) 084, [arXiv:1706.03731 \[hep-ex\]](#).
- [130] **CMS** Collaboration, “Search for supersymmetry in events with one lepton and multiple jets exploiting the angular correlation between the lepton and the missing transverse momentum in proton–proton collisions at  $\sqrt{s} = 13$  TeV,” [arXiv:1709.09814 \[hep-ex\]](#).
- [131] **CMS** Collaboration, “Search for physics beyond the standard model in events with two leptons of same sign, missing transverse momentum, and jets in proton–proton collisions at  $\sqrt{s} = 13$  TeV,” *Eur. Phys. J. C* **77** no. 9, (2017) 578, [arXiv:1704.07323 \[hep-ex\]](#).
- [132] “Summary plots from the ATLAS Supersymmetry physics group.” <https://atlas.web.cern.ch/Atlas/GROUPS/PHYSICS/CombinedSummaryPlots/SUSY/index.html>. Direct link to this version: [https://atlas.web.cern.ch/Atlas/GROUPS/PHYSICS/CombinedSummaryPlots/SUSY/ATLAS\\_SUSY\\_Strong\\_all/ATLAS\\_SUSY\\_Strong\\_all\\_201712.pdf](https://atlas.web.cern.ch/Atlas/GROUPS/PHYSICS/CombinedSummaryPlots/SUSY/ATLAS_SUSY_Strong_all/ATLAS_SUSY_Strong_all_201712.pdf), [https://atlas.web.cern.ch/Atlas/GROUPS/PHYSICS/CombinedSummaryPlots/SUSY/ATLAS\\_SUSY\\_Strong\\_2step/ATLAS\\_SUSY\\_Strong\\_2step\\_201712.pdf](https://atlas.web.cern.ch/Atlas/GROUPS/PHYSICS/CombinedSummaryPlots/SUSY/ATLAS_SUSY_Strong_2step/ATLAS_SUSY_Strong_2step_201712.pdf), Accessed: 17-12-2017.
- [133] F. Bordry, “LHC Status and Outlook.” [https://indico.cern.ch/event/466934/contributions/2473174/attachments/1451176/2316167/Fk\\_Bordry\\_LHC\\_](https://indico.cern.ch/event/466934/contributions/2473174/attachments/1451176/2316167/Fk_Bordry_LHC_)

[Collider\\_Status\\_and\\_outlook\\_EPS\\_July\\_2017.pdf](#), 2017. EPS Conference on High Energy Physics.

- [134] **ATLAS** Collaboration, “Search for Supersymmetry at the high luminosity LHC with the ATLAS Detector.” ATL-PHYS-PUB-2014-010, 2014.  
<https://cds.cern.ch/record/1735031>.

# Acronyms

**ALICE** A Large Ion Collider Experiment. 29

**ATLAS** A Toroidal LHC ApparatuS. 29

**BDT** Boosted Decision Trees. 42

**CERN** European Organization for Nuclear Research. 29

**CKM** Cabibbo–Kobayashi–Maskawa matrix. 4

**CL** confidence level. 108

**CMB** cosmic microwave background. 11

**CMS** Compact Muon Solenoid. 29

**CR** control region. 55

**CSC** Cathode Strip Chamber. 33

**EM** electro-magnetic. 33

**FSR** final state radiation. 25, 80

**GMSB** gauge mediated SUSY breaking. 17

**GUT** grand unified theory. 11

**HLT** High-Level Trigger. 34

**IBL** Insertable B-Layer. 32

**ID** inner detector. 32, 43

**ISR** initial state radiation. 25, 62, 80

- JER** jet energy resolution. 93
- JES** jet energy scale. 42
- JVT** jet vertex tagger. 42
- KLN** Kinoshita-Lee-Nauenberg. 6
- L1** level one. 34, 47
- LAr** liquid argon. 33
- LEP** Large Electron-Positron Collider. 23
- LH** likelihood. 43
- LHC** Large Hadron Collider. 1, 29
- LHCb** Large Hadron Collider beauty. 29
- LO** leading order. 6, 39
- LSP** lightest supersymmetric particle. 11
- MC** Monte Carlo. 39
- MDT** Monitored Drift Tube. 33
- ML** maximum Likelihood. 52
- MS** muon spectrometer. 43
- MSSM** minimal supersymmetric standard model. 11
- MSUGRA** minimal supergravity. 18
- NLL** next-to-leading-logarithmic. 19
- NLO** next-to-leading order. 6, 39
- PDF** parton distribution function. 25
- pMSSM** phenomenological minimal supersymmetric standard model. vii
- POI** parameter of interest. 52, 108

**QCD** quantum chromodynamics. 3

**QED** quantum electrodynamics. 3

**ROC** Receiver Operation Characteristic. 58

**RPC** Resistive Plate Chamber. 33

**SCT** Semiconductor Tracker. 32

**SM** Standard model (of particle physics). 3

**SR** signal region. 55

**SUSY** supersymmetry. 10

**TGC** Thin Gap Chamber. 33

**TMVA** Toolkit for Multivariate Data Analysis. 58

**TRT** Transition Radiation Tracker. 32

**TST** track soft terms. 44, 94

**VEV** vacuum expectation value. 8

**WIMP** weakly interacting massive particle. 11

# Appendix A

## Optimisation plots

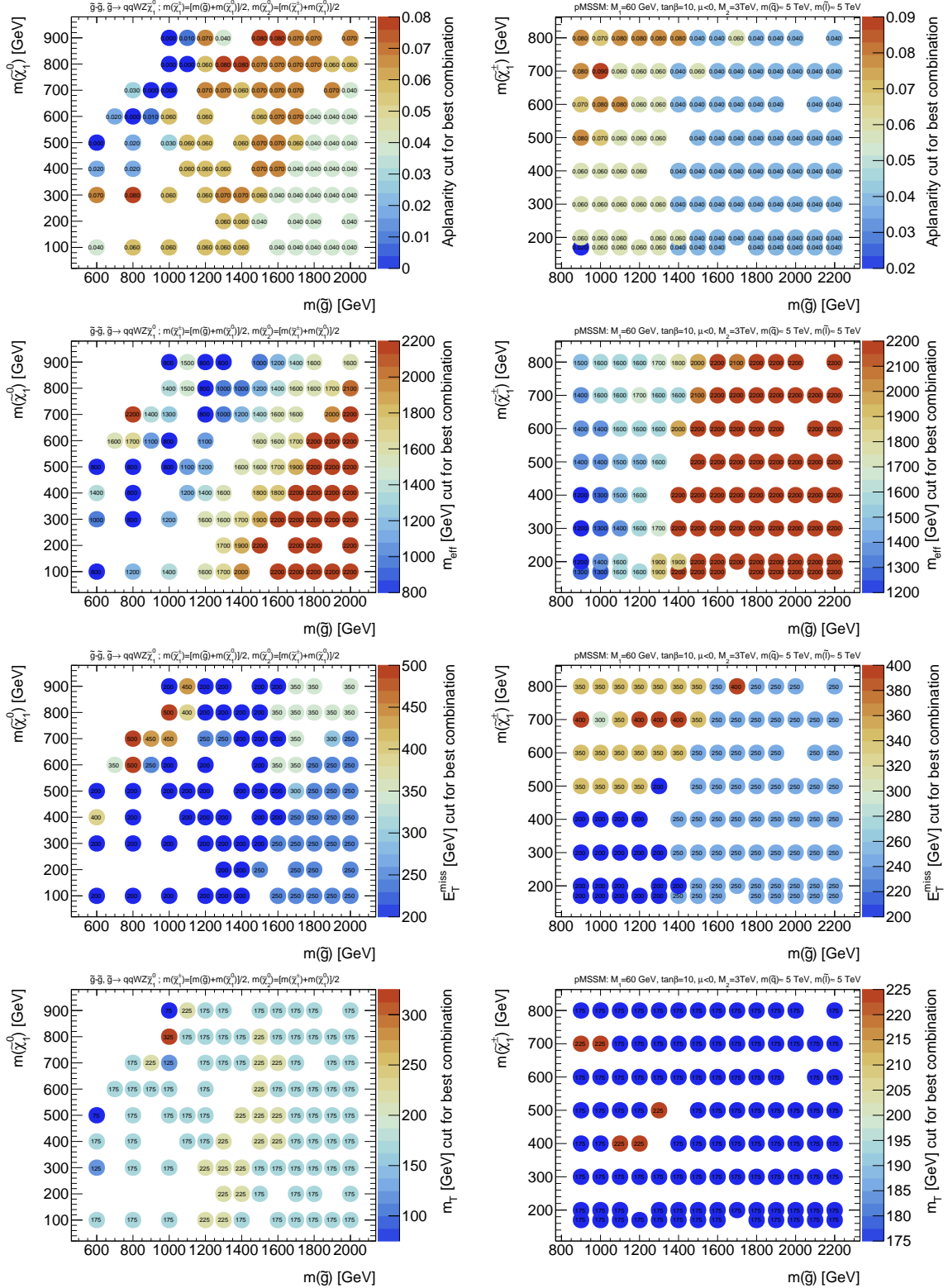


Figure A.1: Cuts for optimal combinations in the N-dimensional optimisation scan for the multijet analysis. The scans for the two-step signals are shown on the left column, the ones for the pMSSM models on the right

# Appendix B

## Signal contamination plots

Figures B.1 - B.6 show potential signal contaminations for all control and validation regions for the **9J** signal region. For reference, exclusion contours from preliminary ATLAS results that were publicly available at the time the regions were designed are shown. The contours in the  $\tilde{g}\tilde{g}$  and  $\tilde{q}\tilde{q}$  one-step grids show the limit set by the 1-lepton analysis [113], the solid line for the  $\tilde{g}\tilde{g}$  two-step grid the limit from the 0-lepton multijet analysis [118] and the dashed line the limit from the same-sign/3-lepton analysis [119]. Outside the excluded contours, no problematic signal contaminations are found.

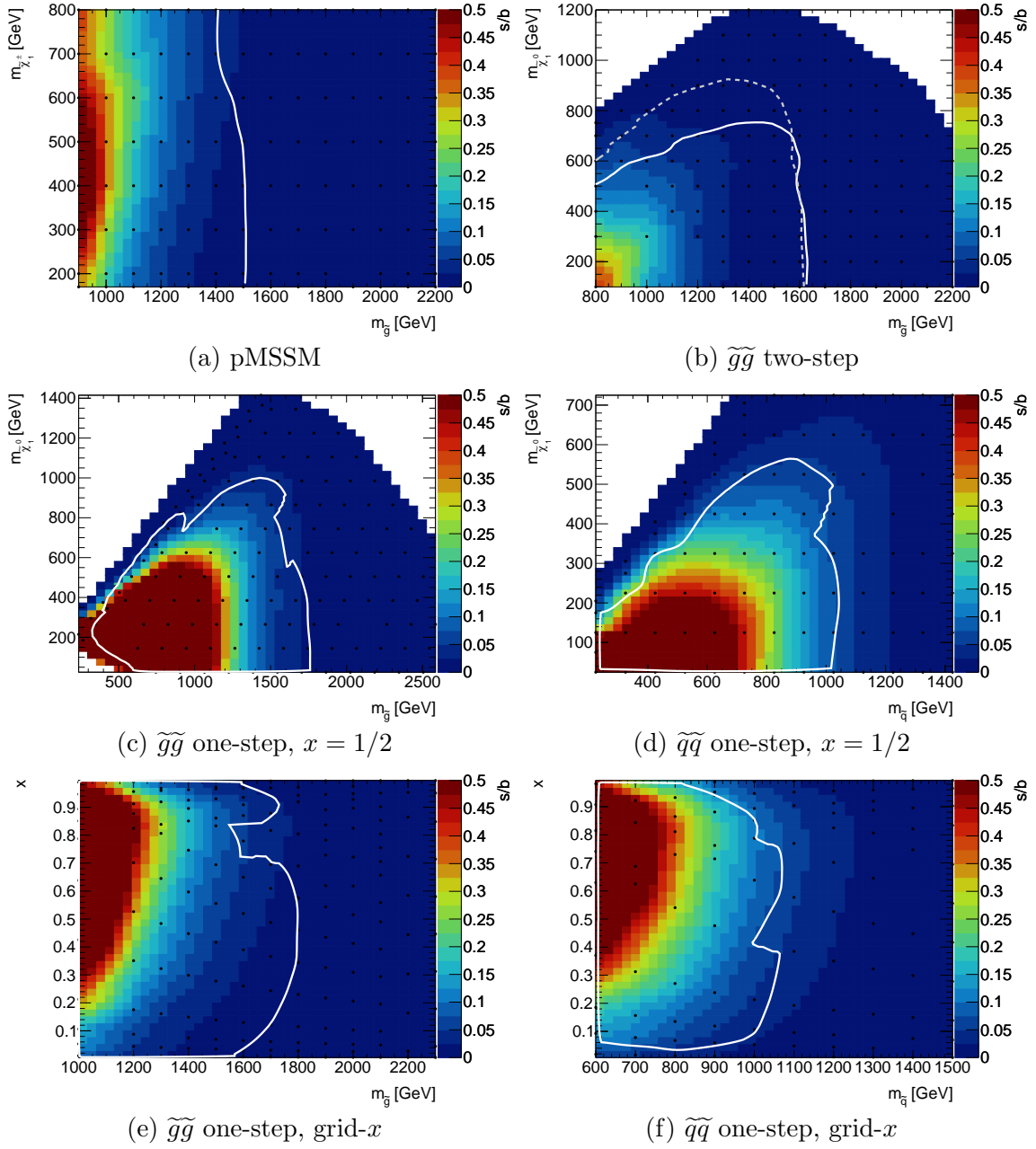
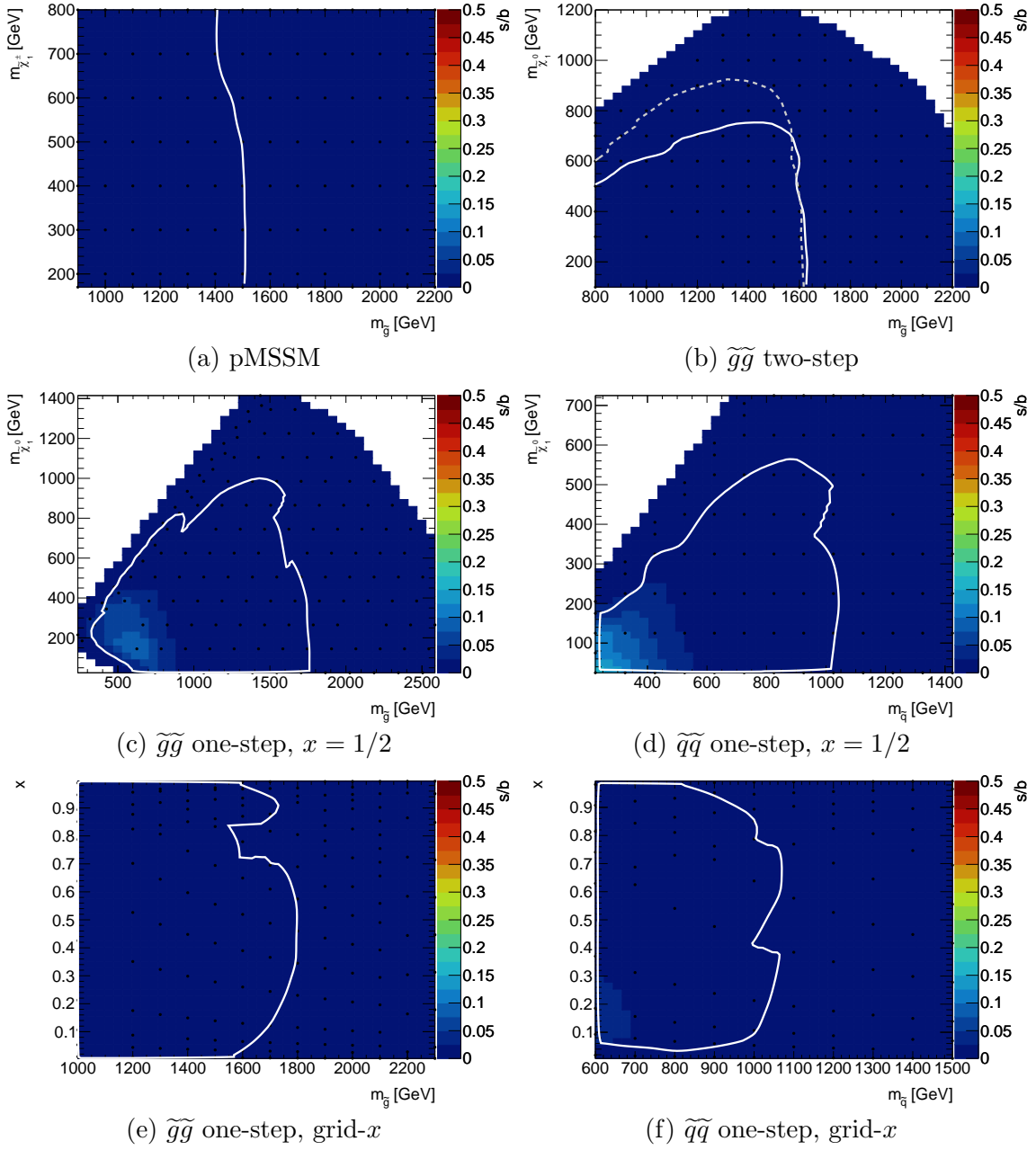


Figure B.1: Signal contaminations for CR A

Figure B.2: Signal contaminations for CR  $B$

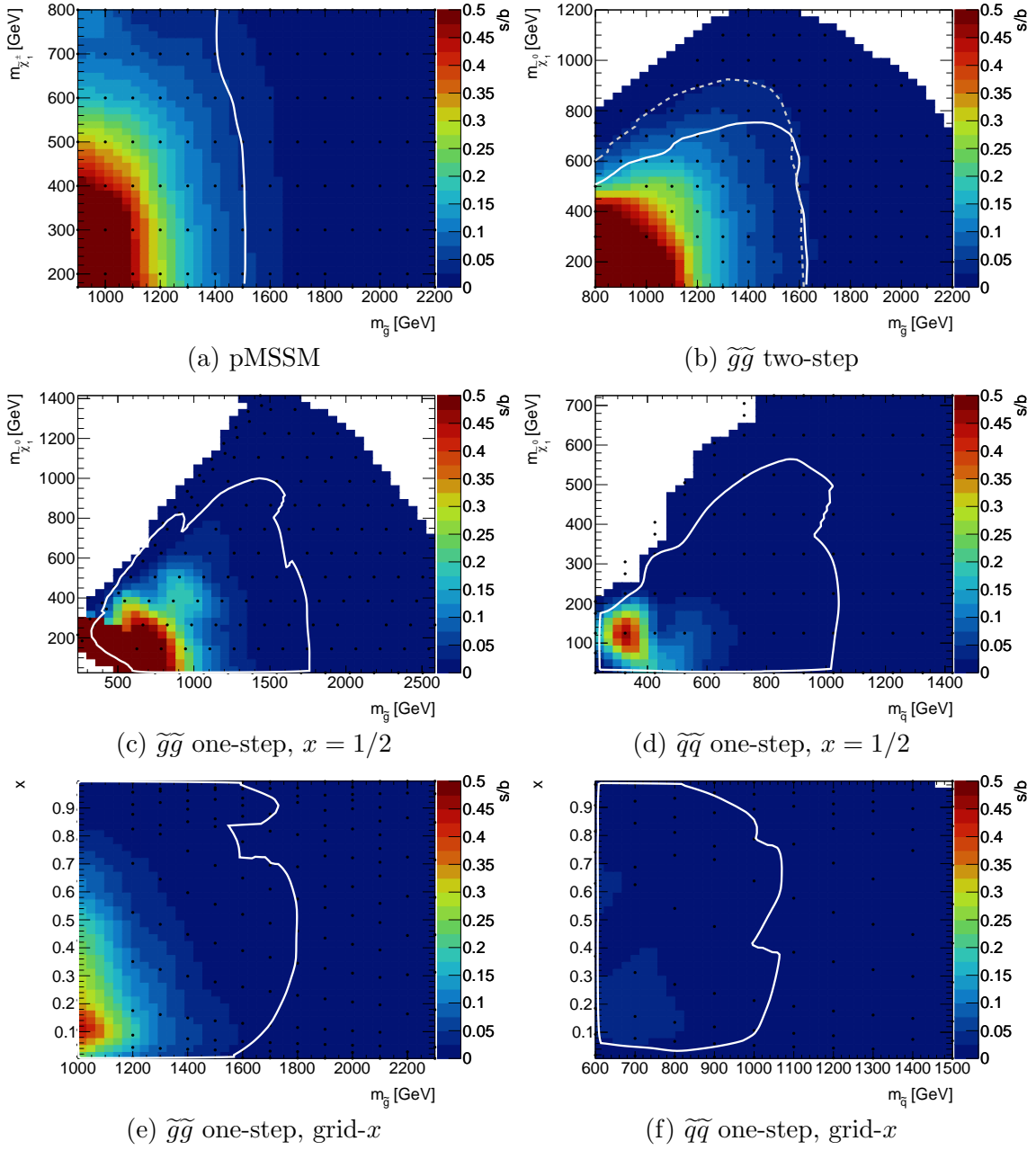


Figure B.3: Signal contaminations for CR C

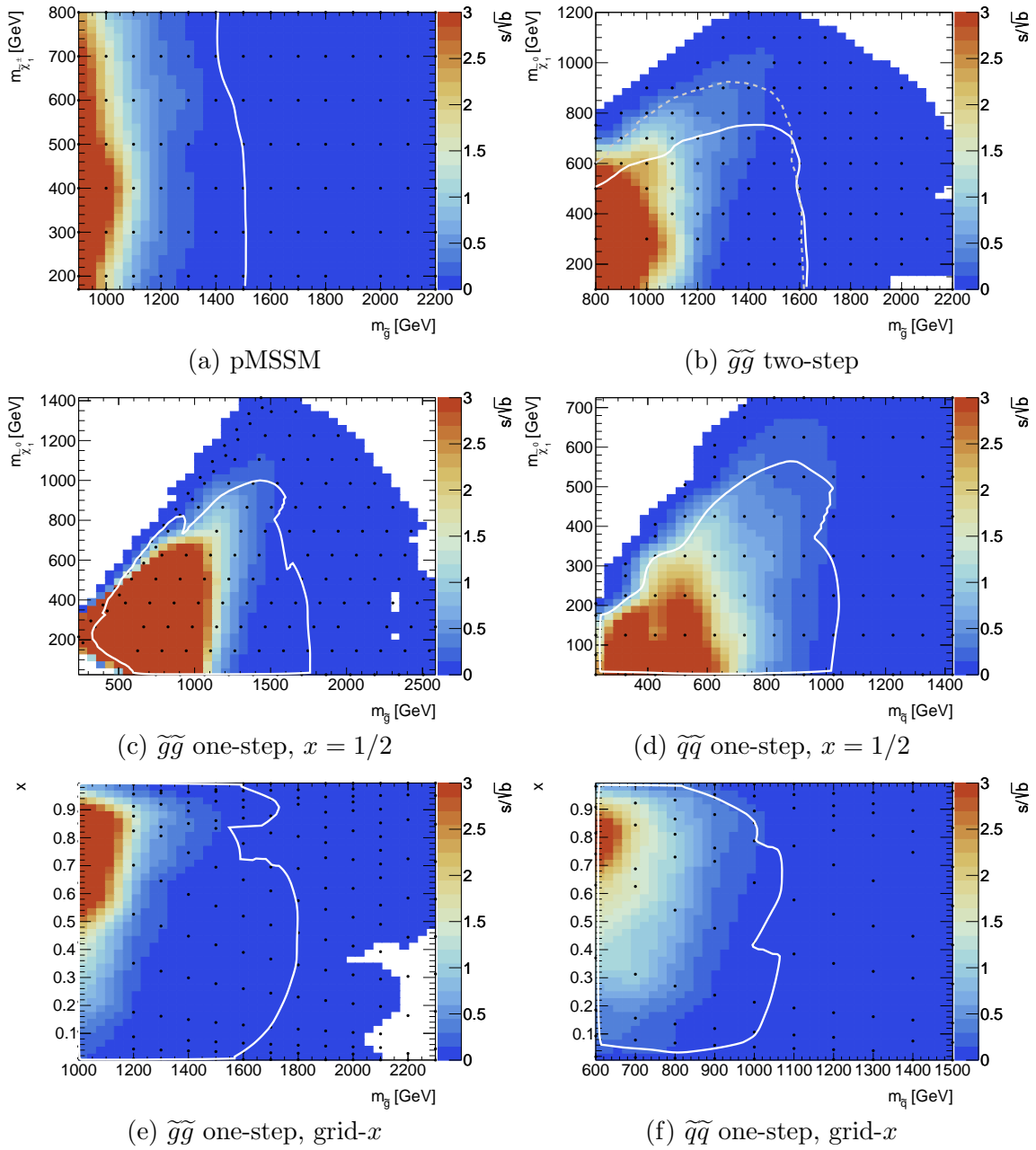


Figure B.4: Signal contaminations in the first  $m_{\text{eff}}$  bin ( $1000 \text{ GeV} < m_{\text{eff}} < 1500 \text{ GeV}$ ) of VR  $m_T$

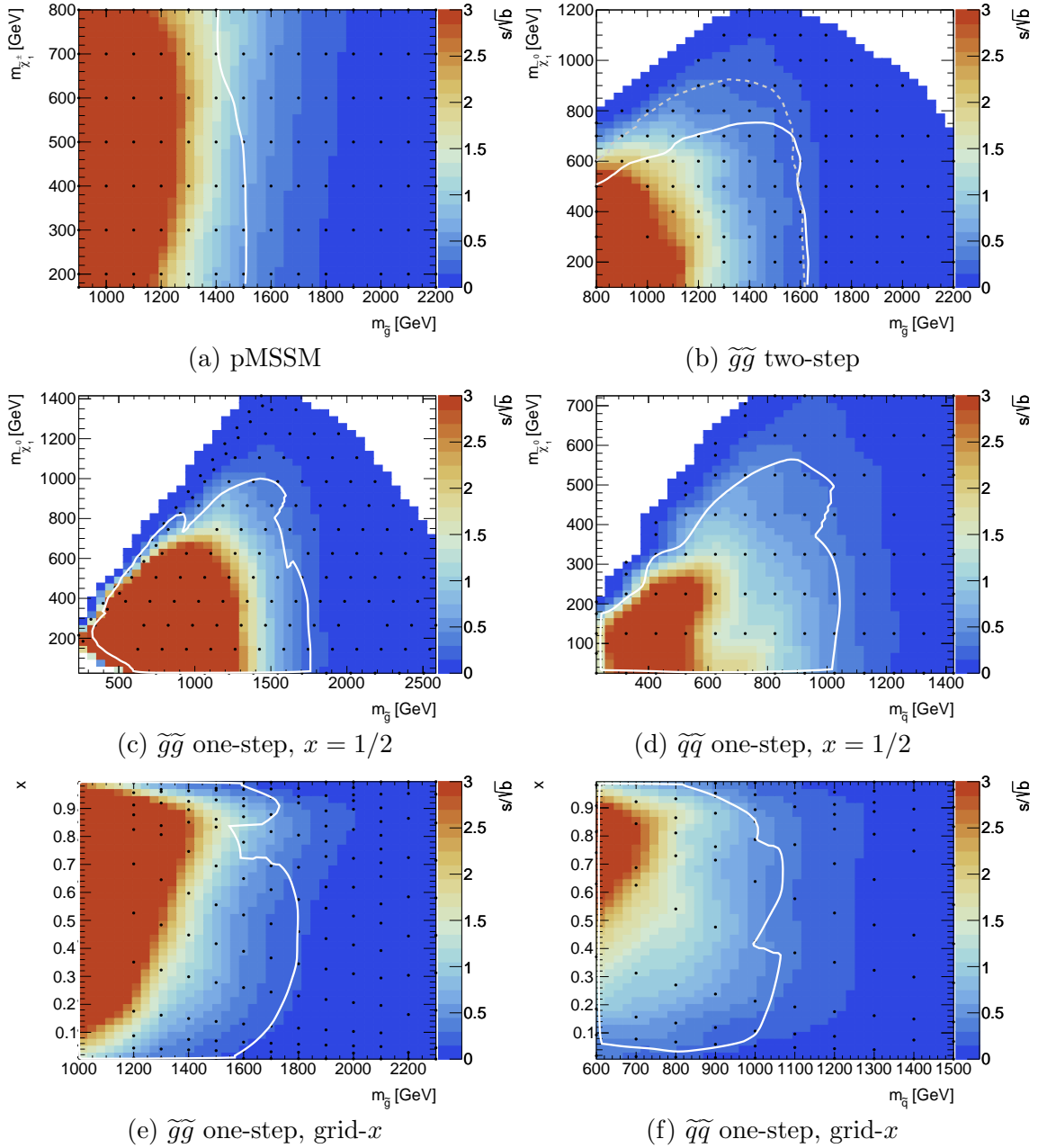
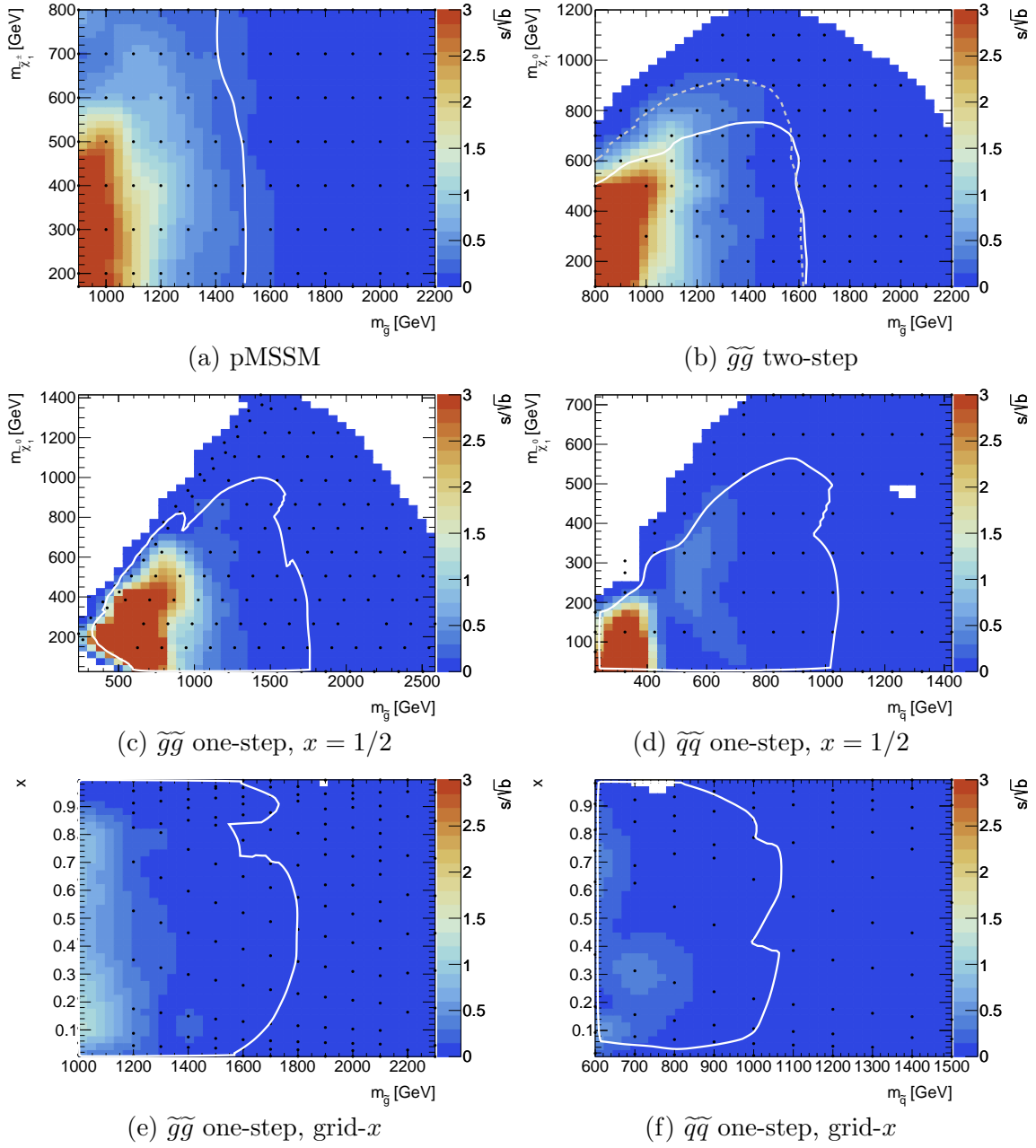


Figure B.5: Signal contaminations in the second  $m_{\text{eff}}$  bin ( $m_{\text{eff}} > 1500$  GeV) of VR  $m_T$

Figure B.6: Signal contaminations in the VR  $N_{\text{jet}}$

# Appendix C

## Studies on the invariant $m_T$ shape

Figures C.1 - C.2 show further studies that were performed to validate the assumptions on the invariance of the  $m_T$  shape for different jet multiplicities.

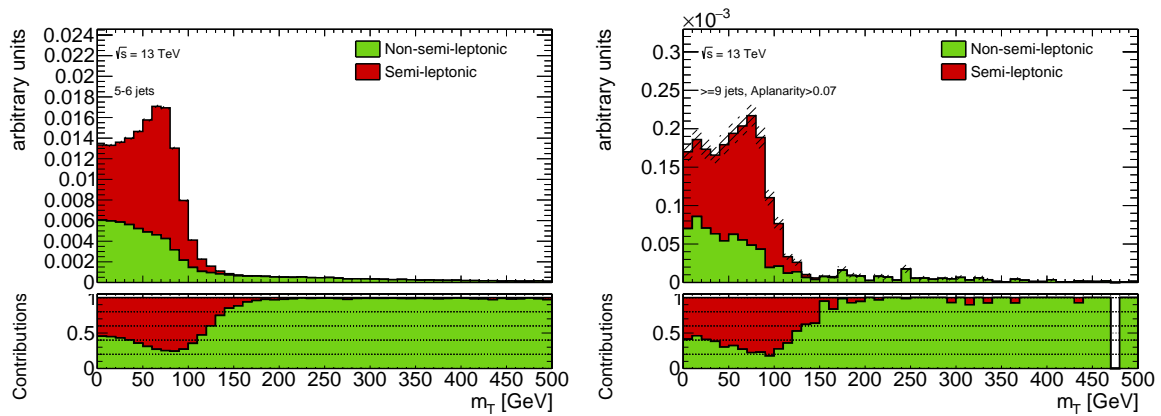


Figure C.1: Contributions of semi-leptonic and non-semi-leptonic decay modes for the  $t\bar{t}$  background for 5-6-jet events (left) and  $\geq 9$  jet events with Aplanarity  $> 0.07$  (right). For both cases the non-semi-leptonic contributions increase in the same way for higher  $m_T$ .

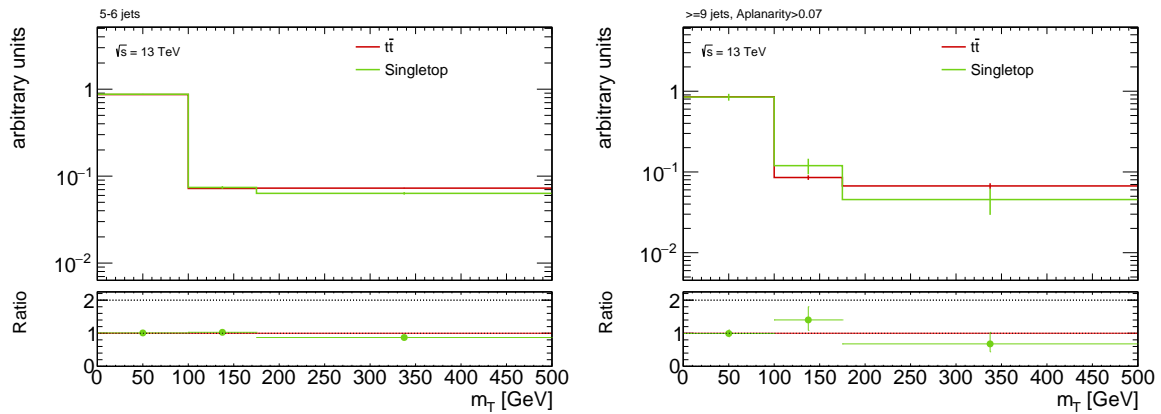


Figure C.2: Transverse mass bins for the single-top and  $t\bar{t}$  backgrounds for for 5-6-jet events (left) and  $\geq 9$  jet events with Aplanarity  $> 0.07$  (right). Both processes show consistent fractions of events in the  $m_T$  tail. This is expected, since the single-top background is dominated by  $Wt$  (in this selection  $\approx 98\%$ ) which has a very similar decay topology. The two backgrounds are normalised by the same parameters in the statistical model.



# Danksagung

Ich bedanke mich bei

- Prof. Dorothee Schaile für die Möglichkeit diese Arbeit an ihrem Lehrstuhl zu schreiben und ihre Unterstützung während der letzten Jahre. Ich schätze sehr, dass sie sich stets für ihre Studenten und Doktoranden Zeit nimmt und mir auch einen 6-monatigen Aufenthalt am CERN und die Teilnahme an Konferenzen und Sommer-schulen ermöglicht hat.
- Prof. Wolfgang Dünneweber für das Erstellen des Zweitgutachtens und allen Mitgliedern der Prüfungskommission für die Bereitschaft an der Prüfung mitzuwirken und die rasche Zusage kurz vor Weihnachten.
- Dr. Jeanette Lorenz für die ausgezeichnete Betreuung und Zusammenarbeit. Sie hat mir ermöglicht schnell in die für mich neue Welt der Suche nach Supersymmetrie bei ATLAS einzusteigen und dadurch die besten Voraussetzungen geschaffen im 1-Lepton Analyseteam mitzuwirken und diese Arbeit zu erstellen.
- Elke Grimm-Zeidler für ihre Hilfe bei sämtlichen Formalitäten und organisatorischen Fragen.
- I would like to thank all members of the 1-lepton analysis team, especially the coordinators Da Xu, Stefano Zambito, Moritz Backes and again Jeanette Lorenz. Thank you for your continuous support all the time, also in times of last minute actions like talk preparations, bug fixes, updated n-tuples with new CP recommendations applied etc. Special thanks also to Matthew Gignac for his analysis code, the 24/7 tech support and all the long and helpful discussions about every detail that needs to be considered when doing data analysis.
- All the people that shared their time with me when i was at CERN.
- The people in the e/gamma and e/gamma trigger group for their support while i was doing my qualification task and service work.

- Nils Ruthmann für seine Ideen und die Unterstützung bei der Entwicklung der 9-Jet Signalregion.
- Allen Mitgliedern des Lehrstuhls für das angenehme Arbeitsklima, die gegenseitige Unterstützung in allen Fragen und nicht zuletzt die großartige Zeit auch außerhalb der Arbeitszeiten.
- Meinem Bürokollegen Thomas Maier für die technische und seelische Unterstützung in allen “phases of grieving” einer Doktorarbeit.
- Balthasar Schachtner für die langen Diskussionen über alle mehr oder weniger wichtigen Details der Physik, des Programmierens und der Datenanalyse mit ATLAS Software, innerhalb und außerhalb der Arbeitszeiten.
- Prof. Otmar Biebel für die Diskussionen in der Küche und seine Fragen nach den Vorträgen im Abteilungsseminar, die mich nicht selten gründlich zum Nachdenken gebracht haben.
- Meiner Familie, die mich bei allem was ich mache unterstützt
- Meiner Freundin Lydia Krug, die immer für mich da ist und mich auch wenn ich deprimiert oder verwirrt bin immer unterstützt.